# INTRACELLULAR TRANSPORT IN CANCER TREATMENTS: CARBON NANOHORNS CONJUGATED TO QUANTUM DOTS AND CHEMOTHERAPEUTIC AGENTS

Kristen Ann Zimmermann

Thesis submitted to the faculty of the Virginia Polytechnic Institute and State University
in partial fulfillment of the requirements for the degree of

Master of Science
In
Biomedical Engineering and Sciences

M. Nichole Rylander, Co-Chair
Christopher G. Rylander, Co-Chair
Timothy E. Long

April 26, 2012
Blacksburg, VA

Keywords: Cancer, carbon nanohorn, quantum dot, transport, cellular uptake kinetics, Intracellular distribution, chemotherapy, hyperthermia

# INTRACELLULAR TRANSPORT IN CANCER TREATMENTS: CARBON NANOHORNS CONJUGATED TO QUANTUM DOTS AND CHEMOTHERAPEUTIC AGENTS

Kristen Ann Zimmermann

## ABSTRACT

Cancer therapies are often limited by bulk and cellular barriers to transport. Nanoparticle or chemotherapeutic compound intracellular transport has implications in understanding therapeutic effect and toxicity. The scope of this thesis was to study the intracellular transport of carbon nanohorns and to improve the efficacy of various chemotherapeutic agents through increased intracellular transport.

In the first study, fluorescent probes (quantum dots) were conjugated to carbon nanohorns to facilitate the optical visualization of the nanohorns. These hybrid particles were characterized with transmission electron microscopy, electron dispersive spectroscopy and UV-VIS/FL spectroscopy. Their cellular uptake kinetics, uptake efficiencies, and intracellular distribution were determined in three malignant cell lines (breast – MDA-MB-231, bladder – AY-27, and brain – U87-MG) using flow cytometry and confocal microscopy. Intracellular distribution did not vary greatly between cell lines; however, the uptake kinetics and efficiencies were highly dependent on cell morphology. In the second study, the efficacy of various chemotherapeutic agents (*i.e.*, doxorubicin, cisplatin, and carboplatin) was evaluated in AY-27 rat bladder transitional cell carcinoma cells. In the future, severe hyperthermia and chemothermotherapy (chemotherapy + hyperthermia) will also be evaluated. Doxorubicin and cisplatin

compounds were more toxic compared to carboplatin. Hyperthermia has previously shown to increase the cellular uptake of chemotherapeutic agents; therefore, chemothermotherapy is expected to have synergistic effects on cell death. This work can then be translated to carbon nanohorn-based laser heating to generate thermal energy in a local region for delivery of high concentrations of chemotherapeutic agents. Although these two concepts are small pieces of the overall scope of nanoparticle-based therapies, they are fundamental to the advancement of such therapies.

# DEDICATION

I would like to dedicate my thesis to my beloved grandmother, Marie A. Sheckells, who sadly, passed away during my graduate career. Grandmom, I want you to know that not a day passes that I do not think about you and miss you. You are an inspiration to me, and remind me how important it is to appreciate everything that God has created.

ACKNOWLEDGEMENTS

First, I would like to thank my advisors, Drs. Nichole and Christopher Rylander for their continued patience and support on this complex and interdisciplinary project. Their constant optimism and drive have been an inspiration. I would also like to show tremendous gratitude to Dr. Timothy Long who has been a wonderful mentor serving on my committee. He has provided enlightening discussions and continued support throughout this project. Next, I thank my lab mates in the Tissue Engineering, Nanotechnology, and Cancer Research (TENCR) laboratory and Biomedical Optical Devices (BODy) laboratory for teaching me various protocols, kindly dealing with my long experiments, and allowing me to hog the chemical fume hood and hot plates. Thank you for your friendships, importantly for making me laugh, and keeping me sane throughout my graduate studies. I would also like to thank Dr. Harry Dorn, Jianfei Zhang, Olga Ivanova, David Inglefield, Erin Murphy, and Renlong Gao for providing insightful chemistry discussions and assisting me with any dangerous experiments. Great thanks to Dr. David Clark, Dr. Robert Hendricks, and Dr. Alex Aning of the Materials Science and Engineering department for their unrelenting support throughout my undergraduate and graduate careers. I also thank the wonderful administrative staff in the School of Biomedical Engineering and Sciences.

I would like to especially acknowledge Dr. David Geohegan at Oak Ridge National Laboratories for kindly providing the carbon nanohorns for this project; Dr. Mitsu Murayama for his assistance with the TITAN TEM and valuable conversation; Melissa Makris for her assistance with flow cytometry; Kathy Lowe and Jay Tuggle for assistance with TEM; Kristi DeCourcy for teaching me to use the confocal microscope; Dr. Peter Vikesland, Dr. Richy Davis, Dr. Yong Woo Lee, Dr. Robert Bodnar, and Dr. Harry Dorn for use of their equipment. Without these kind people, this project would not have been possible.

Finally, I would like to thank my mother and father, Terry and William Zimmermann; my sister and brother, Erin Null and Jason Zimmermann; and the rest of my family whose continued love and support has helped motivate me through graduate school. I also thank Brent Riedel whose support, even from the deserts of Iraq, has helped me get through each day. They believed in me, even when I doubted myself – for that, I only hope that I’ve made you proud. Thank you for being there for me throughout this journey.

TABLE OF CONTENTS

LIST OF FIGURES

LIST OF TABLES

# ATTRIBUTION

Colleagues aided in some of the writing or research included in Chapters 2 and 4 presented in this thesis. A brief description of the co-author contributions is included here.

**Chapter 2:** Single-Walled Carbon Nanohorns Decorated with Semiconductor Quantum Dots to Evaluate Intracellular Transport[*]

[*]This chapter will be submitted to *Nano Research.*

Kristen Zimmermann, M.S., of the Tissue Engineering, Nanotechnology, and Cancer Research/Biomedical Optical Devices laboratories in the School of Biomedical Engineering and Sciences at Virginia Tech wrote this manuscript and conducted all reactions, materials characterization, and cellular internalization research included in the manuscript.

David Inglefield, a graduate student in the Long Research Group in the Department of Chemistry at Virginia Tech edited the manuscript and contributed guidance on materials characterization.

Timothy Long, Ph.D., is currently a professor in the Department of Chemistry at Virginia Tech. Dr. Long was co-PI for one of the grants supporting the research and contributed editorial comments.

Christopher Rylander, Ph.D., is currently a professor in the School of Biomedical Engineering and Sciences/Department of Mechanical Engineering at Virginia Tech. Dr. Rylander was co-PI for one of the grants supporting the research and contributed editorial comments.

Nichole Rylander, Ph.D., is currently a professor in the School of Biomedical Engineering and Sciences/Department of Mechanical Engineering at Virginia Tech. Dr. Rylander was co-PI for one of the grants supporting the research and contributed editorial comments.

**Chapter 4:** Quantum Dot Synthesis in the Presence of SWNHs

Kristen Zimmermann, M.S., of the Tissue Engineering, Nanotechnology, and Cancer Research/Biomedical Optical Devices laboratories in the School of Biomedical Engineering and Sciences at Virginia Tech wrote this manuscript, research was equally contributed (TEM, reaction chemistry, photographs, etc.).

Olga Ivanova, Ph.D., a post-doctorate student in the Institute of Critical Technology and Applied Sciences at Virginia Tech, equally contributed research (TEM, reaction chemistry, photographs, etc.)

# CHAPTER 1. INTRODUCTION AND BACKGROUND

## *1.1. Cancer Disease Statistics*

Cancer remains the second leading cause of death in the United States exceeded only by cardiovascular diseases, with an estimated 1.5 million new cases and 570,000-600,000 deaths in 2009-2010 according to the Centers for Disease Control and Prevention [1, 2]. Malignant cancers are mutated cells that evade the immune system, producing tumor masses that eventually invade and destroy normal tissue. As the incidence of cancer continues to rise with population, advancements in early diagnostic techniques and therapeutic approaches become critical. Three commonly researched cancers are breast, brain, and urinary bladder. Each has a different etiology, incidence, and survival rate; however, they can all ultimately lead to death.

Breast cancer is the leading type of cancer diagnosed in women [3]. While its incidence remains high, its survival rate has grown significantly since the discovery of mammography showing the importance of early diagnostic tools [4, 5]. Since the introduction of mammographic screening and improvements in therapies, the overall 5-year survival rate of breast cancer has risen from 75 to 90% in the last 40 years, with a 99% 5-year survival rate of patients diagnosed with localized breast cancer [6]. Urinary bladder cancer is the fourth most common diagnosed cancer in men, with an overall 5-year survival rate of 78% that drops to just 5% for distant stages [6]. Cancers of the head and neck, while not nearly as common (~10% less cases diagnosed than breast cancer per year), are more detrimental having a mere 35% 5-year survival rate average [6].

Breast cancer is commonly diagnosed during localized or regional stages allowing effective treatment of the disease; whereas brain and urinary bladder cancers are found

during more invasive stages. Brain and urinary bladder cancers typically present "finger-like" processes that invade nearby healthy tissue [7] or multiple tumor masses [8], respectively. This aggressive nature causes the tumor resection to be minimally effective in these types of cancers causing an increase in tumor recurrence and a decrease in survival rate compared to breast cancer. Even though significant advancements in breast cancer diagnostics and treatments were achieved over the past 50 years, annual funding in this area remains the highest due to the high incidence of this disease. For example, the National Cancer Institute of the National Institute of Health allotted over $630 million for breast cancer research, while allotting only $20 million for bladder cancer and $165 million for brain cancer in 2011 [9].

The current treatment standards for malignant tumors involve surgical resection, which is only effective in early stages; chemotherapy, which induces systemic toxicity; and radiation/hyperthermia, which exposes the surrounding normal tissue to harmful doses of radiation [10, 11]. These methods are not selective and induce toxic side effects in the surrounding normal tissues. Additionally, in the case of malignant brain tumors many additional challenges emerge, including evading the blood brain barrier (BBB) and maintaining normal tissue viability [11]. These limitations have motivated researchers to develop novel nano-based structures that rely on passive or active targeting approaches to localize agents in tumor-specific regions and reduce the risk of systemic toxicity [11-13].

### *1.2. Overview of Nanotechnology in Cancer Research*

Significant improvements have been made to understand the etiology of cancers; however, the need for nano-scale manipulation and localized treatments has hindered progress in advanced treatments. Nanotechnology offers a unique approach to enable nano-scale treatments, provide higher resolution diagnostics, and enhance the study of diseases [12]. Nanotechnology is described as man-made materials that have dimensions less than a few hundred nanometers, which have nano-scale specific properties not present in the bulk material [12].

The three main motivations for nanomaterials in medicine are: (1) localized delivery of therapeutic or imaging agents, (2) potential combination therapies, and (3) improved drug kinetics through enhanced circulation times, controlled release, and delivery of hydrophobic agents. Although the full potential of these materials remains unknown, a few nanomaterials have already been approved in medicine as drug delivery vehicles. A common example is Doxil$^{TM}$, which is doxorubicin encapsulated in liposomes for treatment of Kaposi's sarcoma, recurrent breast cancer, and ovarian cancer [10, 14]. Another complex approved for the treatment of metastatic breast cancer is Abraxane$^{TM}$, a paclitaxel-albumin nanoparticle complex [10, 14]. A summary of the current clinical status of nanoparticle systems for cancer therapy are detailed in Table 1.

**Table 1. Summary of current clinical status of nanoparticle systems for cancer therapy. Adapted with permission from Macmillan Publishers Ltd: Nature Reviews Drug Discovery, Davis, M.E. et al. *Nat Rev Drug Disc.* 7, 771-782, © (2008) [14].**

| *Platform* | *Latest stage of development* | *Examples* |
|---|---|---|
| Liposomes | Approved | DaunoXome, Doxil |
| Albumin-based particles | Approved | Abraxane |
| PEGylated proteins | Approved | Oncospar, PEG-Intron, PEGASYS, Neulasta |
| Biodegradable polymer-drug composites | Clinical trials | Doxorubicin Transdrug |
| Polymeric micelles | Clinical trials | Genexol-PM, SP1049C, NK911, NK012, NK105, NC-6004 |
| Polymer-drug conjugate-based particles | Clinical trials | XYOTAX (CT-2103), CT-2106, IT-101, AP5280, AP5346, FCE28068 (PK1), FCE28069 (PK2), PNU166148, PNU166945, MAG-CPT, DE-210, Pegamotecan, NKTR-102, EZN-2208 |
| Dendrimers | Preclinical | Polyamidoamine (PAMAM) |
| Gold nanoparticles | Clinical trials | CYT-6091 |
| Other inorganic or solid particles | Preclinical | Carbon nanotubes, silica particles, quantum dots, etc. |

In addition to delivering chemotherapeutic agents, nanomaterials can also be used for other treatment strategies or to deliver imaging contrast agents to the site of interest to improve diagnosis. Other treatment applications for nanoparticle systems are to enhance photothermal therapy (hyperthermia or ablation) [15-19], radiation therapy [20, 21], and photodynamic therapy [22-25]. Recently, many groups have begun to develop multi-modal or multifunctional nanoparticles, which contain at least two or three of the following qualities: imaging agents (*i.e.,* gadolinium, lutetium, fluorescent probes, etc.), chemotherapeutic agents (*i.e.*, doxorubicin, cisplatin, paclitaxel, etc.), photoabsorptive materials, radiosensitive or radiation-enhancing agents, active targeting ligands, genetic components, etc. [13, 17, 22, 26-28]. An example is illustrated in Figure 1 below.

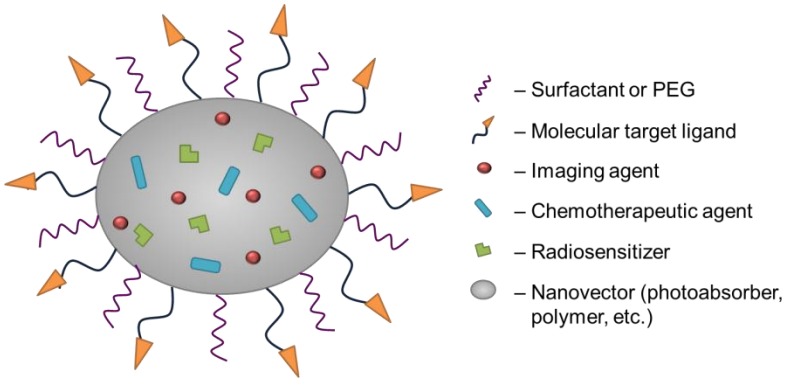


**Figure 1. Illustration of a multi-modal nanovector for simultaneous imaging, drug delivery, enhanced radiosensitivity, etc.**

### *1.3 Nanoparticle Delivery*

Nanoparticle systems offer specific advantages for delivery of therapeutic agents over conventional medicine in cancer treatments by effectively designing the system to preferentially deliver the agents to the tumor site. Many properties can affect nanoparticle transport *in vitro* and *in vivo*, such as the presence of endothelial or tumor cell targeting ligands, nanoparticle size, and shape [29-33]. Aside from nanoparticle geometry and surface characteristics, nanomedicine also takes advantage of the abnormal physiology of neoplastic, or cancerous, tissue by the enhanced permeability and retention effect (EPR) to preferentially accumulate nanoparticles in tumors [31, 34, 35]. There are three methods which nanoparticles can be delivered effectively: (1) systemic delivery and passive targeting; (2) systemic delivery and active targeting; and (3) local injection.

#### *1.3.1. Passive Targeting*

The initial driving force behind nano-scale medicine for cancer therapy was the significant distinction between normal and diseased tissues, which can be defined as the EPR effect. This is known as passive targeting upon systemic injection. Essentially, the

tumor microenvironments have characteristic abnormal vasculature and insufficient lymphatic drainage leading to the accumulation of nanoparticles. Tumors have heterogeneous vascularization, which is disorganized and tortuous leaving avascular regions; the blood flow through the vascular network is independent of vessel size; and the vessel structure is abnormal. Abnormal vessel structures have thick or thin basement membranes, large fenestrations, or wide intercellular junctions [31, 36]. Nanoparticles are thus passively delivered to the tumor through the large fenestrations or wide intercellular junctions, whereas the normal vasculature is void of these properties decreasing nanoparticle extravasation to non-diseased tissue. The purpose of the lymphatic system is to maintain tissue interstitial fluid pressure (IFP); however, in tumors, the highly proliferating cancer cells cause lymphatic vessels to collapse. Tumor lymphatic vessels typically only exist around the tumor margin causing a radial decrease in IFP [31]. Without efficient fluid drainage, the nanoparticles cannot be removed from the tumor [11].

Although the passive delivery of nanoparticles due to the EPR effect has been a fundamental concept for nanomedicine, not all tumors exhibit the same microenvironment. The fenestrae pore cut-off sizes range from approximately 200-2000 nm [37], which is ideal for the delivery of nanomaterials <200 nm, the homogeneity of vascularization [38, 39], and the degree of IFP [40] vary depending on tumor type. Additionally, the high IFP, desmoplasia, and highly dense collagen network characteristic of tumors may inhibit the intratumoral transport leaving nanoparticle accumulation around the periphery of the tumor [31]. Thus, other approaches to improve nanoparticle transport through actively targeting specific cells have become the current standard.

*1.3.2. Active Targeting*

Neoplastic cells that make up tumors have been shown to upregulate specific receptors compared to normal, healthy cells [41-43]. Nanoparticles can then be conjugated with their corresponding targeting agent to selectively target and bind to the receptors on specific cell types after extravasation from the blood vessel. Upon binding, the cells can internalize nanoparticles via receptor-mediated endocytosis. The basic concept of this field of research is to minimize the healthy tissue exposure to the therapeutic agents and selectively localize radiation or absorption-enhancing particles to the diseased tissue.

Common molecular targeting agents are: antibodies (urokinase plasminogen activator (u-PA), anti-HER-2, anti-CDs, etc.), growth factors (*i.e.*, anti-VEGF, anti-EGF, anti-Tf, etc.), chemokines (*i.e.*, CXCL12), peptides (*i.e.*, arginine-glycine-aspartic acid (RGD), hyaluronan, chondroitin sulphate, etc.), vitamins (*i.e.*, folic acid), carbohydrates (*i.e.*, steroids), etc. [10, 12]. The folate receptor (FR) / folic acid (FA) interaction is one of the most commonly studied for drug targeting, as FRs are upregulated in many different types of cancers [44-46]. This is a pathway that may have the most significant potential for reducing systemic toxicity in the widest range of neoplasms. Targeting approaches through angiogenesis and tumor vasculature by targeting growth factor receptors (VEGFR, EGFR, bFGFR, etc.), $\alpha_v\beta_3$-integrins, and matrix metalloproteinases have also shown promise, in addition to targeting neoplastic cells [13, 32]. Molecular targeting of nanoparticles can greatly improve selectivity over current treatment strategies by delivering greater therapeutic agents per binding site and the ability to simultaneously

deliver multi-modal therapies to tumor sites (*i.e.*, thermochemotherapy or radiochemotherapy); however, not without risk.

Despite the improved selectivity using active targeting methods, these modifications become more difficult to achieve, increase their price, and increase the particle diameter [13]. These consequences must be considered because nanoparticle diameter and geometry can greatly influence nanoparticle intracellular and bulk transport. Another challenge faced is the binding affinity of these molecular targeted particles. There must be a balance of binding affinity, such that it is high enough to improve targeting efficiency, while not high enough to block binding sites at the periphery of the tumor causing a decrease in nanoparticle diffusion throughout the tumor [10]. Furthermore, molecular targeting does not overcome transport challenges associated with tumor microenvironment once nanoparticles reach a solid tumor.

### *1.3.3. Local Injection*

Although systemic injection with passive or active targeting has the potential to detect and kill even metastatic cancers, evading the reticuloendothelial system (RES) and improving nanoparticle delivery throughout solid tumors remain major concerns. Serum protein adsorption, or opsonization, is a problem often encountered during systemic delivery of nanoparticles. This process causes the monocytes or macrophages housed in RES organs, such as the spleen and bone marrow, or the Kupffer cells in the liver to clear the foreign materials from the bloodstream [47]. RES uptake may have implications on long term cytotoxicity [48]. Early research demonstrated by adding surface coatings, such as polyethylene glycol (PEG), can reduce RES accumulation by preventing opsonization

[49, 50]. Additionally, the shape, size, and charge of nanoparticles may play a role in biodistribution following systemic injection preventing RES uptake [30, 49].

When a tumor is located in tissues outside of the RES, it may be beneficial to deliver therapies through intratumoral or local injection. The local injection of nanoparticle systems is advantageous if the neoplasm is localized to a specific region because it can minimize the side effects of many treatments [51]. For cancers residing in organs not easily accessible, such as the bladder, brain, colon, etc., an endoscope is often used. Recent investigation of fiber-optic microneedle devices for intratumoral delivery of nanoparticles or chemotherapeutic agents, while simultaneously delivering light, shows great potential to enhance localized therapies [52]. These biomimetic devices have minimal tissue damage as their design is based on the mosquito fascicle [53].

### *1.4. Nanoparticle Design*

Nanoparticle design plays a critical role in effective nano-based therapies. Size and shape can influence pathways, such as nanoparticle delivery, cellular internalization, and intracellular trafficking, in addition to biodistribution upon intravascular injection. Although there is much current research to elucidate these mechanisms, the results are often ambiguous. For example, some work suggests nanoparticles that are spherical in shape with an average diameter of 50 nm have more significant cellular internalization rates compared to rods due to lower energy requirements [29, 54, 55]. However, other groups show that cells internalize particles more readily with higher aspect ratios [56, 57]. These discrepancies may be due to various other factors, such as nanoparticle charge, material, and cell type used.

Additionally, optimal geometry truly depends on the research goal. Current work investigating size dependent cellular internalization shows that smaller nanoparticles are internalized more readily than larger nanoparticles [58, 59]. Some work even suggests that there is an optimal size of 25-50 nm for enhanced cellular uptake [29, 60]. The sizes greatly affect the uptake mechanism required, and may also affect toxicity [59]. For example, if the particles are larger than the size of an endosome (~500-800 nm) a non-endosomal pathway would be required to internalize the particles [59, 61, 62]. However, if the goal of the work is to effectively deliver nanoparticles intravenously, larger particles (> 1μm) of non-spherical shapes may be most effective to enhance circulation time, improve margination dynamics in the vasculature, and improve exposure to surface receptors [63, 64].

These geometry differences also play a role in biodistribution and clearance upon intravenous injection, where large (few microns) or small (<100nm) particles accumulate in the liver due to high Kupffer cell internalization or particles passing through liver fenestrae (pore size ~100 nm); large (few microns) or rod-like particles accumulate in the lungs; (smaller particles (1-10 nm) are often cleared rapidly through the kidneys; and the accumulation of particles in the tumor is favored by particles on the order of fenestrae diameters (100-500 nm) [30, 31, 47, 58, 65-67]. Therefore, all transport pathways must be examined to determine the "optimal" nanoparticle geometry because the size, shape, surface charge, and material can greatly influence the efficacy of the nano-based therapy, in addition to its toxicity.

### *1.5. Transport in Cancer Therapies*

#### *1.5.1. Nanoparticle Bulk Tissue Transport*

Upon systemic or intratumoral injection, nanoparticles encounter a variety of transport barriers prior to reaching the intended site, which are summarized in Figure 2. Nanoparticles and chemotherapeutic drugs alike must first evade the RES (nanoparticles) and lymphatics (chemo- drugs) to ensure availability for extravasation from tumor vasculature [31, 39]. Once extravasated, either via transcytosis or diffusion/convection through pores, the therapies must move through the tumor interstitial space to reach individual cells. Though this transport pathway sounds simple, many barriers exist due to the unique nature of neoplastic tissue. Some of the barriers to these transport mechanisms are summarized in Figure 3 [13, 31, 39].

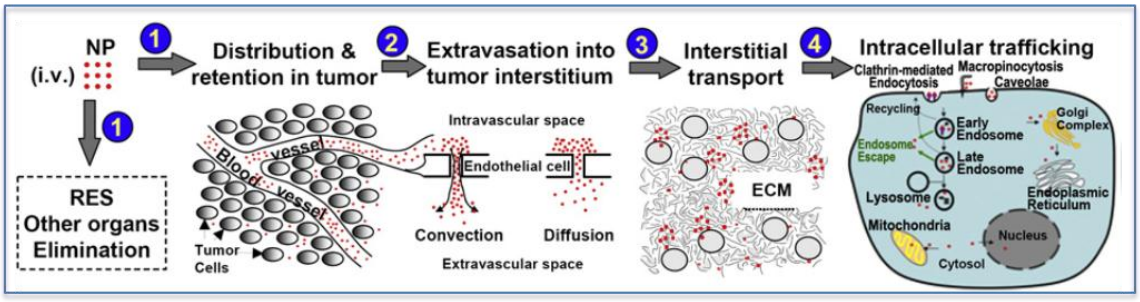


**Figure 2. Illustration of nanoparticle transport pathway to target tissue after systemic injection. Reprinted with permission from Elsevier: Advanced Drug Delivery Reviews, Li, Y. et al., 64, 29-39, © (2012) [39].**

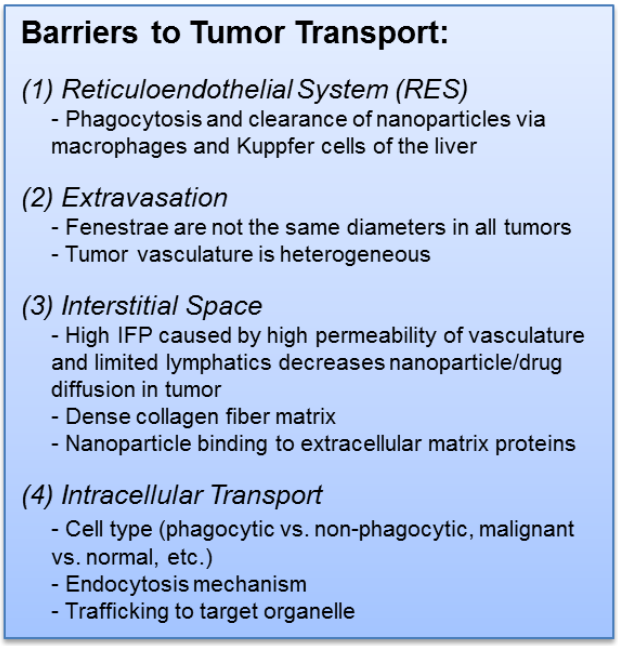


**Figure 3. Summary of nanoparticle/chemotherapy barriers to transport pathways.**

*1.5.2. Nanoparticle Intracellular Transport*

Not only is it important to understand the bulk tissue transport barriers, but intracellular transport as well. Until researchers grasp an understanding of the mechanisms of nanoparticle cellular uptake/exocytosis, cellular uptake rates, intracellular distribution, and sorting pathways, the optimization of nano-based therapies is limited [68]. For instance, selecting nanoparticles that accumulate within the cells' nuclear membranes to deliver nuclear-targeted drugs may potentiate their effects, killing malignant cells more efficiently [69]. In addition, determining the ability of nanomaterials to undergo transcytosis has implications for improved delivery to the intended site and may enable the nano-carriers to cross the blood brain barrier, which is otherwise impervious to diffusion.

Upon the development of novel nanostructures, preliminary nanoparticle-cell interactions are typically evaluated. Commonly, the *in vitro* intracellular transport and

other interactions are only assessed using just one cell line. Other studies, and the study described in Chapter 2 of this document, describe the importance of evaluating nanoparticle-cell interactions in multiple cell lines [70]. Regardless of phagocytic ability, nearly all cells will internalize nano- and even microparticles, but the internalization rates typically differ between cell lines. This emphasizes the significance of thorough nanoparticle-cell interaction evaluation *in vitro,* prior to their implementation *in vivo* to optimize treatment time, concentration, etc. for the tumor type.

### *1.6. Carbon Nanohorns in Cancer Research*

Carbon nanomaterials (CNMs) have greatly impacted the engineering community since their discoveries: the fullerene in 1980 (Sumio Iijima) [71] or 1985 (Smalley *et al.*) [72], the carbon nanotube in 1991 (Iijima *et al.*) [73], and the carbon nanohorn in 1999 (Iijima *et al.*) [74]. The size, shape, and surface functionality can be altered appropriately for specific applications. The most common CNMs are fullerenes, single-walled nanotubes (SWNT), multi-walled nanotubes (MWNT), and single-walled nanohorns (SWNH) [75]. Each of these carbon structures has a similar atomic structure to single graphene sheets; however, the sheets are rolled into tubular or conical shapes due to the number of pentagonal carbon rings present in the graphene sheets [76]. These structures have unique properties, making CNMs suitable for a wide range of applications, including sensors [77, 78], hydrogen storage systems [79-81], solar cells [35, 82], biomolecule sensors [83, 84], drug delivery systems [26, 85-87], photoabsorbing agents [15, 16, 88], etc. – their application is limitless.

In the medical field carbon nanotubes (CNTs) are studied more thoroughly than other forms of carbon. SWNHs (Figure 4), a more recent discovery in CNMs, have many advantages over CNTs as drug delivery systems for cancer therapies. First, they do not require a metal catalyst during synthesis decreasing the risk of heavy-metal induced cytotoxicity [75]. Second, in a preliminary study by our group, SWNHs were more readily endocytosed in the MDA-MB-231 breast cancer cell line than SWNTs (Figure 20). This finding was supported by other studies with gold nanoparticles, where spherical particles were internalized at higher rates than high aspect ratio rods [29].

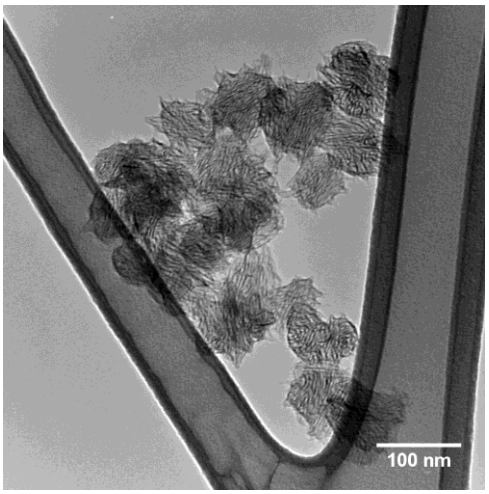


**Figure 4. TEM image of SWNHs placed on a lacey carbon coated copper grid.**

CNMs have recently generated interest for their potential as selective photo-absorbing agents to enhance photothermal therapy (PTT). The use of PTT has been limited due to poor light penetration through the chromophores (*e.g.,* water, hemoglobin, etc.) in healthy tissue causing decreased efficacy. The use of near infrared (NIR) light can be used to overcome some attenuation problems associated with tissue penetration; however, it typically is not enough to eliminate nonspecific injury of surrounding healthy cells upon tumor ablation with PTT [89]. To enhance the selectivity of PTT, the use of

highly absorptive nanomaterials is beneficial. CNMs are highly absorptive in the NIR optical window (700-1100 nm), and their ability to convert photon energy to thermal energy is exceptional [90].

Although gold nanoparticles are currently in clinical trials to enhance PTT [14], carbonaceous nanomaterials (CNMs) may prove more valuable in the future. SWNHs, specifically, have larger internal pore spaces to load large volumes of photodynamic therapy or chemotherapy agents [22], and modifications can be made to the CNM surfaces to attach targeting moieties. Strong carbon-carbon bonds also effectively protect the sensitive adjuvant therapies from degradation prior to reaching the intended location [87]. Additionally, SWNHs may have enhanced photodynamic therapeutic capabilities, similar to fullerenes upon laser-light irradiation [91].

The applications for SWNHs and other CNMs to enhance current cancer therapeutic strategies are infinite. However, there remains a need to evaluate nanoparticle-cell interactions prior to moving forward in the field of nanomedicine. These interactions, along with overcoming the barriers to transport in tumors as observed with chemotherapeutic agents, are *critical* to the development of non-toxic nano-based therapies. Often, CNMs do not possess inherent fluorescence properties to monitor real-time transport and nanoparticle-cell interactions, requiring static methods (*e.g.*, electron microscopy) for evaluation. Therefore, developing stable conjugation strategies to attach fluorescent probes is essential to advance this technology and provide a method to dynamically monitor transport mechanisms.

### *1.7. Hyperthermia*

To overcome these barriers to transport, hyperthermia is often used as an adjuvant therapy with nanomedicine, chemotherapy, or radiation therapy. Hyperthermia is the use of elevated temperatures (between 40 and 44°C) to induce cytotoxic effects in neoplasms, while having minimal effect in normal tissue [92]. This is mainly a result of acidic and hypoxic conditions observed in tumors [93]. An extreme elevation in temperature (> 44°C) can increase cell death at shorter times; however, at these temperatures, it is no longer selective towards neoplastic tissue [92]. Hyperthermia improves bulk transport, such as enhanced permeability of blood vessels, increased blood flow, and increased susceptibility to hyperthermia due to increased oxygen, which augment the delivery of nanomaterials and chemotherapeutic agents [92-96]. Additionally, an increase in sensitivity to chemotherapy is also observed, which may be attributed to increased cellular uptake or enhanced chemotherapy activation via thermal routes [92, 93, 97-100].

The cytotoxic effects observed with *in vivo* whole body hyperthermia-enhanced therapies, such as increased nephrotoxicity [101], could be improved by locally administering hyperthermia. Certain types of nanoparticles are used to enhance laser-based hyperthermia treatments, including gold [17, 24, 102] and carbon nanoparticles [15, 89, 90]. Upon laser irradiation, these nanoparticles can absorb photons emitted from the laser and transfer them to thermal energy. They have potential to localize thermal therapies and permit the use of lower laser powers to obtain the same heat generation in tissue. Recent studies evaluated the use of gold nanorods or graphene oxide-mediated hyperthermia to enhance chemotherapeutic toxicity [103, 104]. SWNHs, therefore, have

the potential to localize temperature elevation for two purposes, to enhance hyperthermia-induced toxicity and to enhance the local pharmacodynamics of chemotherapeutic agents.

# CHAPTER 2. SINGLE-WALLED CARBON NANOHORNS DECORATED WITH SEMICONDUCTOR QUANTUM DOTS TO EVALUATE INTRACELLULAR TRANPSORT

Kristen A. Zimmermann[1], David Inglefield[2], Timothy E. Long[2],
Christopher G. Rylander[1,3], M. Nichole Rylander[1,3]

[1]*School of Biomedical Engineering and Sciences, Virginia Tech, Blacksburg, VA*
[2]*Department of Chemistry, Virginia Tech, Blacksburg, VA*
[3]*Department of Mechanical Engineering, Blacksburg, VA*

*[Contents of this section will be submitted for publication in 2012]*

## *2.1. Motivation*

Single-walled carbon nanohorns show promise as chemotherapeutic drug delivery systems, photo-absorbers for enhanced photothermal therapy, in addition to their use as contrast imaging agent carriers for enhanced tumor detection. Information regarding nanoparticle transport at the cellular and bulk tissue levels is critical to the progression of carbon nanohorn nanotechnologies in medicine, such as intracellular compartmentalization, uptake kinetics, and interstitial transport. Static and destructive approaches are the current standard to evaluate carbon nanomaterial transport. The development of stable conjugation schemes to fluorescently label carbon nanohorns will permit the non-invasive and eventually dynamic study of intracellular carbon nanohorn transport. Although previous work has been conducted to fluorescently label carbon nanotubes to study intracellular transport, limited research with carbon nanohorns has been reported.

The work described in this chapter can be divided into two tasks. The first task of this work proposes a new approach to a commonly used method to enhance stability of

the carbon nanohorn-quantum dot nano-complexes. The second task is to apply these nano-complexes *in vitro* and gain a basic understanding of nanoparticle intracellular transport in three malignant cell lines. Three cell lines were selected to highlight the importance of variability between nanoparticle-cell interactions in various cell types. This study presented in this chapter has been prepared as a manuscript and will be submitted to *Nano Research.*

---

### *2.2. Abstract*

Single-walled carbon nanohorns (SWNHs) have great potential to enhance thermal and chemotherapeutic drug efficiency for cancer therapies. Despite their diverse capabilities, minimal work has been conducted to study nanoparticle intracellular transport, which is an important step in designing efficient therapies. SWNHs, like many other carbon nanomaterials, do not have inherent fluorescence properties making intracellular transport information difficult to obtain. The goals of this project were to: (1) develop a simple reaction scheme to decorate the exohedral surface of SWNHs with fluorescent quantum dots (QDs) and improve conjugate stability and (2) evaluate SWNH-QD conjugate cellular uptake kinetics and localization in various cancer cell lines of differing origins and morphologies.

In this work, SWNHs were conjugated to CdSe/ZnS core/shell quantum dots (QDs) using a unique approach to carbodiimide chemistry. Transmission electron microscopy (TEM) and electron dispersive spectroscopy (EDS) verified the conjugation of SWNHs and QDs. Cellular uptake kinetics and efficiency were characterized in three malignant cell lines, U-87 MG (glioblastoma), MDA-MB-231 (breast cancer), and AY-27 (bladder transitional cell carcinoma) using flow cytometry. Cellular distribution was

verified by confocal microscopy, and cytotoxicity was also evaluated using an alamarBlue assay. Results indicate that cellular uptake kinetics and efficiency are highly dependent on cell type, highlighting the significance of studying nanoparticle transport at the cellular level. Nanoparticle intracellular transport investigations may provide information to optimize parameters (*e.g.*, SWNH concentration, treatment time, etc.) prior to treatment depending on tumor etiology.

KEYWORDS: single-walled carbon nanohorn (SWNH), quantum dot (QD), cellular distribution, uptake kinetics, cancer

### *2.3. Introduction*

Carbonaceous nanomaterials (CNMs) have impacted the engineering community significantly over the past few decades for various applications, such as hydrogen storage [79, 105, 106], sensors (*e.g.*, gas, temperature, biomolecules, etc.) [77, 78, 83, 84], and medical diagnostics and treatments [75, 107, 108], due to their excellent mechanical, chemical, and thermal properties. The versatility of these materials arises from the ability to manipulate and control their sizes, shapes, and surface functionalities. Within the medical field, CNMs have been studied widely to enhance cancer treatment and diagnostic techniques, such as drug delivery systems [26, 85, 86, 109], photoabsorbers in laser-based therapies [15, 16, 88], and MRI contrast agent carriers [110-113]. The strong carbon-carbon bonds present in CNMs create chemically and mechanically inert carriers. Chemotherapeutic and magnetic resonance imaging (MRI) contrast agents are thus protected from degradation as they are transported to the sites of interest [87], in addition

to potentially reducing systemic toxicity of the chemotherapeutic agents. Cancer is the second leading cause of death in the United States, and advancements such as the use of nanomaterials in the diagnosis and treatment of the disease are imperative to reduce this ranking [6].

Single-walled carbon nanohorns (SWNHs) share similar structures to the more conventional carbon nanotubes (CNTs); however, in the case of SWNHs, the single graphene sheets are rolled into conical, rather than tubular shapes. Strong van der Waals forces between the open ends of individual SWNHs cause them to assemble into a larger spherical structure [114]. The spherical structures can take the form of dahlias, buds, and seeds as described by Yudasaka *et al.* [76]. Dahlia SWNHs are the most promising because they can be synthesized with extreme purity in large quantities and were, therefore, selected for this study. SWNHs are appealing for biomedical applications over other forms of CNMs for numerous reasons. The most significant advantage is the elimination of metal catalysts during synthesis, thereby reducing cytotoxic effects [75, 76]. Furthermore, nanoparticle shape and size is proven to greatly affect nanoparticle intravenous transport, intratumoral transport, and intracellular transport. Chithrani and collaborators found that spherical gold nanoparticles of 50 nm diameter were endocytosed more readily than gold nanorods of various aspect ratios [29]. SWNHs are thus predicted to have a shape that requires less energy to be endocytosed than high aspect ratio CNTs. Finally, SWNHs have larger surface areas and internal storage spaces than CNTs for enhanced exohedral surface modification (*e.g.*, receptor targeting moieties, chemotherapeutic drugs, coatings for biocompatibility, etc.) and endohedral drug loading, rendering them more attractive for active drug delivery systems [115].

Nanomaterials will encounter a series of transport barriers prior to reaching the site of interest, whether targeting the bulk tumor tissue or individual cellular compartments [31, 39]. Nanoparticle design (*e.g.*, shape, size, material, and surface characteristics) will influence transport through the pathways previously stated [30, 39]. The study of "nano-biotransport" is fundamental to the success of nanotechnology to ensure the delivery of adequate concentrations of chemotherapy and other adjuvant agents, such as photoabsorptive materials, photodynamic therapy agents, and radiosensitizers. Additionally, information specifically regarding intracellular transport will have implications in directing agents to the appropriate cellular pathways. Potential cytotoxic or long-term effects of endocytosed nanoparticles may also correlate to transport information, such as the intracellular location of the particles or the uptake kinetics [116].

Many nanomaterials, such as iron oxide nanoparticles and CNMs (with the exception of a portion of single-walled carbon nanotubes), lack fluorescent properties sufficient to monitor their optical transport *in vitro* or *in vivo*, limiting the study of their transport [117]. Therefore, more invasive and laborious techniques are necessary, such as paraffin embedding and sectioning of samples to monitor transport at discrete time points with electron microscopy (EM). Additionally, low contrast between CNMs and cell or organelle membranes makes techniques such as EM difficult [118]. Even though gadolinium has been incorporated into SWNHs to enhance contrast in studying SWNH biodistribution using EM [117], few attempts have been made to optically track SWNH transport. This work focuses on developing fluorescently-tagged single-walled carbon

nanohorn conjugates to study intracellular transport *in vitro* using semiconductor quantum dots (QDs).

Traditionally, many organic fluorescent probes, such as fluorescein and cyanines, are used to enhance imaging of nanoparticles in biomedical research [22]; however, the use of QDs has generated significant interest because they have several benefits over conventional probes. The most prominent advantages are that they are resistant to both photo- and chemical degradation over time and they have a wide excitation band with a narrow emission band. Furthermore, they are brighter than other fluorophores and can be tuned to emit specific wavelengths by altering the diameter of the crystal [119, 120]. In particular, near-infrared (NIR) emission wavelengths can be achieved to overcome attenuation problems when used *in vivo*. The current standard nanocrystal composition is cadmium selenide, which generates a concern of toxicity when used in biology due to cadmium ions leaching from the nanocrystal. Many studies aim to determine *in vitro* and *in vivo* toxicity; however, the results are ambiguous and highly dependent on nanocrystal size, surface charge, stability in solution, and physical environment [121-124]. Recent research is directed in the synthesis of cadmium-free nanocrystals, though their commercial availability is limited and the quantum yield has yet to reach that of CdSe nanocrystals (except in the NIR emission region) [125-127]. Despite these concerns, QDs can be easily surface modified with target ligands, polymers, or chemotherapeutic agents.

Previous groups have demonstrated that QDs can be successfully conjugated to CNT surfaces with various non-covalent [128] or covalent methods, including acid-chloride [129], carbodiimide [27, 130, 131], *in situ* QD growth [132, 133], and streptavidin adsorption [134]. Nevertheless, limited work has been conducted to

conjugate QDs to SWNHs [110]. Each of these methods has challenges, such as the use of harsh solvents during synthesis, lack of stability (*i.e.*, precipitation), cost, and the likelihood that QDs will detach from the CNT surface. This work builds upon the carbodiimide approach used by Dorn *et al.* [110] to optimize the method and improve conjugate stability. Previous studies using this technique typically conjugate amine-functionalized QDs, often prepared with monothiols, to carboxyl-functionalized CNTs. However, these methods may not be stable due to the labile interaction between monothiols and QDs [135]. The combination of carbon nanohorns and other inorganic nanoparticles, such as QDs may have substantial impact in fields outside of biological imaging. These heterostructures could create new opportunities as supercapacitors, gas, vapor, or molecular sensors, field emission displays, etc. [136].

In this study, SWNHs were successfully conjugated to semiconductor QDs using a conventional carbodiimide approach. We hypothesized that thiol-functionalized SWNHs will serve as multi-dentate substrates to interact with the QD surfaces and enhance conjugation stability, thereby creating a highly decorated SWNH with surface conjugated QDs. SWNH-QD materials characterization was performed and intracellular transport of SWNHs decorated with QDs was evaluated herein by flow cytometry and confocal microscopy using three cell lines: AY-27, MDA-MB-231, and U-87 MG. These three cell lines were selected to evaluate variations in cellular uptake kinetics (*i.e.*, the rate with which nanoparticles are internalized over time) and uptake efficiency (*i.e.*, the amount of nanoparticles internalized over time) as a result of different cellular morphologies and cancer origination. This study highlights the importance of studying the dynamic transport of nanoparticles in multiple cell lines to better predict nanoparticle-

cell interactions. This is the first in-depth study of SWNH-QD conjugation to conceptualize SWNH transport *in vitro.* The goals of this work were: (1) to develop a simple reaction scheme for exohedral conjugation of fluorescent QDs to SWNHs and (2) to evaluate SWNH-QD conjugate cellular uptake kinetics and efficiency in various cancer cell lines of differing origins and morphologies *in vitro*.

### *2.4. Materials and Methods*

#### *2.4.1. Materials*

SWNHs were synthesized by colleagues at Oak Ridge National Laboratories (Oak Ridge, TN) using a laser vaporization technique based on previously published methods [137]. The SWNHs used in this work were approximately 80-100 nm in diameter, as determined by transmission electron microscopy and ImageJ (data not shown). Cadmium selenide/zinc sulfide core/shell quantum dot powder (emission peak at 630nm) was purchased from Ocean Nanotech, LLC (Springdale, AR). Chloroform and phosphate buffered saline (PBS) mixture were purchased from Fisher Scientific (Pittsburgh, PA). 1-Ethyl-3-(3-dimethylaminopropyl) carbodiimide (EDC), *N*-hydroxysulfosuccinimide (NHS), 2-aminoethanethiol (AET), and fetal bovine serum (FBS) were purchased from Sigma-Aldrich (St. Louis, MO). 1,2-distearoyl-*sn*-glycero-3-phosphoethanolamine-*N*-[methoxy(polyethylene glycol)-2000] (ammonium salt) (DSPE-PEG) (MW = 2805.54) was purchased from Avanti Polar Lipids (Alabaster, AL). Durapore® 0.2 μm nylon membrane filters were purchased from Millipore (Billerica, MA). Dulbecco's Modified Eagle's Medium: Nutrient Mixture F-12 (DMEM/F-12), Roswell Park Memorial Institute (RPMI) 1640 medium, penicillin-streptomycin (pen-strep), and 0.25% trypsin were

purchased from Invitrogen (Carlsbad, CA). Eagle's Minimum Essential Medium (EMEM) was purchased from American Type Culture Collection (ATCC; Manassas, VA). Transmission electron microscopy (TEM) lacey carbon coated copper grids and lacey carbon/carbon film coated copper grids were purchased from Electron Microscopy Sciences (Hatfield, PA) and Pacific Grid Tech (San Francisco, CA), respectively.

*2.4.2. Single-Walled Nanohorn Oxidation*

Water dispersible SWNHs were created by acid functionalization. Similar procedures have been shown to produce oxygen containing functional groups that are negatively charged and are extremely useful for further chemical modification [138, 139]. Briefly, approximately 300 mg of pristine SWNHs were sonicated in 50 mL of 8.0 M nitric acid ($HNO_3$) for 1 h (0.5-0.6 w/v%). The reaction vessel was then placed in an oil bath, heated to 120°C, and stirred for 24 h under reflux. Upon completion, SWNHs were filtered with a 0.1 μm-pore hydrophilic PVDF membrane and rinsed with deionized water ($dH_2O$) until the filtrate reached a pH of 7.0. SWNHs were removed from the membrane and sonicated in 50 mL of 1 M HCl for 1 h. The SWNH-HCl suspension was stirred for 24 h at room temperature to reprotonate the carboxyl groups. The product was filtered again and washed with $dH_2O$ until a pH of 7.0 was reached. Then oxidized SWNHs (SWNHox) were dried in a vacuum oven for 36 – 48 h.

*2.4.3. Carbon Nanohorn – Quantum Dot Conjugation*

SWNHox were dispersed in sterile $dH_2O$ at a final concentration of approximately 0.1 mg/mL by sonication. The dispersion of SWNHox was added to a reaction vessel containing 0.1 M EDC and stirred briefly, followed by the addition of 5 mM NHS. The thiol-containing compound, AET, was then added to the flask at a concentration of 0.2 M and the pH of the solution was adjusted to approximately 6.0 by drop wise addition of 1.0 M HCl to optimize the carbodiimide reaction and prevent disulfide formation. The solution was stirred vigorously overnight at room temperature. AET was selected for this conjugation scheme because of its small size, leading to minimal steric effects. The final product is thiol-functionalized SWNHs (SWNH-SH).

After 24 h, as-purchased QD powder was dissolved in chloroform to a concentration of 1.0 mg/mL and added to the SWNH-SH in a weight ratio of 4:1 QD to SWNH. The ratio of QD to SWNH can be altered to control the degree of QD conjugation to the exohedral surface. The pH of the solution was adjusted to approximately 7.0 by drop wise addition of 1.0 M NaOH to enhance particle stability. As-purchased QD powders contain octadecylamine surface stabilizing ligands, in which the amine has an affinity to the heavy metals, Zn or Cd. Monothiols, such as AET, have higher affinity for heavy metals than the amines, causing ligand exchange on the QD surface at the solvent phase interface. The high affinity of thiol for Cd and Zn causes QDs to move from the organic (chloroform) phase into the aqueous (SWNH-SH in $dH_2O$) phase, creating a SWNH-QD complex dispersed in $dH_2O$. A schematic summarizing the conjugation process is depicted in Figure 5 below.

SWNH-QDs suspended in $dH_2O$ were separated from the chloroform phase with a separatory funnel. The product was then filtered with a 0.2 μm-pore hydrophilic nylon membrane and washed four times with sterile $dH_2O$ to remove any residual reagents and unreacted QDs. After four washes, the 630 nm emission peak of the filtrate was diminished, suggesting all unbound QDs were removed. To sterilize the particles prior to *in vitro* use, SWNH-QDs were filtered with 70% ethanol, followed by four subsequent sterile $dH_2O$ washes. SWNH-QDs trapped on the filter membrane were then sonicated off of the membrane for 1 min in a 0.5 mg/mL DSPE-PEG aqueous solution. This suspension was then stirred for 1 h at room temperature (SWNH-QD+PEG). Polyethylene glycol (PEG) is commonly used to enhance dispersibility and prevent opsonization of serum proteins in biological environments [50]. A concentration of 0.5 mg/mL DSPE-PEG was selected because it showed minimal toxicity in MDA-MB-231 cells using an alamarBlue assay over 24 h, while significantly improving SWNH-QD dispersibility (Supplementary Information (SI), Figure 14). However, higher concentrations of DSPE-PEG (greater than 1.0 mg/mL) did prove to reduce cellular metabolism. Sterile $dH_2O$ was used to make a stock suspension of SWNH-QDs to eliminate the risk of serum protein adhesion during the 1 h of mixing. SWNH-QD+PEG was diluted with the respective cell culture medium to the concentrations of interest. Photographs of each step were taken under ultraviolet excitation to visually demonstrate QD conjugation (Figure 7B and Figure **7**D). From here on, the final product, SWNH-QD+PEG, will be referred to as SWNH-QD.

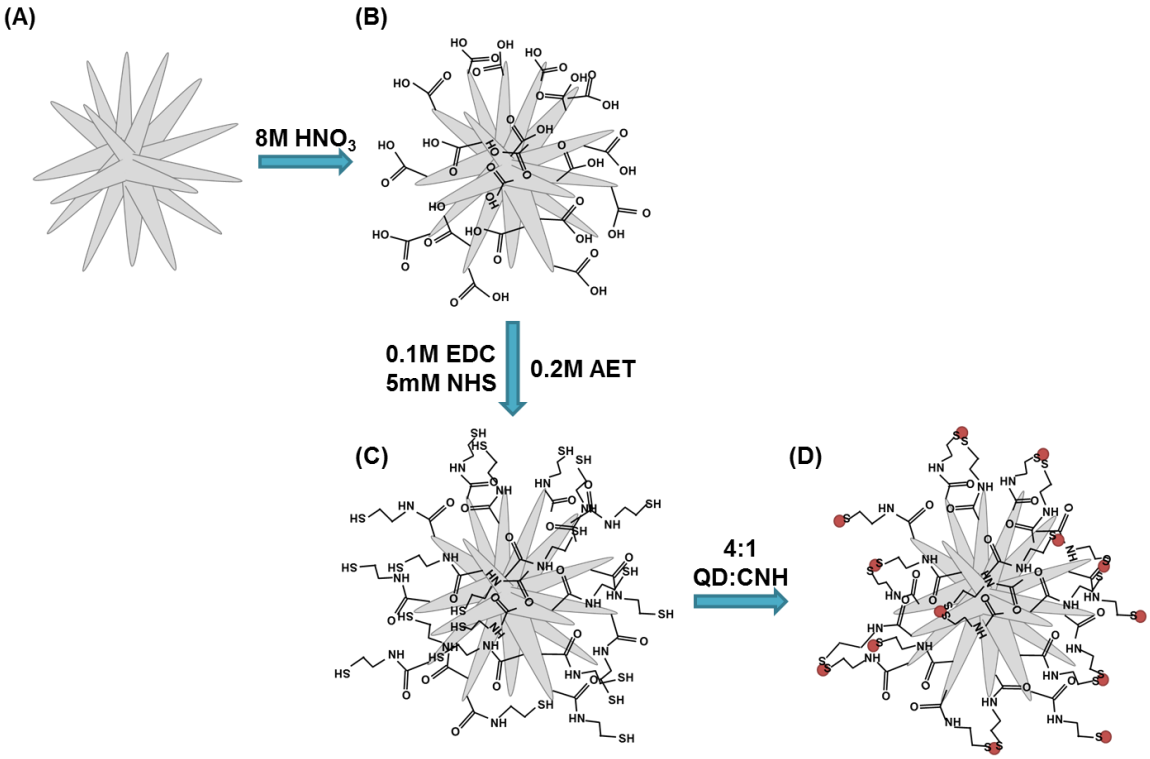


**Figure 5. Schematic of QD conjugation to SWNH exohedral surface. Pure SWNHs (A) were acid oxidized to produce SWNHox (B). SWNHox were functionalized with AET using carbodiimide conjugation (C) and SWNH-QD complexes (D) were synthesized using a ligand exchange approach**

*2.4.4. Materials Characterization*

SWNH-QD conjugation was characterized with transmission electron microscopy (TEM) using either a Zeiss 10CA TEM equipped with AMT Advantage GR/HR-B CCD camera system (Carl Zeiss AG; Oberkochen, Germany) or an FEI$^{TM}$ Titan 300 equipped with high spatial resolution electron dispersive spectroscopy (EDS) (FEI; Hillsboro, OR) for high resolution imaging and elemental quantification. Elemental analysis of SWNH-QD conjugates was performed with EDS to confirm the presence of QD elements (*i.e.*, Cd, Se, and Zn) and linker elements (*i.e.*, N, S). Accelerating voltages of 100kV and 300kV were used to obtain TEM images, respectively with each instrument. The complexes were further characterized by dynamic light scattering (DLS) and

electrophoretic light scattering (ELS) using a Zetasizer NanoZS system (Malvern Instruments; Worcestershire, UK) to obtain their hydrodynamic radius and zeta potential. DLS and ELS were performed at 25°C in water with attenuator position, count rate, and number of runs set to automatic. A 632.8 nm HeNe laser with vertically polarized light was used as the light source. A concentration of 0.05 mg/mL SWNH-QD in water was used for both measurements. DLS and spectrophotometry were performed using 10 x 10 mm quartz cuvettes and ELS was performed using disposable zeta cells (Malvern Instruments; Worcestershire, UK). SWNH-QDs were further characterized with UV-VIS and fluorescence (FL) spectroscopy using a SpectraMAX M2$^{e}$ microplate reader (Molecular Devices; Sunnyvale, CA). Samples were excited with a wavelength of 488 nm to simulate the laser light used for *in vitro* experiments.

*2.4.5. Cell Culture*

The cells in this study include human mammary gland adenocarcinoma epithelial-derived cells, MDA-MB-231 (ATCC); human glioblastoma epithelial-derived cells, U-87 MG (ATCC); and *N*-(*4*-[*5*-nitro-*2*-furyl]-*2*-thiazolyl)formamide induced rat bladder transitional cell carcinoma cells, AY-27, originally developed by Dr. S. Selman and Dr. J. Hampton (Medical College of Ohio, Toledo, Ohio) and kindly donated by Dr. John Robertson (Virginia Tech, Blacksburg, VA). MDA-MB-231, U-87 MG, and AY-27 cells were cultured in complete DMEM/F-12, EMEM, and RPMI 1640 medium, respectively, each supplemented with 10% FBS and 1% pen-strep and maintained in a humidified atmosphere at 37°C, 5% $CO_2$, and 95% air.

*2.4.6. Cytotoxicity Evaluation*

*In vitro* cytotoxicity was evaluated by measuring the metabolic activity using alamarBlue, according to manufacturers' protocol (AbD Serotec; Raleigh, NC). SWNH-QD toxicity at a concentration of 0.025 mg/mL was analyzed after 3 h and 24 h incubation. For this assay, 25,000 cells per well were seeded in TCPS 48-well dishes and incubated for 48 h (~90% confluent), changing the media every 24h. Cells were rinsed with PBS and treated with 500 μL of SWNH-QD ($n$=3) for 3 or 24 h. Cells were then rinsed four times with ice cold PBS to halt endocytosis processes and remove excess SWNH-QDs. Next, 500 μL of 10% alamarBlue in media was added to each sample and incubated for 3 h or 24 h. Then, 100 μL aliquots from each sample were taken in triplicate and placed into a 96-well dish, totaling 9 readings per experimental group. Absorbance was measured with a SpectraMAX M2$^e$ microplate reader (Molecular Devices; Sunnyvale, CA) at 570 and 600 nm according to the manufacturer's protocol. Each experimental group ($n=3$) was tested and analyzed independently. The results were represented as the mean value ± sample standard deviation. Significance of results was verified with Student's t-test and a 95% or 99% confidence was used to determine statistical significance between groups.

*2.4.7. Flow Cytometry Cellular Binding/Uptake*

Fluorescence-activated cell sorting (FACS), a specific type of flow cytometry, was used to estimate cellular uptake rates of SWNH-QDs into three different cancer cell lines. In the context of this study, cellular uptake will refer to both non-specific cellular surface binding and internalization as they cannot be differentiated with the FACS

instrument used. Cells were seeded in tissue culture treated polystyrene (TCPS) 12-well dishes at 100,000 cells per well for each time point and incubated for 48 h prior to treatment (~90% confluent), changing the medium every 24 h. A 0.1 mg/mL stock suspension of SWNH-QDs and 0.5 mg/mL DSPE-PEG in sterile $dH_2O$ was prepared. The SWNH-QD solution was diluted with the respective cell culture medium to a concentration of 0.025 mg/mL and sonicated for 30 sec immediately prior to experiments. This concentration was used to efficiently visualize uptake kinetics over time. Cell culture medium was aspirated and cells were rinsed once with PBS. One milliliter of SWNH-QD was added to each well and incubated for 0, 5, 15, 30, 45, 60, 120, and 180 minutes. After treatment, cells were rinsed four times with ice cold PBS by gentle rocking to halt any endocytosis processes and remove any unbound SWNH-QDs. Cells were then trypsinized with 100 μL of 0.25% Trypsin-EDTA for 3-5 min. Fresh media (1 mL) was added to each well and cell suspensions transferred to centrifuge tubes, followed by centrifugation at 150 G for 5 min at 4°C. Media supernatant was aspirated and 150 μL of fresh media was added to each group creating a final cell density of $1x10^6$ cells/mL. Cell suspensions were placed on ice until analysis. The cell suspensions were analyzed with a BD Biosciences FACSARIA cell sorter (San Jose, CA). A 488 nm excitation source was used with a 610/20 nm emission filter with a 595 nm long pass filter. This experiment was performed on three separate days to obtain an average cellular uptake rate (*n=1*) for each cell line on each day. A small sample size was used to reduce the chance of human error when handling large numbers of samples. Cellular debris was excluded with a forward vs. side scatter gate and aggregates were excluded using height and width parameters on both forward and side scatter.

*2.4.8. Confocal Microscopy*

Immunofluorescent staining with confocal microscopy was performed to study the cellular distribution of SWNH-QDs. Circular glass coverslips (18 mm diameter, No.1) were sterilized in 70% ethanol for 15 min and placed in the bottom of each well of 12-well dishes. Cells were seeded and treated following the same conditions from cellular uptake experiments analyzed with FACS. Cellular distribution at 0 min, 60 min, and 24h was characterized. Following ice cold PBS washes, cells were fixed with a 3.7% paraformaldehyde solution for 15 min. Cells were then rehydrated with PBS; their membranes were permeabilized with a 0.5% Triton-X solution for 15 min; and subsequently blocked with 1% BSA for 30 min. Approximately 30 nM Oregon Green® 488 Phalloidin (Invitrogen; Grand Island, NY) in PBS, an F-actin selective probe conjugated to *2',7'*-difluorofluorescein, was incubated with the cells at room temperature in the dark for 20 min. Cells were then incubated with NucBlue Fixed Cell Stain (Invitrogen; Grand Island, NY), a room temperature-stable DAPI formulation, for 5 min and then rinsed with PBS. Vetashield Mounting Medium (Vector Laboratories; Burlingame, CA) was added to preserve the fluorescence, and coverslips were placed on microscope slides for imaging. A Zeiss LSM510 confocal microscope (Carl Zeiss AG; Oberkochen, Germany) with Enterprise UV 364nm, Argon 488 nm, and HeNe 543nm laser excitation sources was used to image.

## *2.5. Results*

### *2.5.1. Materials Characterization*

CdSe/ZnS core/shell QDs were successfully conjugated to the exohedral surface of SWNHs using a thiol-containing compound as a linker. This synthesis procedure yielded highly decorated SWNHs as evidenced by the TEM micrographs in Figure 6A and Figure 6B. The HRTEM micrograph clearly depicts successful conjugation of the two particles with high contrast QDs attached to the exohedral surface of the low contrast SWNHs. To confirm the elemental composition of the complexes, EDS was performed on an area represented by the red circle in Figure 6B. The high counts of cadmium (Cd) and carbon (C) in Figure 6C are important in verifying the presence of QDs and SWNHs, respectively. The presence of sulfur (S) suggests successful covalent coupling between the particles via the AET linker compound. A copper (Cu) peak was attributed to the Cu TEM grid. A control experiment was performed by mixing pure SWNHs and unfunctionalized QDs. The nanoparticles were mixed in the same ratio (4:1 weight ratio of QDs to SWNHs) in chloroform. TEM micrographs (SI, Figure 15) show minimal adhesion of QDs on the SWNH surfaces in this control experiment, further confirming covalent attachment of QDs using this method.

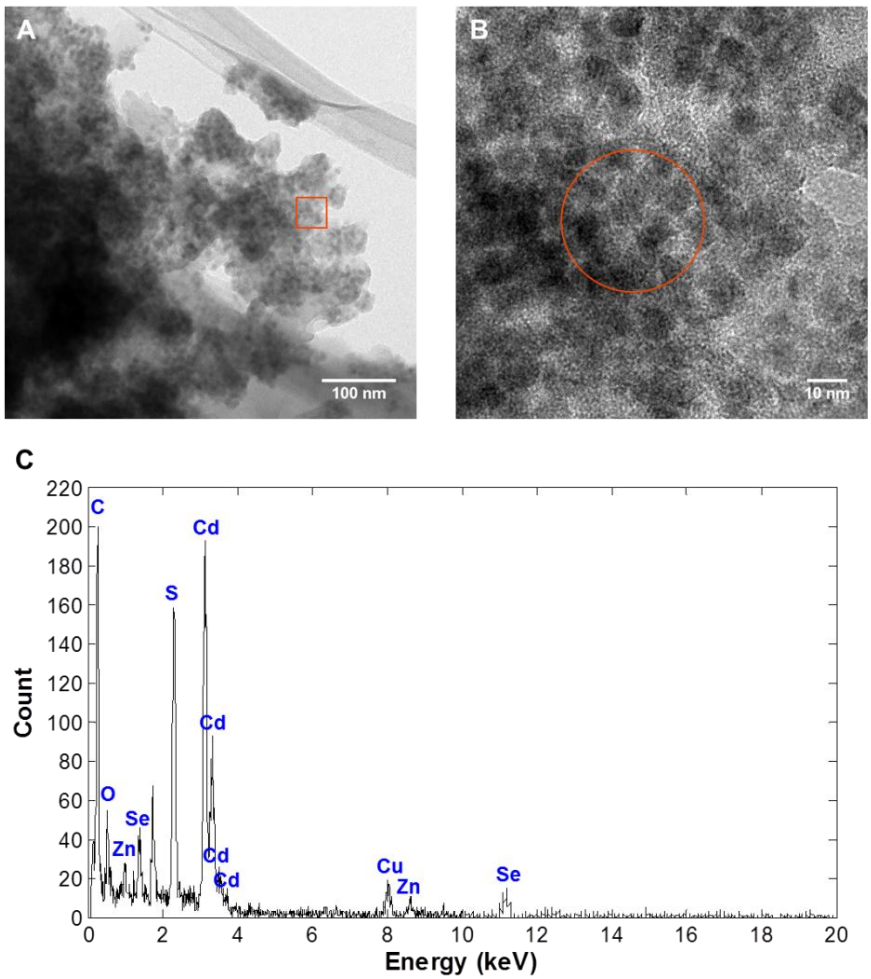


**Figure 6. SWNHs were successfully labeled with a high density of QDs. (A) TEM micrograph of SWNH-QD conjugates shows high contrast spherical CdSe/ZnS QDs are attached to the exohedral surface of the lower contrast SWNHs. (B) Higher resolution image of outlined area (red) depicted in (A). (C) EDS spectra of a zone represented by the red circle in (B).**

SWNHox, SWNH-QD, and as-purchased QDs were further characterized using UV-VIS and fluorescence spectroscopy. The spectra were normalized to the maximum intensity for each spectrum for comparison. The UV-VIS spectrum of SWNH-QD has qualities characteristic to both SWNHox and QD samples as shown in Figure 7A. For example, the conjugate sample is highly absorptive below 500 nm because both SWNHox and QDs also increase absorption at these wavelengths. Additionally, the

conjugate sample has absorbance peaks at approximately 485 and 630 nm, representing the same peaks observed for QDs alone. A slight blue-shift in fluorescence was observed for SWNH-QD conjugates compared to QDs alone (Figure 7C), which could be due to variations in solvent dielectric constants. Furthermore, the conjugates also have a mild fluorescent signal outside of the peak due to SWNH background fluorescence (Figure 7C and Figure 7D), which was also observed by Zhu *et al.* [140].

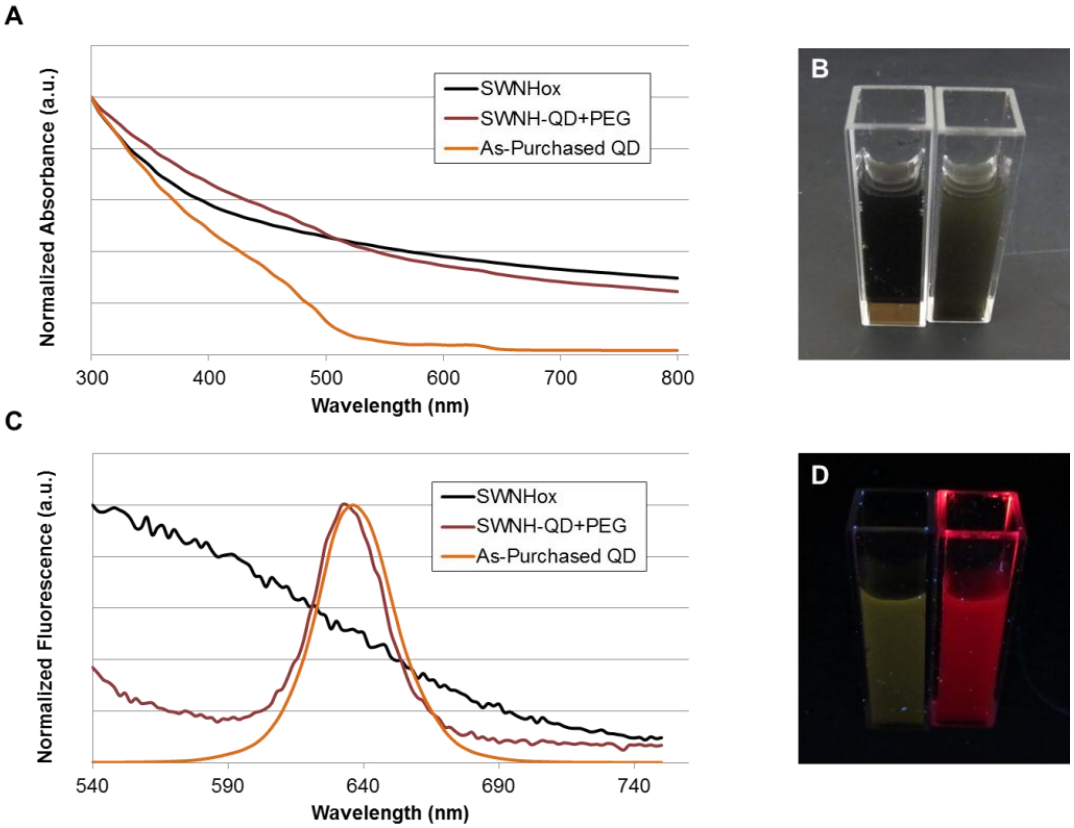


**Figure 7. (A) Normalized UV-VIS absorption spectra of SWNHox, SWNH-QD, and as-purchased QDs. (C) Normalized fluorescence spectra of SWNHox, SWNH-QD, and as-purchased QDs excited at 488nm. (B) and (D) are photographs of SWNHox (vial on left) and SWNH-QD (vial on right) in solution under (B) fluorescent bulb and (D) UV excitation.**

Dynamic light scattering (DLS) and electrophoretic light scattering (ELS) were then performed to further characterize the size (hydrodynamic diameter) and stability

(zeta potential) of SWNHox and SWNH-QDs (Figure 8). DLS analysis of SWNHox and SWNH-QD dispersed in water at a concentration of 0.05 mg/mL indicated that the average hydrodynamic diameters were approximately 150 and 207 nm, respectively. The average diameter of unfunctionalized SWNHs used in this study was 80-100 nm according to TEM analysis. Zeta potential was then analyzed to provide a measure of suspension stability after QD conjugation. The zeta potential, as determined by ELS, decreased from approximately -50 to -30 mV with QD conjugation, suggesting that many of the carboxyl, hydroxyl, or other oxygen-containing groups contributing to the large electric potential of SWNHox are being used to form the amide bond with AET. DLS and ELS results are summarized in Table 2 below.

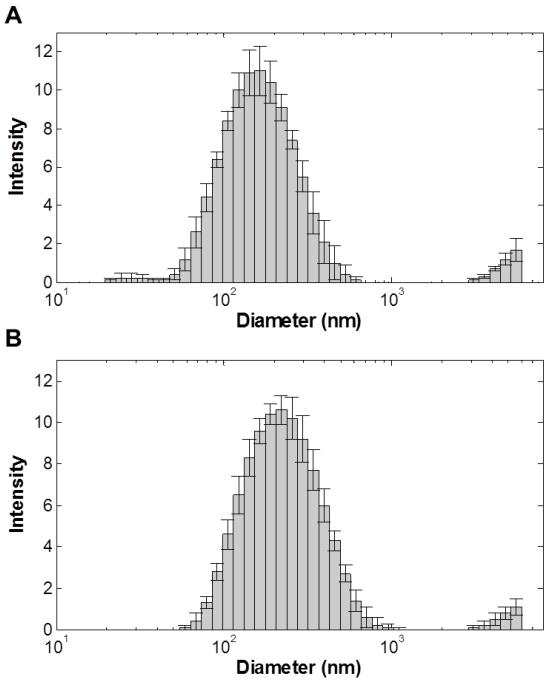


**Figure 8. Dynamic light scattering of (A) SWNHox and (B) SWNH-QD shows an increase in diameter after QD attachment.**

**Table 2. Summary of DLS and ELS results for SWNHox and SWNH-QD**

| *Sample* | *Average Hydrodynamic Diameter ($Z_{avg}$, nm)* | *Zeta Potential (mV)* |
|---|---|---|
| *SWNHox* | 150.2 ± 2.7 | -51.2 ± 1.8 |
| *SWNH-QD* | 207.5 ± 3.6 | -32.3 ± 0.7 |

*2.5.2. Cytotoxicity Analysis*

Prior to in vitro implementation, cytotoxicity was evaluated in three cell lines using a concentration of 0.025 mg/mL. This concentration was also used for cellular uptake kinetics and efficiencies in the following studies. Cytotoxicity analysis after 3 and 24 h incubations using an alamarBlue assay confirmed minimal toxicity in all three cell lines. Evaluation of metabolic activity showed a statistically significant increase in metabolic activity compared to the control in the AY-27 and U-87 MG cell lines after 3 h incubation. After 24 h incubation, only a statistically significant decrease in metabolic activity for the MDA-MB-231 cell line was observed (Figure 9). Current *in vitro* toxicology assays are typically insufficient for determining the toxicity of nanomaterials due to discrepancies between assays; therefore, further investigation is necessary to confirm toxicity.

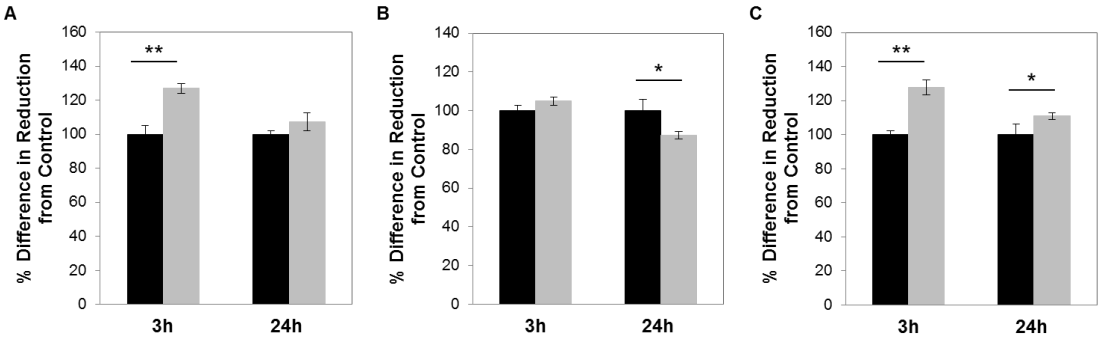


**Figure 9. SWNH-QD have minimal reduction in metabolic toxicity after 3 and 24 h incubation at 37°C evaluated with alamarBlue assay (*n=3*) in (A) AY-27, (B) MDA-MB-231, and (C) U-87 MG cell lines. Black bars represent the untreated control group while grey bars represent cells treated with 0.025 mg/mL SWNH-QD. Data represented as percent difference from the control (no nanoparticle) group determined by Equation S1 in SI. *Denotes statistical difference from the control for $p < 0.05$ and **denotes statistical difference for $p < 0.01$ using Student's t-test.**

*2.5.3. Cellular Binding/Uptake*

Non-specific cellular uptake and binding of SWNH-QD conjugates over the course of 3 h was evaluated with flow cytometry. For the purpose of this work, cellular uptake will be defined as both internalization and non-specific binding to the cell surfaces as it cannot be differentiated with the available flow cytometry system. Cellular uptake rate was quantified by the percentage of cells containing SWNH-QDs and measuring the median fluorescence intensity at each time point (*i.e.*, 0, 5, 15, 30, 45, 60, 120, and 180 min). *In vitro* research investigating the use of nanomaterials as medical tools often fails to evaluate the efficacy over various cell lines. Therefore, in this work, three different malignant cell lines were analyzed to determine if the uptake rates varied with the cell line. Flow cytometry data shows a cell type-dependent cellular uptake of SWNH-QDs, as shown in Figure 10. U-87 MG, human malignant glioblastoma cells, showed the greatest SWNH-QD uptake in the least amount of time compared to MDA-MB-231, human breast

cancer cells, and AY-27, rat transitional cell bladder carcinoma cells. After 60 min, approximately 95%, 80%, and 50% of U-87 MG, MDA-MB-231, and AY-27 cells were sorted as positive for containing SWNH-QDs by FACS, respectively. All cells continued to uptake SWNH-QDs over time in a linear fashion according to the median fluorescence intensity and the side scattering information (SI, Figure 18). Side scattering can be used as a metric of cellular uptake because it is a measure of cellular internal complexity. As the side scattering increases, the internal complexity of the cell also increases, suggesting more nanoparticle internalization. Deviations in FACS data may be due to variations in cell metabolism between passages and variations between SWNH-QD batches from day to day.

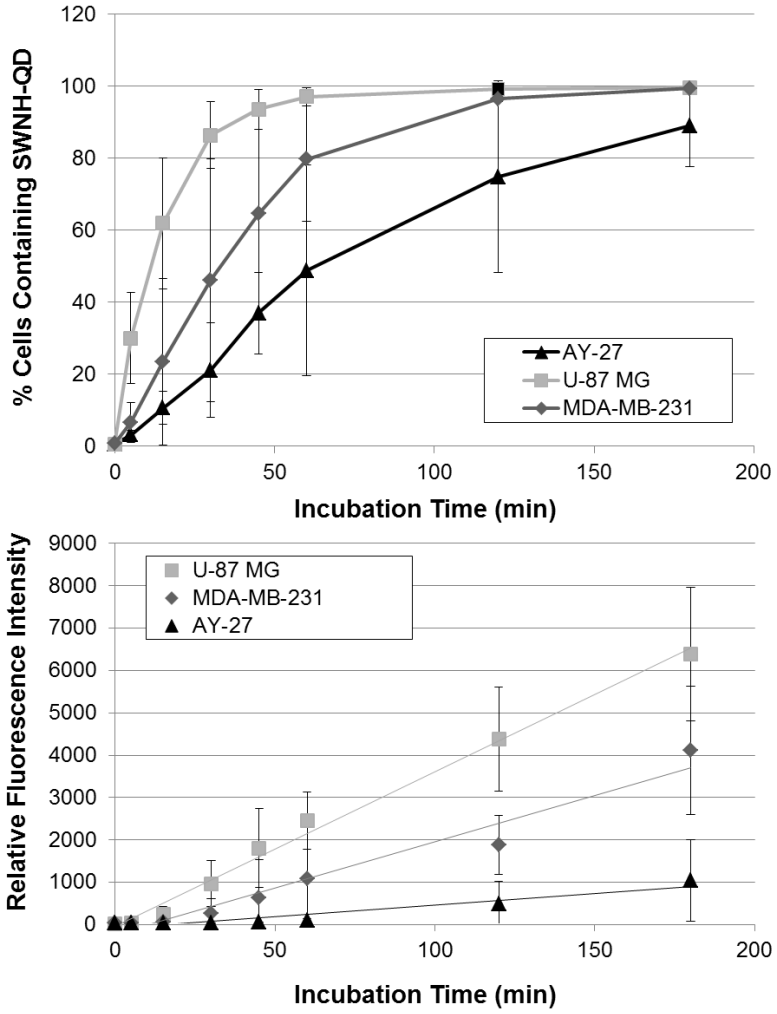


**Figure 10. FACS results of AY-27, MDA-MB-231, and U-87 MG cells incubated with 0.025 mg/mL SWNH-QDs over time represented as (A) the percentage of cells containing SWNH-QDs in the population measured and (B) median fluorescence intensity of the cell population.**

*2.5.4. Intracellular Distribution*

Immunofluorescence staining was performed and imaged with confocal microscopy to analyze SWNH-QD cellular distribution. Cellular nuclei and F-actin were stained to monitor morphology and to determine the localization of SWNH-QDs. F-actin was selected to determine SWNH-QD surface binding compared to internalization because they interact extensively with the cellular membrane and it provided a clearer

visualization of SWNH-QD internalization. Ultimately, SWNH-QDs were found on the cell surface, as well as internalized into the cytoplasm and nuclei of all cell lines within 60 min as shown in Figure 11, Figure 12, and Figure 13 (B and D, all). Over 24 h, cells continued to internalize SWNH-QD conjugates. Additionally, the number of SWNH-QD conjugates found in the nuclei of all three cell lines also increased after 24 h. According to immunofluorescence staining, morphology changed minimally in all three cell lines over a 24 h treatment with SWNH-QDs further confirming minimal toxicity at a concentration of 0.025 mg/mL.

Interestingly, nanoparticles are known to aggregate in cell culture medium over time, reaching sizes of a few microns [141]. Although particles of these sizes are typically not internalized, aggregates were found inside U87-MG and MDA-MB-231 cells after 24 h, but not after 60 min (Figure 12 and Figure 13). Another study by dos Santos *et al*. revealed a similar finding suggesting that nano- and even micron particles are internalized by non-phagocytic cell types suggesting abnormal endocytosis processes occur in the presence of nanomaterials [70]. This abnormal endocytosis process may be attributed to alterations in cytoskeletal stiffness following internalization.

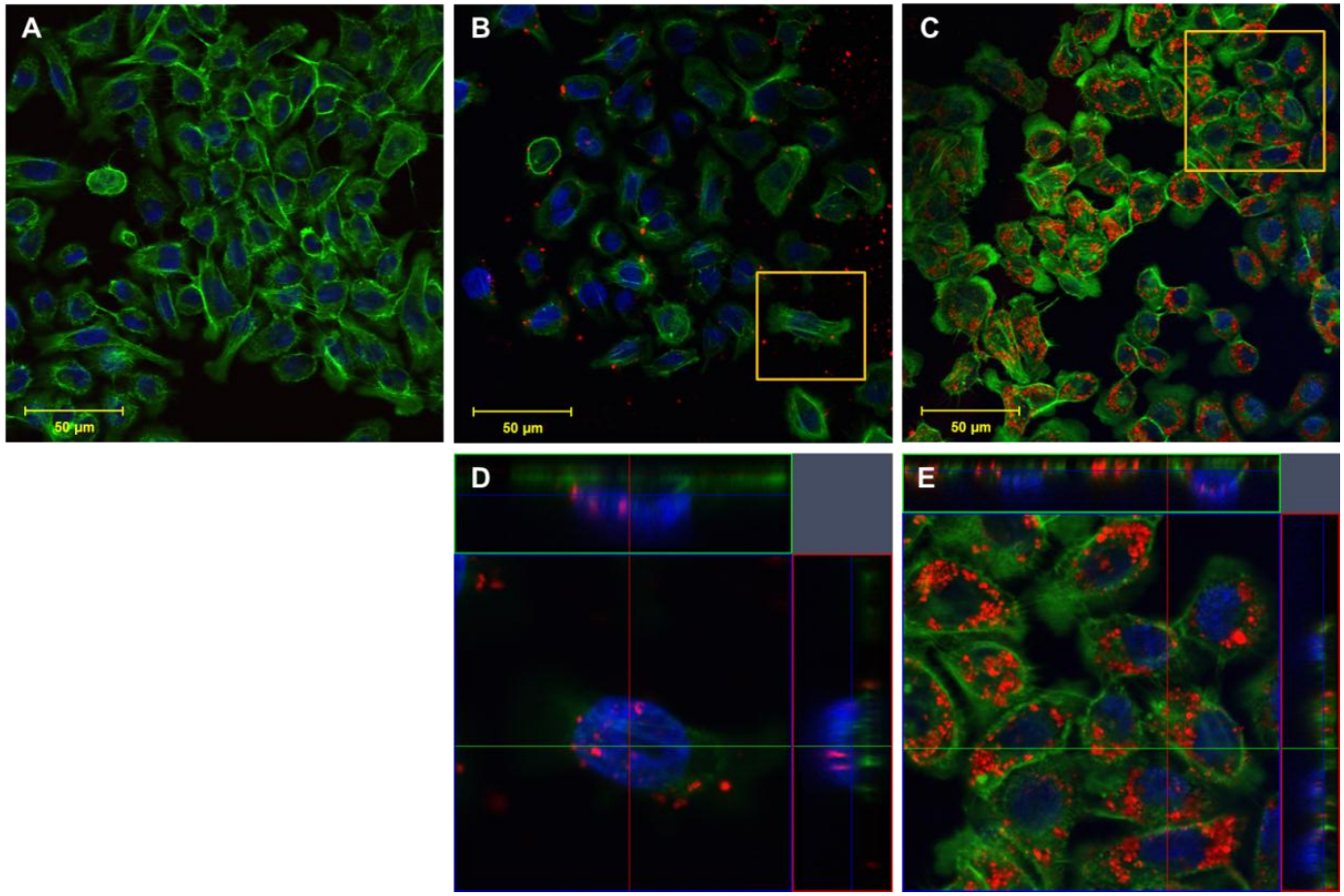


**Figure 11. AY-27 cellular uptake and binding after (A) 0 min, (B) 60 min, and (C) 24 h incubation with SWNH-QD complexes. (D) and (E) are orthogonal snapshots of the regions of interest in (B) and (C), respectively. The cross sections in the orthogonal images indicate SWNH-QDs within the nucleus and within the cytoplasm. Staining represented as: green = Oregon Green® phalloidin F-actin stain, blue = DAPI nuclear stain, red = SWNH-QD conjugates.**

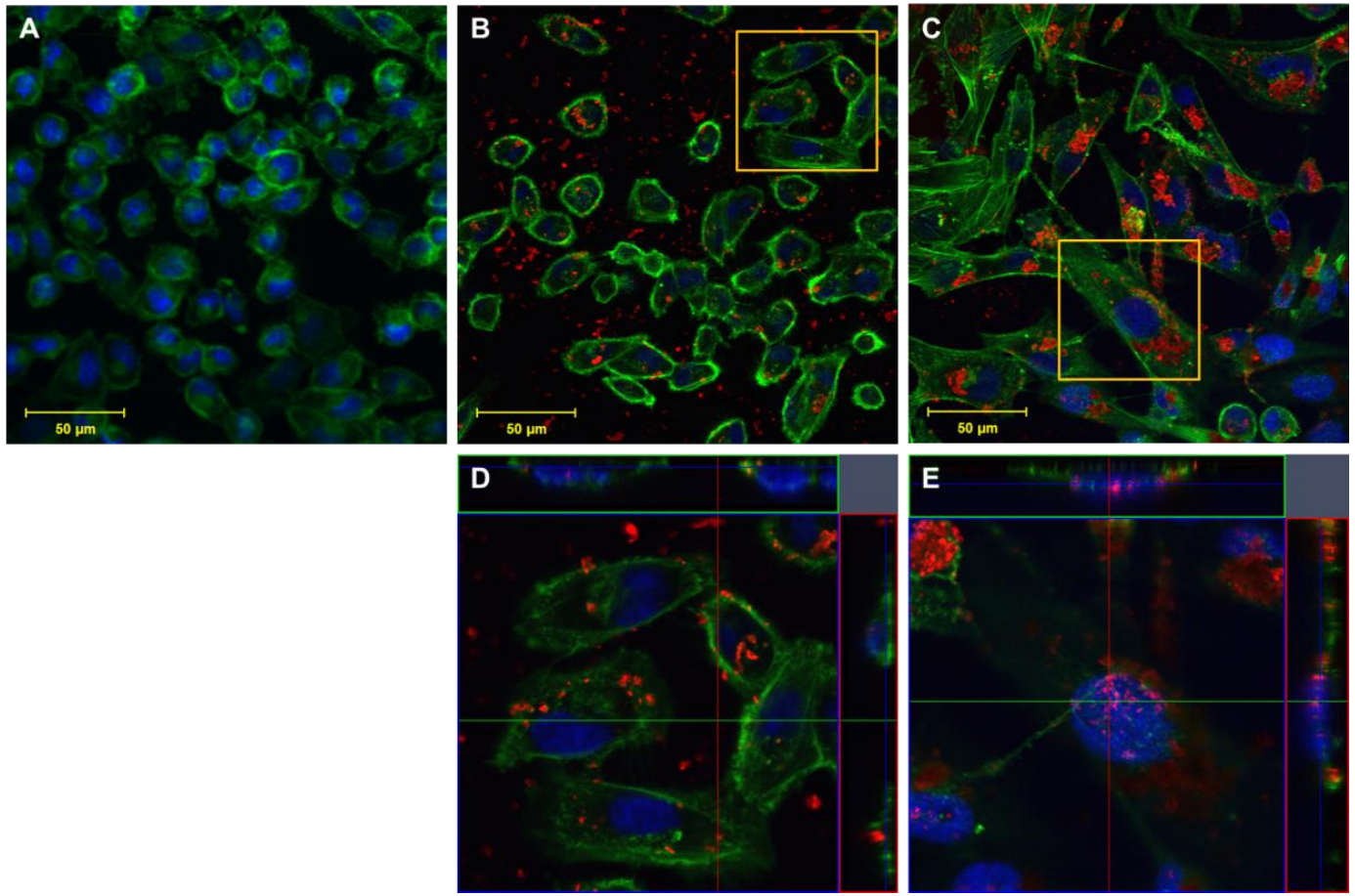


**Figure 12. MDA-MB-231 cellular uptake and binding after (A) 0 min, (B) 60 min, and (C) 24 h incubation with SWNH-QD complexes. (D) and (E) are orthogonal snapshots of the regions of interest in (B) and (C), respectively. The cross sections in the orthogonal images indicate SWNH-QDs within the nucleus and within the cytoplasm. Staining represented as: green = Oregon Green®phalloidin F-actin stain, blue = DAPI nuclear stain, red = SWNH-QD conjugates**

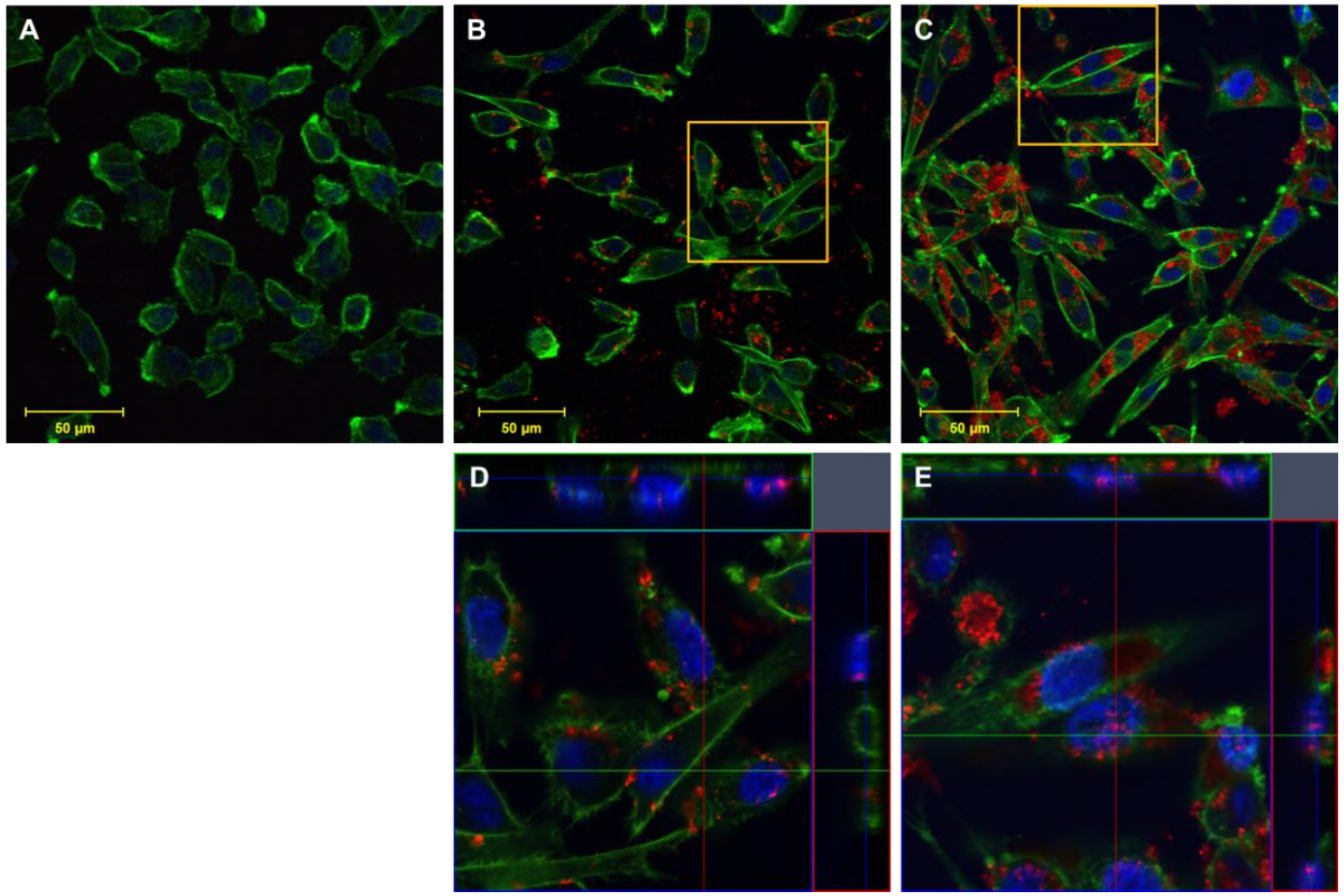


**Figure 13. U-87 MG cellular uptake and binding after (A) 0 min, (B) 60 min, and (C) 24 h incubation with SWNH-QD complexes. (D) and (E) are orthogonal snapshots of the regions of interest in (B) and (C), respectively. The cross sections in the orthogonal images indicate SWNH-QDs within the nucleus and within the cytoplasm. Staining represented as: green = Oregon Green® phalloidin F-actin stain, blue = DAPI nuclear stain, red = SWNH-QD conjugates**

### *2.6. Discussion*

Although other groups have investigated various procedures for conjugating QDs to single-walled and multi-walled carbon nanotubes (SWNT, MWNT) [27, 128-132], this is one of the first studies to characterize covalent attachment of QDs to SWNHs [110]. The carbodiimide method of conjugation used herein is not a new method for nanomaterial surface modification [113, 130, 131]; however, the novelty originates from developing a multi-dentate nanoparticle system for attachment of QDs using short linker molecules. This approach improves the interaction between SWNHs and QDs enhancing long-term stability. Previous studies with SWNTs have focused on conjugating carboxyl-functionalized tubes to amine-functionalized QDs [129, 142]. In those studies, QDs were either purchased as amine-functionalized QDs or as a QD powder with organic capping ligands. Each method has its drawbacks, with the pre-functionalized QDs being costly and possessing large diameters (upwards of ~40 nm), and the QD powder requiring a ligand exchange. In this study, QD powder was selected to minimize the size of the nanoparticle complexes. Traditionally, monothiols are used as capping ligands for QD surface modification; however, it has been shown that the thiol-ZnS interaction is labile [143]. When coupling QDs to nanoparticles for biomedical applications, it is important to consider such details because QD detachment is undesirable while monitoring transport.

Medintz *et al.* described that the use of poly-dentate thiolated ligands (*i.e.*, di-thiols) may improve stability [135]. However, these di-thiols are typically carboxylic acids, such as dihydrolipoic acid derivatives, requiring their dispersion solutions to have a basic pH. SWNHs in this study were thiol-functionalized to serve as a multi-dentate substrate using a short linker molecule to preserve the small particle size. When SWNH-

QDs were left in solution for 5 days, TEM images showed that SWNH-QDs which were synthesized using this multi-dentate approach (Figure 5) remained conjugated after 5 days (SI, Figure 17). However, within this time frame, QDs detached from the SWNH surface when QDs were first functionalized with the monothiol compound (AET) followed by conjugation to carboxyl-functionalized SWNHs via carbodiimide chemistry (SI, Figure 16 and Figure 17).

To further characterize this novel approach to covalent coupling, HRTEM and EDS confirmed the conjugation of QDs to the exohedral surface of SWNHs. The EDS spectra showed the presence of Cd, Zn, and Se, indicating the high contrast particles were QDs, in addition to S and N. These results suggest the AET linker compound has covalently coupled the two particles. SWNH-QD complexes were further characterized with UV-VIS and FL spectroscopy. The spectra of the complexes exhibited traits characteristic of both SWNHs and QDs. The FL spectra of the complexes compared to the spectra of QDs alone showed ~5 nm blue-shift in fluorescence emission. This shift could have been caused by either successful binding of thiol groups on the SWNHs [144, 145] or different dielectric constants of the solvents used in each particle suspension (SWNH-QDs suspended in water and QDs alone were suspended in chloroform). However, Wuister *et al.* performed a QD ligand exchange with hexanethiol in chloroform which resulted in a similar shift as that produced with *2*-aminoethanethiol in water, suggesting the shift observed after conjugation is indeed due to the ligand exchange [144]. Although each additional modification to the SWNH surface caused an approximate 50 nm increase in diameter, the nanoparticle size remained in the ideal range for delivery based on the enhanced permeability and retention effect [146, 147]. Zeta

potential (ζ) of a suspension is the measurement of electric potential between the particle and solution and is, therefore, often used as a measure of particle stability in solution. After conjugation, the zeta potential increased 20 mV compared to SWNHox, due to the decrease in free carboxyl groups to interact with the hydrophilic environment or the neutrality of the PEG-DSPE coating. Although an increase in zeta potential occurred following conjugation (more positive), the final complex zeta potential remains within the stable range, $\zeta < -15$ mV or $\zeta > +15$ mV [148].

Cytotoxicity analysis measured with an alamarBlue assay revealed no metabolic decrease after 3 h in all three cell lines or 24 h in the AY-27 or U-87 MG cell lines. A significant metabolic decrease was observed after 24 h for the MDA-MB-231 cell line (Figure 9). This decrease in metabolic activity may be characteristic of initial nanoparticle-cell interactions within the specific cell line. One study showed CNMs induced a toxic response after 24 h, but a repair process appeared after 48 h incubation [149]. Therefore, this may be an artifact of short viability time studies. This apparent toxicity may also be attributed the internalization of large SWNH-QD aggregates over the 24 h period, which may disrupt processes involved in metabolism or cell growth rate. A similar phenomenon was described by Raja *et al*. in the case of single-walled CNTs incubated with smooth muscle cells [141]. The increase in metabolic activity compared to non-treated controls observed in each cell line is most likely an artifact of CNM interference with the assay. Many standard assays currently used to evaluate toxicity cause enhanced reduction of the indicator, indicator adhesion to nanoparticles, or nanoparticle interference in absorbance or fluorescence measurements [150].

Visualizing carbon nanohorn transport was achieved through successful conjugation of CdSe/ZnS core/shell QDs. Estimation of cellular uptake rate was determined with flow cytometry. The percentage of cells containing SWNH-QD conjugates and median fluorescence intensity per cell was used to estimate and compare the uptake rates in the three malignant cell lines. Although much work has been done to study the uptake mechanisms, intracellular localization, and specificity of nanoparticles with various properties, these interactions remain poorly understood because of variability from group to group [151-153]. It is evident that the uptake efficiency and kinetics of SWNH-QDs are highly dependent on the cell type and may affect the delivery of the nanoparticle conjugates *in vivo* depending on the tumor type. U-87 MG cells exhibited the highest uptake rate, followed by the MDA-MB-231 and AY-27 cell lines, respectively (SI, Table 3). These findings are supported by dos Santos *et al*., where cellular uptake and localization of polystyrene nanoparticles of various sizes were studied in multiple (phagocytic and non-phagocytic) cell lines [88]. Further investigation is necessary to determine the uptake mechanisms and discrepancies between cellular uptake kinetics and efficiency. The U-87 MG cell line is highly infiltrative with its F-actin spreading across a larger area, followed by the MDA-MB-231 cell lines, and AY-27 cells respectively. As a result, a larger surface area of the U-87 MG cells are exposed for enhanced cellular uptake compared to the other two lines. Additionally, the doubling time and metabolic activity of each cell type may contribute to differences in SWNH-QD uptake rates; *i.e*., if a greater cell population grows during the 48 h plating time, there will be a lower particle to cell ratio.

Cellular distribution observed with confocal microscopy verified the presence of surface bound and internalized SWNH-QDs. After 60 min incubation, SWNH-QDs were primarily localized to the surface cytoplasm in all cell lines, with a few localized to the nuclei. After 24 h incubation, SWNH-QDs entered more readily into both the cytoplasm and the nuclei. Additionally, SWNH-QDs began to aggregate after 24 h, and despite the large sizes of the aggregates (few microns), the cells were still able to internalize them.

Although SWNH-QD transport was not evaluated in real-time for this study, QD photostability allows them to be continuously monitored without the risk of photobleaching. This is advantageous for implementation in 3D *in vitro* culture systems or *in vivo.* While Cd-containing QDs have many deleterious effects if not coated properly [121, 154], they were used to develop an effective conjugation scheme because of their high quantum yield compared to Cd-free QDs at visible wavelengths and commercial availability. However, the availability of Cd-Free QDs, such as indium phosphide QDs, is growing rapidly and could replace CdSe/ZnS core/shell QDs for *in vivo* uses in the future.

### *2.7. Conclusion*

SWNH-QD complexes were synthesized and characterized using thiol-functionalized SWNHs as a multi-dentate substrate, which improved conjugation stability compared to previous methods. This stable, covalent conjugation of QDs to SWNHs will permit the study of SWNH transport *in vivo* with confidence that QDs are not detaching from the SWNH surfaces. Non-phagocytic cells were shown to endocytose SWNH-QDs at substantial rates that were greatly dependent on cell type. Further investigation is

necessary to determine if each cell type uses the same endocytosis process or if there is another reason for the variability. These findings support the need for thorough cell-nanoparticle interactions prior to clinical implementation. The localization of SWNH-QDs within the cytoplasm and nuclei has significant potential for SWNH carriers as drug delivery systems. However, ligand or antibody targeting strategies should be employed in the future to improve the non-specific binding to reduce endocytosis in non-malignant cell lines. Advancements in studying SWNH transport in real-time will enhance the development of SWNH-based cancer therapies, such as laser-induced hyperthermia and chemotherapeutic drug delivery.

### *2.8. Acknowledgements*

The authors would like to thank Dr. David Geohegan at Oak Ridge National Laboratories for generously providing the single-walled carbon nanohorns for this research; Dr. Mitsu Murayama at Virginia Tech for his assistance with the TITAN TEM; Melissa Makris at Virginia Tech for her assistance with running the FACSARIA flow cytometer; and Dr. Harry Dorn, and Dr. Jianfei Zhang, Dr. Olga Ivanova, and Jay Tuggle for their collaboration with this project. Funding for this work was provided by the National Science Foundation Early CAREER Award CBET 0955072, the National Institute of Health Grant 1R21 CA135230-01, an Institute for Critical Technology and Applied Sciences (ICTAS, Virginia Tech) Grant, the National Institute of Health Grant R21 CA156078, the National Science Foundation Grant CBET 0933571, and the National Science Foundation Graduate Research Fellowship Program.

### *2.9. Supplemental Information to the Main Manuscript*

#### *2.9.1. PEG-DSPE Toxicity*

AlamarBlue was used to study the cytotoxicity of PEG-DSPE on MDA-MB-231 cells at various concentrations following manufacturer's protocol. Approximately 25,000 cells per well were seeded in TCPS 48-well dishes and incubated for 24 h (~70% confluent). Cells were then exposed to 0, 0.05, 0.1, 0.25, 0.5, 0.75, 1.0, or 2.0 mg/mL PEG-DSPE in DMEM/F12 growth media for 24 h (*n=3*). PEG-DSPE solutions were removed and cells rinsed once with PBS. Next, 500 μL of 10% alamarBlue in growth media was added to each sample and incubated for 3 h, and 100 μL aliquots from each sample were taken in triplicate and placed into a 96-well dish, totaling 9 readings per experimental group. Absorbance was measured with a SpectraMAX M2$^{e}$ microplate reader (Molecular Devices; Sunnyvale, CA) at 570 and 600 nm. Each experimental group (*n=3*) was tested and analyzed independently. The results were represented as the mean value ± sample standard deviation. Significance of results was verified with Student's t-test and a 95% confidence was used to determine statistical significance between groups. MDA-MB-231 cells were selected because they are a widely used cell line in our laboratory.

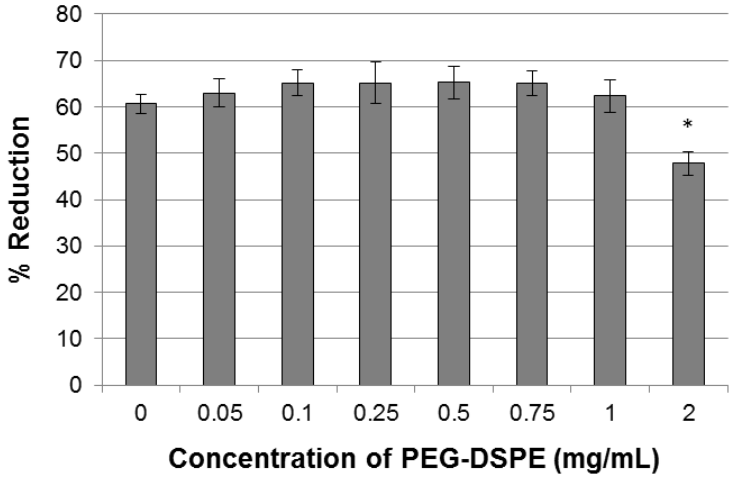


**Figure 14. alamarBlue assay of MDA-MB-231 cells treated with PEG-DSPE at various concentrations shows minimal toxicity at concentrations ≤ 1 mg/mL. *Denotes statistical significance for $p<0.05$.**

*2.9.2. Unfunctionalized Nanoparticle Control*

Pristine single-walled carbon nanohorns (SWNHs) were bath sonicated for 15 min in chloroform (0.25 mg/mL) and CdSe/ZnS powder (as-purchased) was suspended in chloroform by hand mixing (1 mg/mL). Equal volumes of SWNH and QD suspensions were mixed without reagents and the resulting solution was dried on a TEM grid. QD self-assembly was mainly observed (Figure 15A). Minimal QD assembly on SWNHs was observed as shown in Figure 15B and may be attributed to hydrophobic interactions upon removal of the solvent.

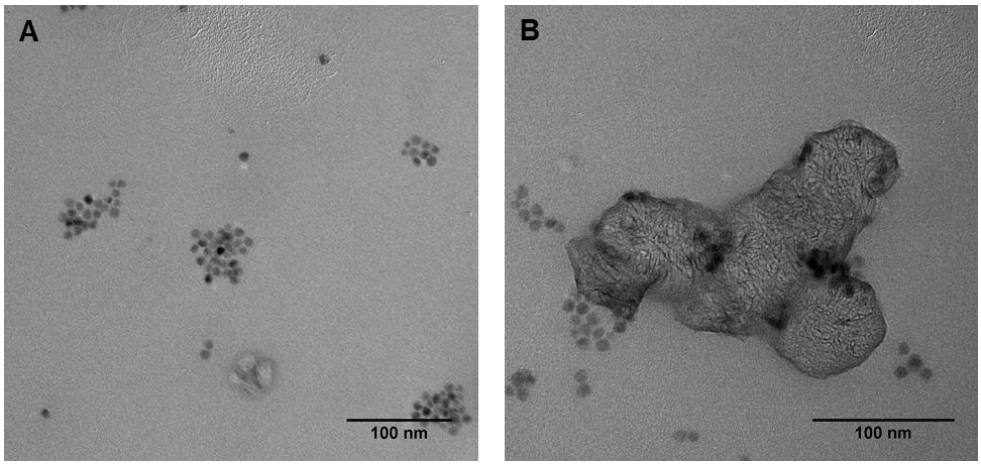


**Figure 15. Pristine SWNH and QDs (1:4 weight ratio) were physically mixed without reaction products (EDC, NHS, or AET) and analyzed with TEM to confirm minimal physioadsorption of QDs to exohedral SWNH surface. (A) Self-assembled regions of QDs were observed throughout the sample, which were not observed after SWNH-QD conjugation described in the manuscript. (B) SWNH aggregates had minimal QD physioadsorption upon physical mixing of nanomaterials.**

*2.9.3. SWNH-QD Conjugation Stability Experiment*

Single-walled carbon nanohorns (SWNHs) were also conjugated to quantum dots (QDs) using a more conventional method, similar to those used for single-walled carbon nanotubes (SWNTs) [130] and SWNHs [110] in previously published work (Figure 16). SWNHs were acid oxidized using the same procedures in the manuscript. Surface ligand exchange was then performed on as-purchased QDs. During this process, the QDs undergo surface ligand exchange at the phase interface, replacing the octadecylamine capping ligand with 2-aminoethanethiol (AET), creating amine-terminated QDs that are water dispersible (QD-AET). QDs were suspended in chloroform to a concentration of 1.0 mg/mL. Equal volume of 2.0 M AET was added to the solution and stirred vigorously for 24 h. The thiol containing end of AET forms a much stronger bond to the ZnS shell than the Zn-amine bond of the octadecylamine, causing it to be replaced. Subsequently,

equal volume sterile $dH_2O$ was added to the mixture and stirred vigorously for 24h to move QDs from the organic phase to the aqueous phase. Acid oxidized (SWNHox) were sonicated in sterile $dH_2O$ for 45-60 min to make a final concentration of 0.1 mg/mL. Then, 0.1 M EDC was added to the SWNHox suspension and stirred for 5 min, followed by the addition of 5.0 mM NHS. QD-$NH_2$ were then added to the reaction vessel (4:1 QD to SWNH weight ratio), pH was altered between 6.0 and 7.0 with 1.0 M HCl and stirred vigorously for 14-24 h at room temperature. The product (SWNH-QD(2)) was filtered with a 0.22 μm-pore nylon filter membrane and rinsed four times with $dH_2O$. The product was sonicated off the membrane filter for 1 min in sterile $dH_2O$. SWNH-QD(2) was then analyzed by TEM and compared to the SWNH-QD produced using the method in the main manuscript (SWNH-QD(1), Figure 5). Additionally, the conjugates were analyzed for stability over time. Conjugates were left in solution for 5 days and subsequently imaged with TEM.

SWNH-QD complexes, where modified QDs (QD-AET) and SWNHox were conjugated with EDC were not stable over 5 days (Figure 17B) as evidenced by the separation of QDs from SWNHs when dropped on the TEM grid. However, SWNH-QD complexes synthesized by thiol-functionalization remained conjugated after 5 days (Figure 17A).

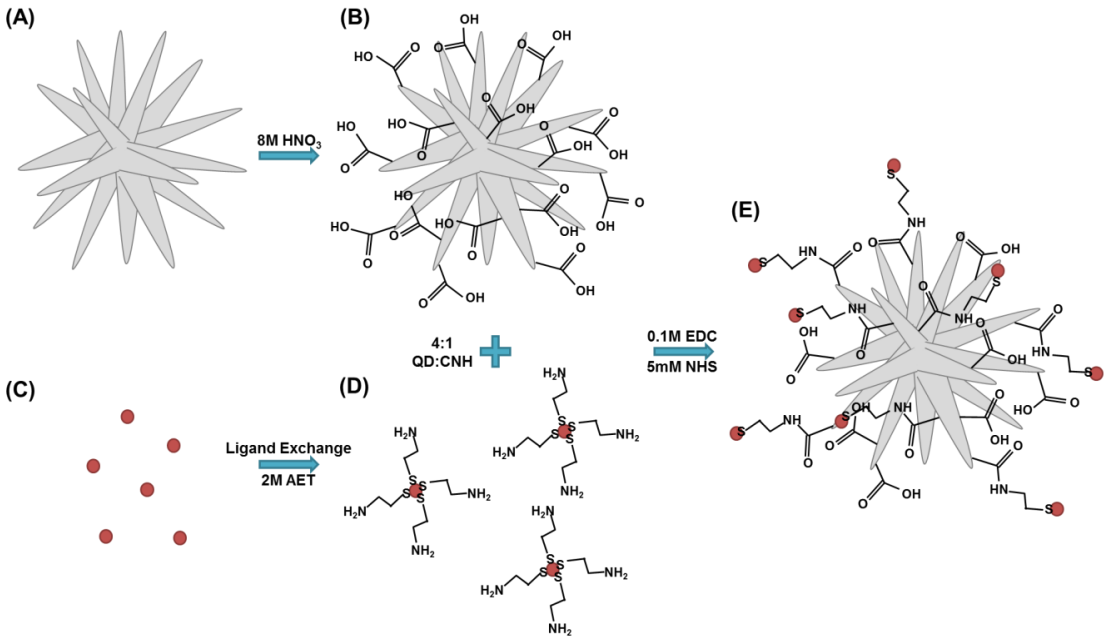


**Figure 16. Illustration of QD conjugation to SWNH exohedral surface using conventional method (Scheme 1). Pristine SWNHs (A) were acid oxidized to produce SWNHox (B). QDs (C) underwent surface ligand exchange to produce amine-functionalized water-dispersible QD-NH2 (D). Carbodiimide coupling was used to conjugate SWNHox and QD-$NH_2$ (E).**

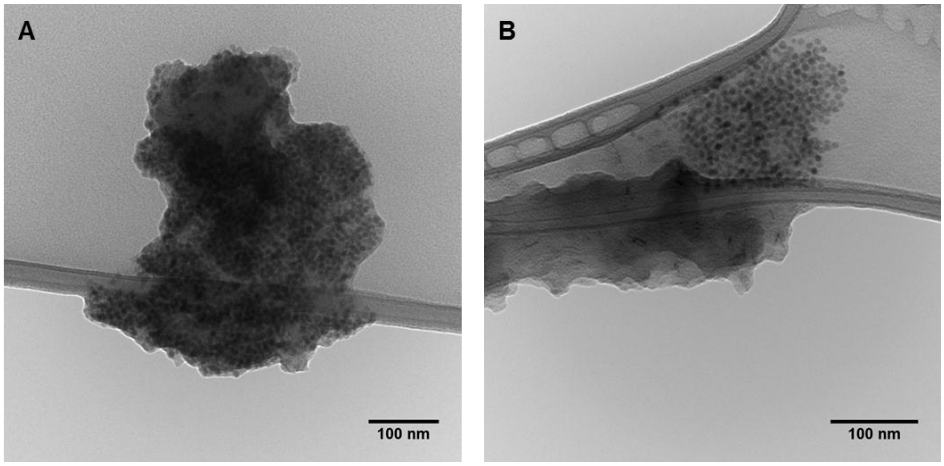


**Figure 17. TEM images of SWNH-QD conjugation products using (A) the multi-dentate approach discussed in the manuscript (Figure 5 in *Section 2.4.3*, SWNH-QD(1)) and (B) the traditional coupling approach discussed in this supplementary document (SI, Figure 16, SWNH-QD(2)).**

*2.9.4. Calculation of alamarBlue Percent Difference*

Percent difference of alamarBlue reduction compared to the non-treated control (*i.e.*, 100% difference is equal to 100% of that in the non-treated control groups) was quantified using the following equation:

$$\%\ Difference = \frac{(O_{600} \times A_{570}) - (O_{570} \times A_{600})}{(O_{600} \times P_{570}) - (O_{570} \times P_{600})} \quad \text{(E.S1)}$$

Where $O_{570}$= molar extinction coefficient of oxidized alamarBlue at 570 nm, $O_{600}$= molar extinction coefficient of oxidized alamarBlue at 600 nm, $A_{570}$= absorbance of test wells at 570 nm, $A_{600}$= absorbance of test wells at 600 nm, $P_{570}$= average absorbance of control wells at 570 nm, $P_{600}$= average absorbance of control wells at 600 nm.

*2.9.5. Flow Cytometry Side Scattering*

Side scattering information from flow cytometry provides information about the cellular internal complexity (Figure 18). The population of all cell lines shift from forward scattering to side scattering as the number of SWNH-QDs are internalized, *i.e.*, as median fluorescence intensity increases with time.

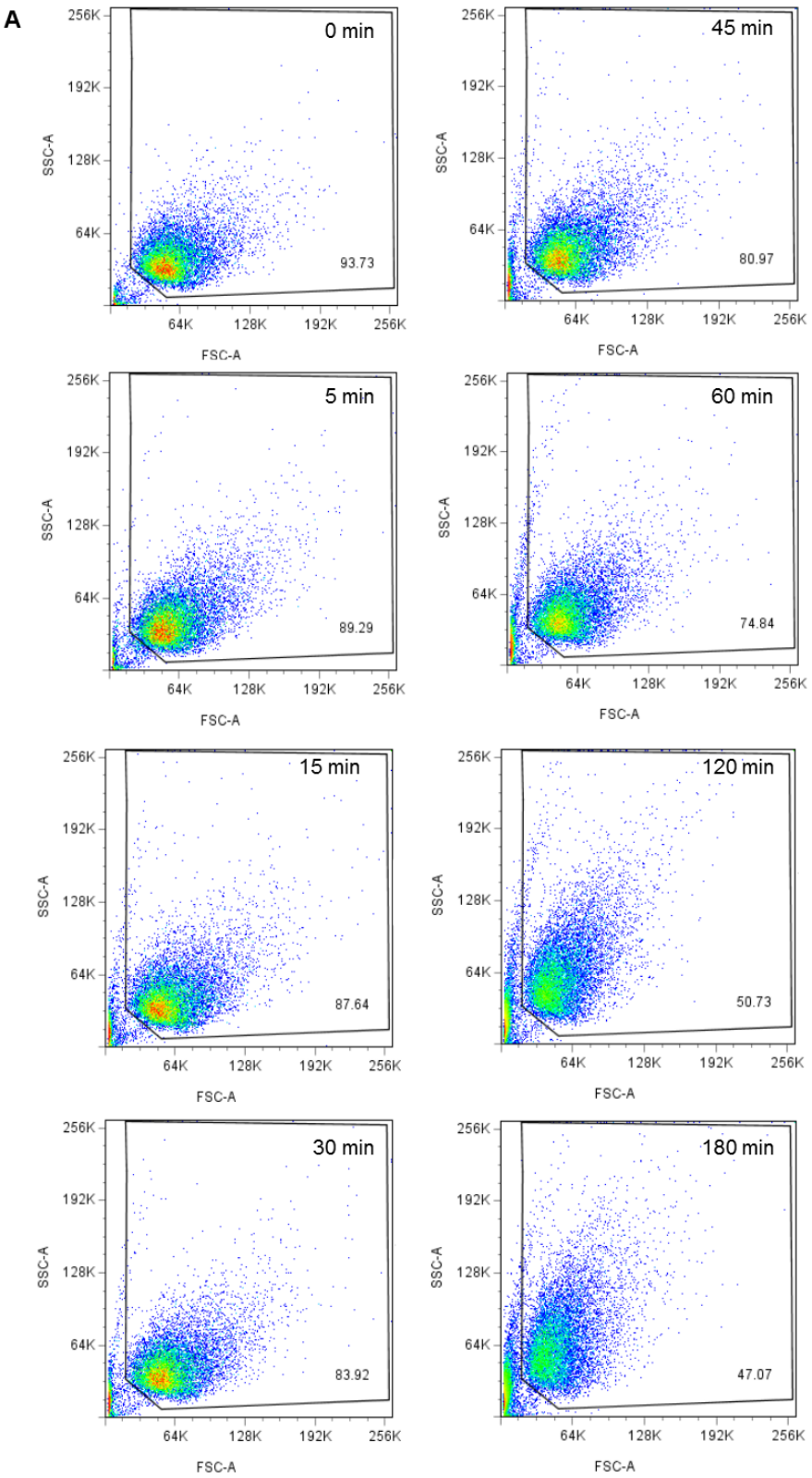
A
0 min
93.73
45 min
80.97
5 min
89.29
60 min
74.84
15 min
87.64
120 min
50.73
30 min
83.92
180 min
47.07
SSC-A
FSC-A
64K
128K
192K
256K

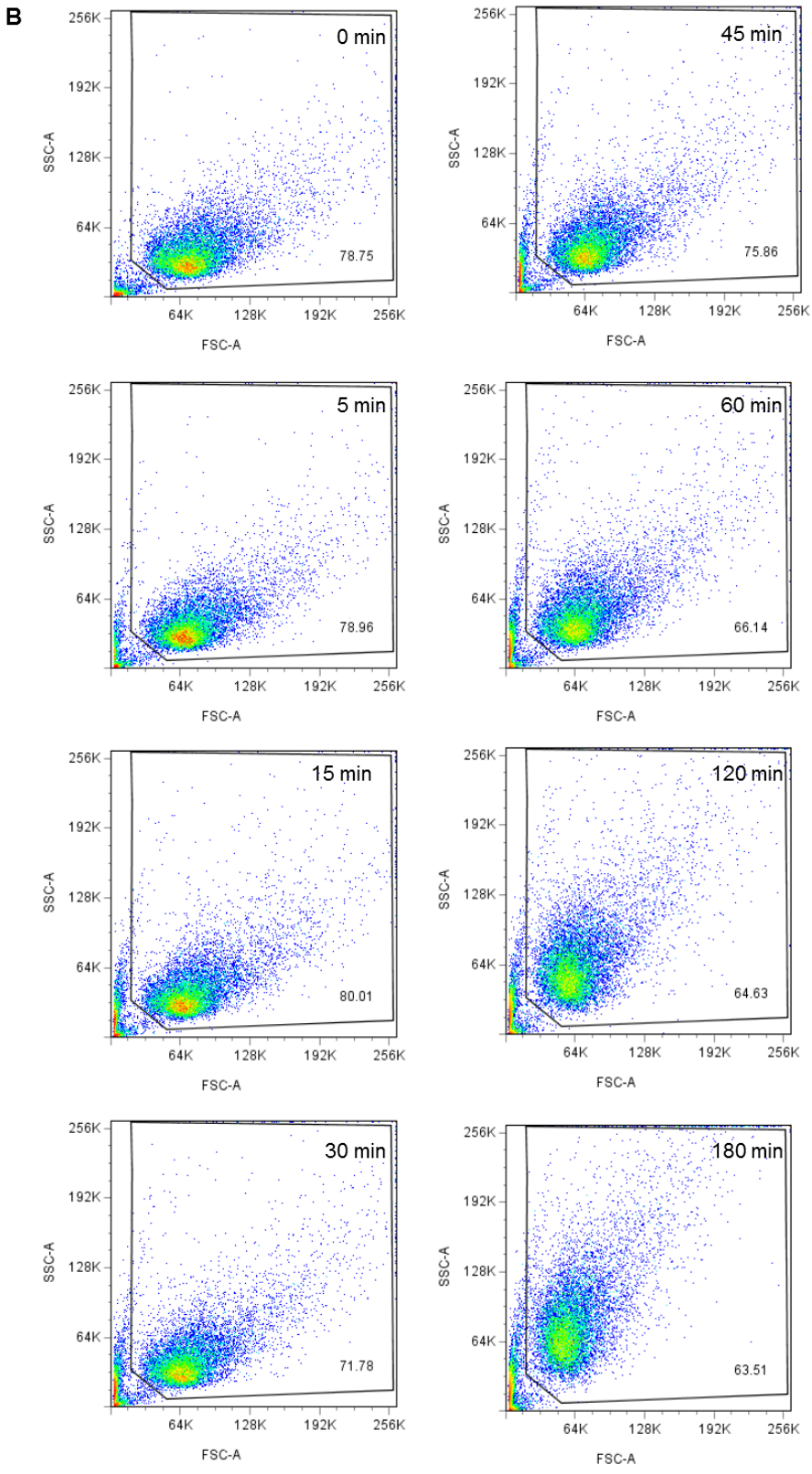
B
0 min
78.75
45 min
75.86
5 min
78.96
60 min
66.14
15 min
80.01
120 min
64.63
30 min
71.78
180 min
63.51
SSC-A
FSC-A
256K
192K
128K
64K

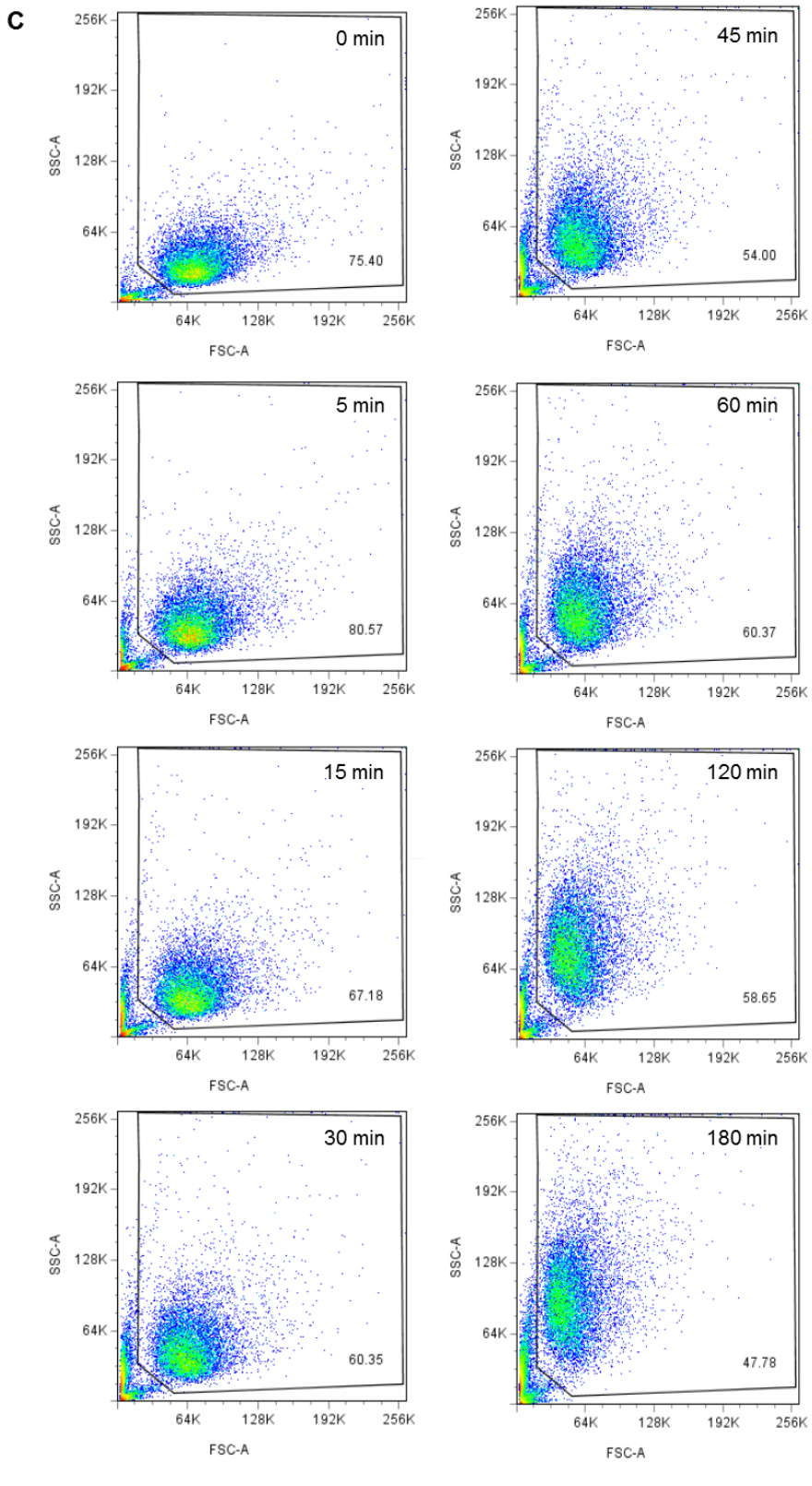


**Figure 18. Flow cytometry raw data side scatter vs. forward over 3 h for (A) AY-27, (B) MDA-MB-231, (C) U-87 MG cell lines.**

*2.9.6. Calculation of Uptake Kinetics and Efficiency*

**Table 3. Slopes of cellular uptake kinetics and uptake efficiencies determined by linear regression of the linear regions of the SWNH-QD uptake curves obtained by FACS. [a,b]Corresponding uptake curves are shown in Figures 5A and 5B.**

| Cell Line | Cell Type | Uptake Kinetics (% positive)[a] | Uptake Efficiency (median FL)[b] |
|---|---|---|---|
| AY-27 | Rat bladder transitional cell carcinoma | 0.70 | 5.52 |
| MDA-MB-231 | Human mammary gland adenocarcinoma | 1.54 | 21.9 |
| U-87 MG | Human glioblastoma | 2.73 | 36.5 |

# CHAPTER 3: CHEMOTHERAPY AND HYPERTHERMIA ALONE OR IN-COMBINATION FOR TREATMENT OF BLADDER TRANSITIONAL CELL CARCINUMO *IN VITRO*

## *3.1. Motivation*

Cancers of the brain and bladder are highly infiltrative diseases that typically invade the surrounding healthy tissue or form multiple tumors, respectively. The current standard for bladder cancer is the surgical resection of bulk tumors, followed by chemotherapy. Previous studies have shown that the use of mild hyperthermia has synergistic effects when used in combination with chemotherapy, compared to either chemotherapy or hyperthermia alone in other forms of cancer [155-158].

We hypothesize that the use of mild hyperthermia ($40 < T < 44°C$) would increase transport of chemotherapeutics to the intended site providing synergistic effects, whereas severe hyperthermia ($T > 50°C$) would induce cellular apoptosis in the bladder transitional cell carcinoma cell line. The goal of this study is to determine the lethal doses for chemotherapy, thermotherapy, and chemothermotherapy to develop an effective *in vitro* treatment regimen that could be translated to *in vivo* animal studies. The work presented in this chapter is fundamental to the progression of multi-modal therapies developed within our group [52]. The thermal lethal doses will be translated to carbon nanohorn concentrations and laser powers in future work. *This work is in progress and will be prepared as a manuscript for submission in the future.*

---

## *3.2. Introduction*

Each year, approximately 1.5 million people in the United States will be diagnosed with some form of cancer [3]. Urinary bladder cancers are the fourth most

common type of cancer among males and eleventh among females, with over 70,000 new cases and 15,000 deaths combined estimated in 2012 [6]. The disease prognosis has not improved over the past ten years, as have many other forms of cancer. In 1999, over 54,000 new cases and 15,000 deaths were estimated [159] suggesting advancements in the treatment and diagnosis of UCCs are limited. Approximately 90% of urinary bladder cancers are transitional-cell carcinomas (also known as urothelial transitional cell carcinoma, UCC), which are characteristic of single or multiple tumors throughout the bladder epithelium or urinary tract [8, 160]. Seventy percent of UCCs are superficial with a 50-70% recurrence after resection [161]. UCCs often begin in the bladder mucosa and as the disease progresses from superficial to invasive, the tumors move through the lamina propria, muscularis propria, to the pervesical fat [162]. Upon further development, lymph node involvement increases, following metastasis into surrounding organs.

The current treatment standard for superficial UCCs is transurethral resection; however, tumor recurrence is common [161]. Therefore, intravesical chemotherapy typically follows surgical resection, commonly with the use of doxorubicin, mitomycin-C, or epirubicin [161]. Radical cystectomy is the standard treatment for high-grade, invasive UCCs, though it is also used if transurethral resection and chemotherapy fail to improve the prognosis of superficial tumors [161-163]. Radical cystectomy often results in high patient morbidity, as the bladder, prostate, and seminal vesicles are removed in men or the uterus, fallopian tubes, ovaries, and urethra are removed in women [163]. The development of new therapeutic strategies is imperative to improve patient morbidity and prognosis of both superficial and invasive UCCs.

One interesting approach is the use of laser-based hyperthermia or hyperthermia in combination with chemotherapy. The use of hyperthermia for cancer treatment *in vivo* is based upon the selectivity between normal and malignant tissues due to differences in pH and vascularization. Under mild hyperthermic conditions, normal tissues have homogeneous vascularization allowing for efficient dissipation of heat. However, in tumor tissue, vascularization is heterogeneous often leaving regions avascular and unable to regulate temperatures [92, 97]. Mild hyperthermia is shown to also potentiate the effects of chemotherapy in melanomas, cervical carcinomas, and retinoblastomas [156, 164, 165]. Severe hyperthermia, on the other hand, may induce complete tumor ablation, if delivered selectively [166].

Platinum-containing compounds, such as cisplatin and carboplatin, are among the most commonly used chemotherapeutic agents to treat many forms of cancer, including ovarian cancer, lung cancer, head and neck cancer, and bladder cancer [167]. Cisplatin and carboplatin were the first platinum-containing analogs introduced clinically, each having substantial different toxicity profiles [167, 168]. Carboplatin has less toxic side effects compared to cisplatin because the structure is less reactive toward nucleophilic DNA sites [168]. Doxorubicin is another commonly used chemotherapeutic agent for the treatment of bladder cancer, breast cancer, bone cancer, Kaposi's sarcoma, stomach cancer, etc. [161, 169, 170]. Each of these chemotherapeutic agents binds to DNA causing decreased replication, ultimately inhibiting proliferation; however, the mechanism of DNA interaction is different. Cisplatin undergoes hydrolysis causing chlorine groups to be displaced by water, generating an electrophilic reactive species that can bind to nucleophilic sites of DNA. Carboplatin, on the other hand, is thought to

undergo enzymatic activation *in vivo* [168]. Doxorubicin is an anthracycline that forms an intercalation complex with DNA by binding to base pairs of the DNA [171]. Other groups show induction of reactive oxygen species and mitochondrial apoptosis, causing multi-modal toxicity as a result of doxorubicin treatment [170]. As a result, these different chemotherapeutic agents may have different synergistic potential with when used as an adjuvant to hyperthermia.

Recent work by our group to develop novel devices for the simultaneous delivery of chemotherapeutic agents or nanoparticles and light in a localized manner may advance the clinical treatment strategies of invasive UCCs [52]. However, *in vivo* animal models must be performed prior to their clinical translation. This study provides a basis for determining *in vivo* treatment plans and to determine the efficacy of chemothermotherapy in UCCs. In this study, a bladder transitional cell carcinoma cell line, AY-27, was used to evaluate and predict the therapeutic lethal doses of chemotherapy or hyperthermia alone and in combination *in vitro*.

### *3.3. Materials and Methods*

#### *3.3.1. Cell Culture*

The effects of various chemotherapy (CT) agents were evaluated in *N*-(*4*-[*5*-nitro-*2*-furyl]-*2*-thiazolyl) formamide induced rat bladder transitional cell carcinoma cells, AY-27 cells, originally developed by Dr. S. Selman and Dr. J. Hampton (Medical College of Ohio, Toledo, Ohio) and kindly donated by Dr. John Robertson (Virginia Tech, Blacksburg, VA). AY-27 cells were maintained in a humidified atmosphere at 37°C, 5% $CO_2$, and 95% air and cultured with Roswell Park Memorial Institute (RPMI) 1640

medium supplemented with 10% fetal bovine serum, 1% penicillin-streptomycin. Cells were split every 4 days prior to confluence.

*3.3.2. Chemotherapy Treatment*

Cells were seeded in 6-well tissue culture polystyrene dishes at 100,000 cells per well and were incubated for 24 h to reach their exponential growth phase. The therapeutic effect of cisplatin (*cis*-diamminedichloroplatinum(II), CDDP) (EMD Millipore; Billerica, MA), carboplatin (*cis*-diammine(1,1-cyclobutanedicarboxylato)platinum(II), CBP) (Hospira; Lake Forest, IL), or doxorubicin ((*7S,9S)-7*-[(*2R,4S,5S,6S*)-*4*-amino-*5*-hydroxy-*6*-methyloxan-*2*-yl]oxy-*6,9,11*-trihydroxy-*9-(*2-hydroxyacetyl)-*4*-methoxy-*8,10*-dihydro-*7H*-tetracene-*5,12*-dione, DOX) (Sigma-Aldrich; St. Louis, MO) were evaluated in this study. Chemotherapeutic dosages were selected based on clinically-relevant doses. Maximum doses, or clinically-relevant doses, of 100 mg/m$^2$ were selected for CDDP and DOX, while 300 mg/m$^2$ was selected for CBP. Lower doses of 10 and 50% of the maximum doses were also evaluated. These doses were translated to molar concentrations for each drug based on the percentage of the maximum dose, outlined in Table 4. Cell culture media was removed and cells were exposed to 0, 10, 50, and 100% of the clinically relevant doses of CDDP, CBP, or DOX for 2, 4, and 24 h (*n=3*). After the intended time, cells were rinsed once with phosphate buffered saline solution (PBS) (Thermo Scientific; Logan, UT). Fresh culture media was then added and cells incubated for a 24 h recovery period from the time of treatment.

**Table 4. Drug conversion from clinical dosage to molar concentration.**

| Drug | 10% | 50% | 100% |
|---|---|---|---|
| *Cisplatin* | 10.7 μM | 53.5 μM | 107 μM |
| *Carboplatin* | 26 μM | 130 μM | 260 μM |
| *Doxorubicin* | 5.5 μM | 27.5 μM | 55 μM |

*3.3.3. Cell Viability*

Cell viability and count were analyzed following recovery using trypan blue exclusion quantified with a Vi-CELL Cell Viability Analyzer (Beckman Coulter; Indianapolis, IN). Sample collection was as follows, cell media was collected, to account for the apoptotic population, and adherent cells were removed with 0.25% trypsin-EDTA (Invitrogen; Grand Island, NY). PBS was added to the previously collected media. The wells were rinsed once with PBS to ensure all cells were collected. Cell suspensions were centrifuged at 120 G for 5 min at 4°C, the supernatant was aspirated, and the remaining pellet was resuspended in 1 mL of PBS. The lethal concentration ($LC_{50}$) of each chemotherapeutic agent for each exposure time was determined using linear regression.

### *3.4. Results and Discussion*

Cisplatin, carboplatin, and doxorubicin each had dose- and time-dependent responses on AY-27 proliferation. Each yielded a decrease in proliferation; however, with varying efficacy. Cisplatin provided enhanced cell death and reduction in proliferation compared to carboplatin, an analog of cisplatin (Figure 19). Carboplatin is less cytotoxic than cisplatin, which is well supported by other studies [167, 172, 173]. In a study comparing efficacy of cisplatin and carboplatin in ovarian cancer, carboplatin had markedly fewer side effects, such as limited neurotoxicity, while inducing a similar tumor response [172]. However, a study using cocktails of four chemotherapeutics either

containing cisplatin or carboplatin for the treatment of metastatic bladder cancer, the cisplatin-containing cocktail was more efficacious than the carboplatin-containing cocktail. Though the latter had reduced gastrointestinal, renal, neurologic, and otologic toxicity associated [174]. Higher doses than those investigated in this study may be necessary for the treatment of UCCs. Although carboplatin is less effective than cisplatin using these concentrations, the combination of carboplatin with an adjuvant therapy, such as hyperthermia, may potentiate its effect for the treatment of UCCs.

Doxorubicin induced immediate reduction in cellular proliferation at low concentrations. Its cytotoxic effect plateaued with increasing concentration, whereas the platinum containing drugs decreased with increased concentration. On the other hand, longer exposure times continued to enhance toxicity using all three chemotherapeutic agents. The doxorubicin 4 h group has an irregularity compared to the other trends; therefore, this data set should be repeated (Figure 19). The cell viability is not an adequate measure of toxicity using these three agents because they interact with DNA causing decreased proliferation; therefore it was not reported herein.

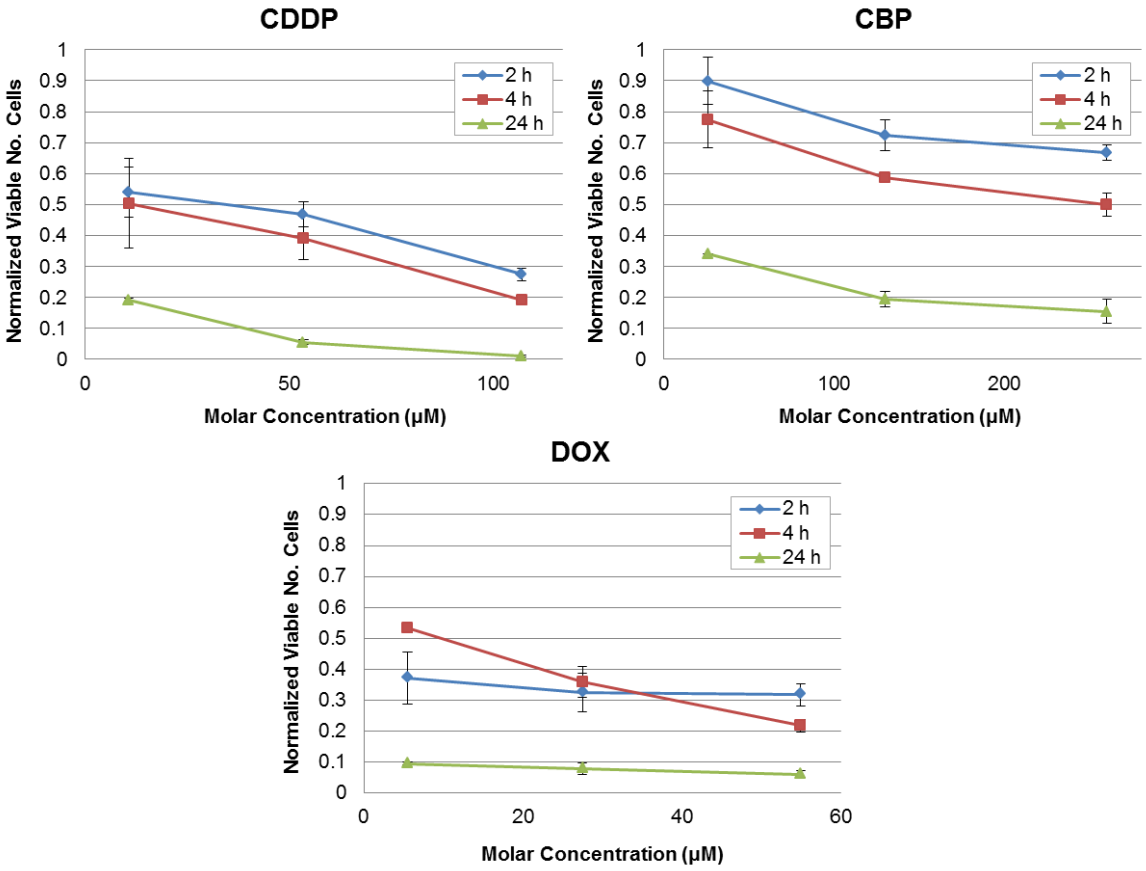


**Figure 19. Concentration-response curves for AY-27 cells exposed to CDDP, CBP, or DOX for varying times (*n*=3). Data is normalized to a positive control group (media-only) for each chemotherapy agent.**

The lethal concentrations to obtain approximately 50% cell death ($LC_{50}$) were determined for each exposure time of each drug and reported in Table 5. This measurement serves as a guideline for *in vivo* animal testing. Greater than 50% cell death was achieved with the minimum concentration for each of the agents investigated after 24 h exposure time.

Previous work demonstrates the synergistic effects of hyperthermia (HT) to increase the chemotherapeutic response [100, 156, 158, 175]. Therefore, a similar response is expected using cisplatin, carboplatin, and doxorubicin in the AY-27 rat bladder transitional cell carcinoma cell line. The synergistic effect depends on the CT

agent, the cell line used, and the dosages of CT and HT. As described by van der Heijden *et al*., each chemotherapeutic agent has a different synergistic response to HT. They found that epirubicin, an analog of doxorubicin, had the most significant synergistic effect with HT compared to mitomycin C, gemcitabine, and indoloquinone EO9 [100].

**Table 5. Lethal dose-50% of CDDP, CBP, or DOX at various exposure times.**

| *Drug* | *Exposure Time (h)* | *$LC_{50}$ (μM)* |
|---|---|---|
| Cisplatin (CDDP) | 2 | 31.1 |
| | 4 | 14.8 |
| | 24 | * |
| Carboplatin (CBP) | 2 | 398 |
| | 4 | 234 |
| | 24 | * |
| Doxorubicin (DOX) | 2 | * |
| | 4 | 8.9 |
| | 24 | * |

* Denotes >50% cell death at this exposure time

### *3.5. Future Work*

In addition to the study of chemotherapeutic efficacy in the treatment of rat transitional cell carcinoma lines, efficacy of hyperthermia (HT) alone and its synergistic effect with chemotherapy (CT) has yet to be determined for this cell line. The development of treatment regiments *in vitro* is fundamental toward the progression of *in vivo* animal-model treatments, which will then be translated to the clinic. The use of HT and CT may have synergistic therapeutic effects; however, determination of lethal doses-50% ($LD_{50}$) for HT, CT, and combinations are necessary. SWNHs may have an added effect in improving the delineation between cytotoxic responses in malignant versus normal tissues and may locally potentiate the effects of chemotherapeutic agents.

*3.5.1. Hyperthermia and Combined Chemothermotherapy Treatments*

As a continuation to the study outlined in *Sections 3.3 and 3.4,* AY-27 cells will be exposed to a range of thermal doses, from mild to severe hyperthermia (40 – 60°C), and exposure times (seconds to hours). Incubator heating will be utilized to ensure adequate gas-exchange conditions are maintained. Cells in culture dishes will be placed in small volumes of water to ensure uniform heating within the incubator. Heating medium, consisting of RPMI 1640 without L-glutamine or phenol red, will be utilized during these experiments to limit heat shock protein expression and prevent thermotolerance. Lethal doses to achieve 50% and 10% cell death ($LD_{50}$, $LD_{10}$) using hyperthermia will be evaluated and reported for specific exposure times and temperatures.

Additionally, the synergistic effects of chemothermotherapy (CT+HT) will be analyzed. Appropriate drug concentrations in heating medium will be prepared and heated to the target temperature in a water bath. Growth medium will be exchanged with heating medium and cells will be placed in a heated incubator. Sample collection and analysis will be similar to that described in *Section 3.3.3.* Additionally, the effect of the chemotherapeutic agents and hyperthermia will also be evaluated with a PicoGreen DNA quantification assay to evaluate proliferation. This assay will provide an accurate measurement of toxicity, which will then be compared to the cell viability technique outlined in *Section 3.3.3.* The thermal enhancement ratio (TER) will be determined as a method to evaluate synergism, as is common in many previous studies [93, 156, 175, 176]. A TER greater than 1 denotes synergism of the combined therapies.

*3.5.2. Determination of Synergistic Effect Mechanism*

Although the synergistic effect of CT+HT has been reported previously, the synergistic mechanism is not well known. The cellular uptake of the chemotherapeutic agents can be evaluated by either inductively-coupled plasma atomic emission spectroscopy (ICP-AES) (cisplatin and carboplatin) or fluorescence spectroscopy (doxorubicin) before and following HT to determine if HT is causing cellular uptake of the drug to increase.

## *3.6. Conclusions*

Cisplatin, carboplatin, and doxorubicin each have a different time and dose-dependent effect on cellular proliferation. The use of hyperthermia to enhance these effects in AY-27 cells remains to be investigated. The use of *in vitro* models to predict and develop treatment regiments eliminates the use of excessive animals *in vivo*. Although the *in vivo* responses do not always match *in vitro* results, the clinician can build upon this foundation. The combination of hyperthermia with chemotherapy may potentiate the effects of cisplatin, carboplatin, or doxorubicin at lower concentrations in UCCs, in addition to enhancing drug permeability throughout the tumor interstitium.

# CHAPTER 4: SUMMARY, FUTURE PROSPECTS, AND OTHER PRELIMINARY WORK

## *4.1. Summary*

This research was conducted to obtain fundamental knowledge of nanoparticle (*Chapter 2*) and chemotherapeutic (*Chapter 3*) interactions with cells *in vitro* to enhance current strategies for the treatment of cancer. The scope of the first study was to (1) synthesize and characterize a fluorescently labeled SWNH conjugate and (2) to gain an understanding of SWNH transport in multiple malignant cell lines. SWNH-QDs were successfully synthesized and the conjugation stability in solution was improved compared to previously established methods using the same linker compound [110]. Optical visualization of SWNH-QDs promotes the real-time, dynamic, and non-invasive evaluation of SWNH transport in biological systems. The localization of SWNH-QDs to the cytoplasm validates the use of SWNHs for drug or even gene delivery for the treatment of cancer.

Additionally, this biodistribution may also impact SWNH-enhanced photothermal therapy because SNWHs localized within the cytoplasm and nucleus may induce reactive oxygen species to enhance cellular apoptosis. SWNH-QDs, as most other nanoparticles, can be internalized by non-phagocytic cells and their uptake rates and efficiencies are dependent on cell type. Tumor type may affect the intracellular transport to such a degree, where specific nanoparticle designs should be used to target certain types of cancer. Although long term toxicity was not evaluated, SWNH-QDs can be used as a tool for quantification purposes prior to the use of SWNHs clinically for short term transport investigation. The conjugate system developed in *Chapter 2* can be further utilized to

understand SWNH bulk tissue transport through *in vitro* tumor models and *in vivo.* The use of QDs as the fluorescent probe allows for the fluorescence emission wavelength to be altered for *in vivo* applications (*i.e.*, near-infrared wavelength) to overcome the tissue scattering limitation associated with other fluorophores.

The goal of the second study was to characterize the chemotherapeutic efficiency of three agents commonly used clinically for the treatment of cancer. Each agent had a positive killing effect with increased concentration and exposure time for the rat bladder transitional cell carcinoma cell line. The influence of various chemotherapeutic agents for the treatment of this cell line has not been widely characterized. Eventually, the use of hyperthermia alone or in-combination with chemotherapy for inducing apoptosis in this cell line will serve as a guideline for the treatment of AY-27 cell-induced rats using a novel local therapeutic delivery system [52]. Additionally, this study serves to determine which chemotherapeutic agent may have the most significant effect if delivered with SWNHs. The use of hyperthermia may not only potentiate the effects of the chemotherapeutic agent, but it may also enhance delivery of future SWNH-based drug delivery systems.

### *4.2. Future Prospects*

An advantage to using a photoabsorptive material as a nano-carrier is the ability to induce localized temperature increases [15, 16, 90]. This may be beneficial for tumor ablation or it may improve SWNH and chemotherapeutic agent transport, such as enhanced cellular permeability or vascular permeability [93-95, 177]. Hyperthermia-enhanced SWNH transport and hyperthermia-enhanced chemotherapeutic toxicity should

be thoroughly investigated as potential advantages to the uses of SWNHs in cancer therapy. Though SWNTs remain among the most commonly researched CNMs for biological applications, SWNHs have potential benefits over SWNTs as outlined by the preliminary work described in the following section. Many studies fail to compare CNM efficacies; therefore, future work should be conducted to comprehensively evaluate the size and shape effects of SWNHs and other CNMs on toxicity, cellular transport, drug loading capacity, etc.

The SWNH-QD conjugates developed in this study can be used to study the real-time, dynamic transport of SWNHs *in vitro* prior to monitoring bulk transport *in vivo*. Additional staining of intracellular organelles, followed by paraffin embedding, sectioning, and TEM of cells may provide a more thorough understanding of SWNH-QD intracellular compartmentalization and endocytosis mechanism. Chemotherapeutic agents which act on SWNH-localized cellular compartments can be loaded into SWNHs for effective delivery. Some preliminary experiments involving the loading of cisplatin into the internal SWNH pores is described in the following section.

Novel conjugation schemes can also be investigated to provide enhanced particle stability and potentially minimize particle size. Other work describes the use of di-thiols [178-181] or imidazole rings [182, 183] to stabilize QDs in aqueous environments. Finally, additional targeting mechanisms should be implemented in the nano-carrier design to reduce non-specific binding and internalization of nanoparticles in tissues outside of the tumor mass, such as the incorporation of folic acid.

### *4.3. Additional Preliminary Work Related to Future Work*

#### *4.3.1. SWNH vs. SWNT Cellular Uptake*

A preliminary experiment comparing cellular uptake rate and efficiency of SWNHs and SWNTs was performed to determine if endocytosis was affected by nanoparticle geometry for CNMs. Briefly, SWNHs and SWNTs were oxidized using a high speed vibration milling method where succinic acid acyl peroxide was added to the CNMs in a 1:1 ratio and was mechanically milled for 2 hours. Thorough washing with acetone removed excess peroxide. Despite the capability of this solid state reaction procedure, we moved towards liquid phase oxidation to reduce potential toxicity associated with residual peroxide in pore spaces. The method for QD conjugation described in *Section 2.9.3* was used in this study. Similar procedures were used for flow cytometry analysis as detailed in *Section 2.4.6.*

Absorbance was also measured for pristine SWNHs and SWNTs to determine if SWNHs may have added absorbance due to their large surface areas. SWNH and SWNT samples for absorbance measurements were prepared by suspending particles in a 1% (*w/v*) Pluronic-F127 solution (BASF Chemicals; Florham Park, NJ). CNM absorbances were measured in 1x10 mm quartz cuvettes using a Cary 5000 Spectrophotometer (Varian, Inc.; Santa Clara, CA) using a diffuse reflectance accessory (DRA 2500, Varian, Inc.; Santa Clara, CA).

Although SWNHs and SWNTs were found in approximately 80-90% of the MDA-MB-231 breast cancer cellular population after 60 minutes of nanoparticle incubation, SWNHs were internalized much quicker than SWNTs as observed by the median fluorescence intensity (Figure 20) and side scattering information (data not

shown). These findings are supported by other work where spherical shaped structures are more readily endocytosed than rod shaped structures [29, 54].

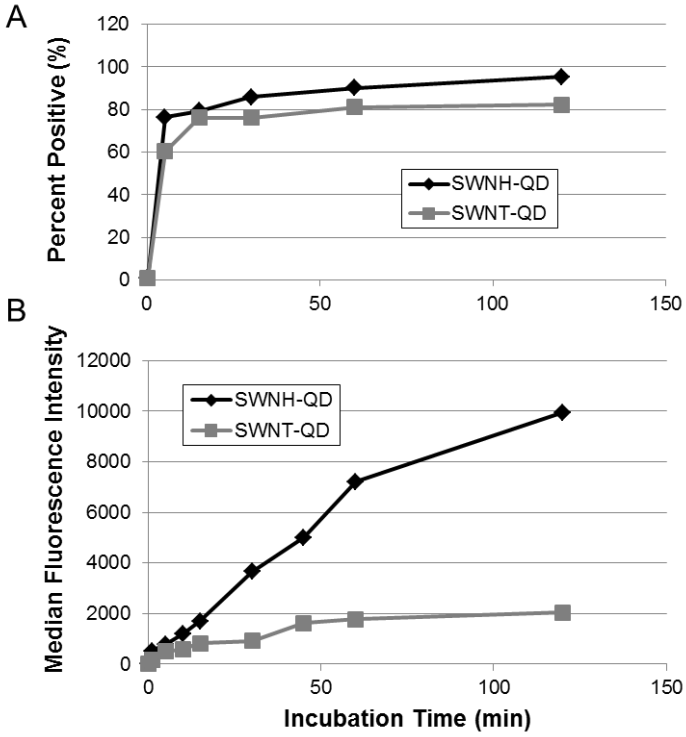


**Figure 20. CNM geometry effects cellular uptake rate and efficiency in MDA-MB-231 cells incubated with 0.025 mg/mL SWNH-QD or SWNT-QD over 3 h. FACS data represented as (A) the percentage of cells containing SWNH-QDs in the population measured and (B) median fluorescence intensity of the cell population.**

Currently, carbon nanomaterials are highly researched for biomedical applications; however, limited studies have been conducted to compare SWNH to SWNT/MWNTs. SWNHs may have superior properties to SWNTs and MWNTs, such as greater surface area for improved drug loading, optimal shape and size to overcome transport barriers, and higher absorbance in the near infrared (NIR) optical window for enhanced photothermal therapy (Figure 21).

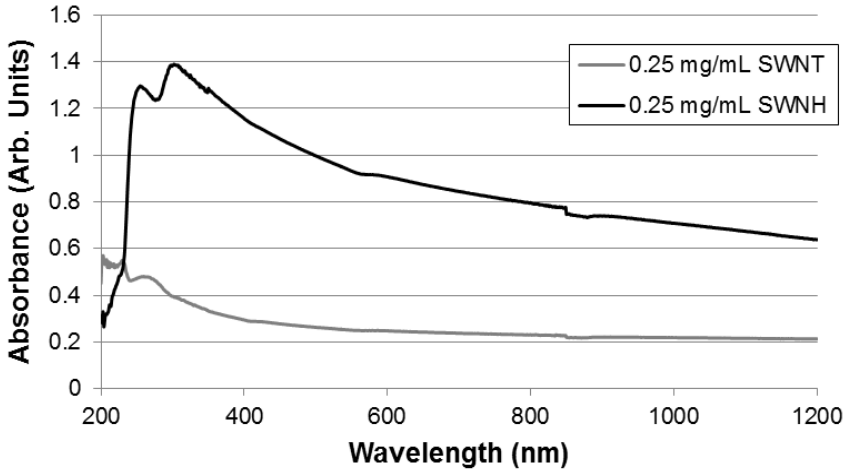


**Figure 21. Absorbance of SWNHs and SWNTs. SWNH diameter was 80-100 nm and SWNTs were approximately 1-3 nm in diameter and 900-1200 nm in length.**

*4.3.2. Chemotherapeutic Drug Loaded SWNHs*

Preliminary experiments were performed to study the efficacy of loading cisplatin, a commonly used chemotherapeutic agent into oxidized SWNHs. A nano-precipitation method was used, similar to that described by Iijima, Yudasaka, and colleagues [87, 184, 185]. Yudasaka *et al.* found they were able to load cisplatin into SWNHs [184]; however, we had hoped to expand on this by evaluating the release properties depending on pH and temperature. Additionally, future work can be performed to optimize drug loading by increasing the temperature and length of time during stirring to optimize nucleation sites.

Briefly, SWNHs were acid oxidized using the method described in *Section 2.4.2.* Approximately 5.0 mg SWNHox was added to 2.5 mL of dimethylformamide (DMF) and bath sonicated for 60 min. Subsequently, 8.0 mg of cisplatin was dissolved in 2.5 mL DMF. Cisplatin (CDDP) was added to SWNHox in suspension and sonicated for 15 min;

followed by vigorous stirring for 24 h. SWNH+CDDP were dried under air flow and collected for analysis. Inductively-coupled plasma atomic emission spectroscopy (ICP-AES) was used to calculate loading efficiency based on the amount of platinum in a given sample. TEM was also utilized to observe crystal formation of CDDP after nanoprecipitation.

Preliminary findings showed a 91% loading efficiency of CDDP into SWNHs, calculated based on the total amount of platinum found with ICP-AES. TEM using an accelerating voltage of 100 kV (Zeiss 10CA TEM equipped with AMT Advantage GR/HR-B CCD camera system; Carl Zeiss AG; Oberkochen, Germany) showed black aggregates within SWNHs as observed in Figure 22. Further analysis is necessary to confirm that the CDDP precipitated in SWNH internal pore spaces.

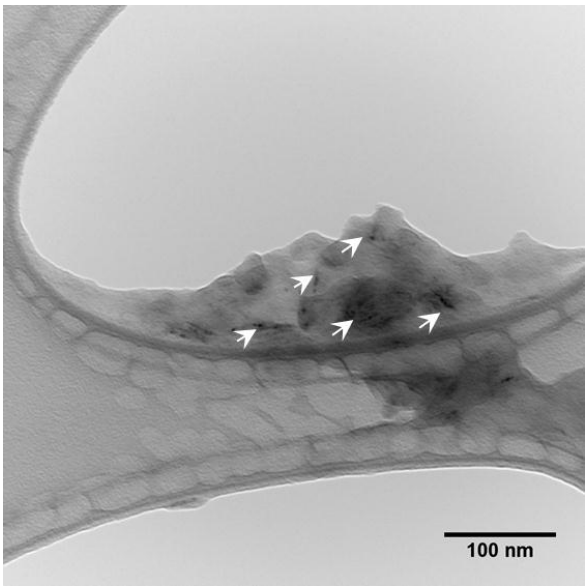


**Figure 22. TEM micrograph of cisplatin (CDDP)-loaded SWNHs. CDDP aggregates are denoted by white arrows.**

*4.3.3. Hyperthermia-Enhanced Nanoparticle Delivery*

Hyperthermia effectively augments current therapies, in addition to the delivery of nanoparticles [92-94]. This experiment evaluated the potential of using mild HT to increase cellular uptake of nanomaterials. SWNH-QDs prepared using the method described in *Section 2.9.3* were used to evaluate the effect of mild hyperthermia (HT) on the cellular uptake of SWNHs. MDA-MB-231 breast cancer cells were cultured in DMEM/F12 cell culture medium, supplemented with 10% fetal bovine serum and 1% pen-strep and maintained in a humidified atmosphere at 37°C, 5% $CO_2$. Cells were seeded in 6-well dishes at a density of 100,000 cells per well and incubated for 24 h. A concentration of 0.025 mg/mL SWNH-QDs were added to cells and dishes were either placed in an incubator at 37°C or in a circulating water bath at 43°C for a range of times. SWNH-QDs were removed and cells were rinsed four times with ice cold phosphate buffered saline solution. Cellular populations were then collected and evaluated with fluorescence-activated cell sorting (FACS).

Enhanced cellular uptake was observed at shorter times (~1-15 min) with hyperthermia; however, at longer exposure times, a decrease was observed compared to cellular uptake at physiologic conditions (Figure 23). This is speculated to be a result of protein denaturation in the cytoskeleton, potentially affecting cellular apoptosis. Additional experiments must be performed to optimize and characterize the effect of hyperthermia on cellular uptake of SWNHs-QDs, such as determining an adequate thermal exposure and exposure time to enhance this effect.

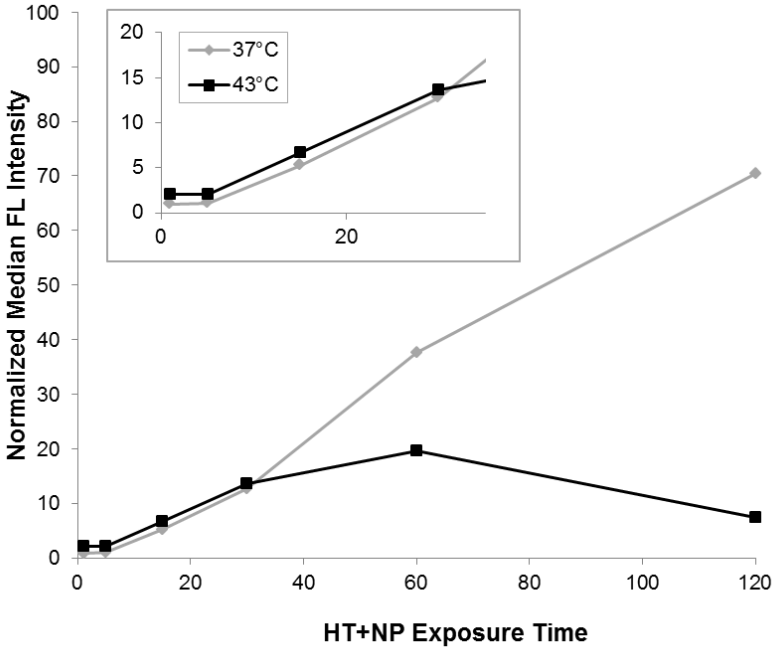


**Figure 23. The effects of hyperthermic conditions on SWNH-QD cellular uptake in MDA-MB-231 cells. The effect of HT+NP exposure time on median fluorescence intensity at lower exposure times is enlarged in the inset.**

*4.3.4. Quantum Dot Synthesis in the Presence of SWNHs**

*Work performed by Olga Ivanova[1] and Kristen Zimmermann[2]

[1]*Institute for Critical Technology and Applied Sciences, Virginia Tech, Blacksburg, VA*
[2]*School of Biomedical Engineering and Sciences, Virginia Tech, Blacksburg, VA*

There is always a concern of toxicity when cadmium-containing quantum dots (QDs) are used in biological application. Therefore, we proposed to synthesize QDs in the presence of air oxidized SWNHs (provided by Oak Ridge National Laboratory, Oak Ridge, TN) to encapsulate QDs. Thus, the inert carbon structure would protect them from oxidation in the external environment. SWNHs were oxidized by heating to a temperature of 500°C with a ramp rate of 30°C/min. SWNHs were held at this temperature for 25

min, followed by rapid cooling to room temperature. The average diameter of SWNHs was 40-60 nm, according to TEM. We hypothesized that the defect sizes initiated in the carbon surface would be large enough for $Cd^{2+}$ and $Se^{2+}$ ions to penetrate the SWNH internal pore space [186].

To synthesize QDs, previously published methods were used and modified to incorporate SWNHs [187]. Approximately, 6.0 mg SWNHs were sonicated in 0.53 mmol of selenium (Se) dissolved in 2.4 mL of tri-*n*-octylphosphine (TOP) for 15-30 min. Then, 0.4 mmol of cadmium oxide (CdO), 0.8 mmol of tetradecylphosphonic acid (TDPA), and 9.77 mmol of tri-*n*-octylphosphine oxide (TOPO) were added to a flask and heated to 270°C. The product was heated until the powders underwent phase change and the liquid became optically clear (approx. 30 min). Meanwhile, the Se/TOP/SWNH suspension was cooled to room temperature and once the CdO/TDPA/TOPO mixture became clear, the Se/TOP/SWNH suspension was injected. The temperature decreased to approximately 220°C upon injection and the temperature was then heated to a specific target for a desired time (Figure 24). Two samples of SWNH/QDs were removed, placed in toluene, and analyzed: (1) after heating to 230°C for 30 min and (2) subsequently raising the temperature to 270°C (~20 min) and holding at this temperature for 10 min. SWNH/QDs were characterized by TEM (Zeiss 10CA Carl Zeiss AG; Oberkochen, Germany) at an accelerating voltage of 100 kV.

SWNH+QDs were then imaged under visible light and ultraviolet light (365 nm wavelength). The first sample (vial on left) fluoresced pink, and after heating to 270°C, the sample fluoresced blue as shown in Figure 25.

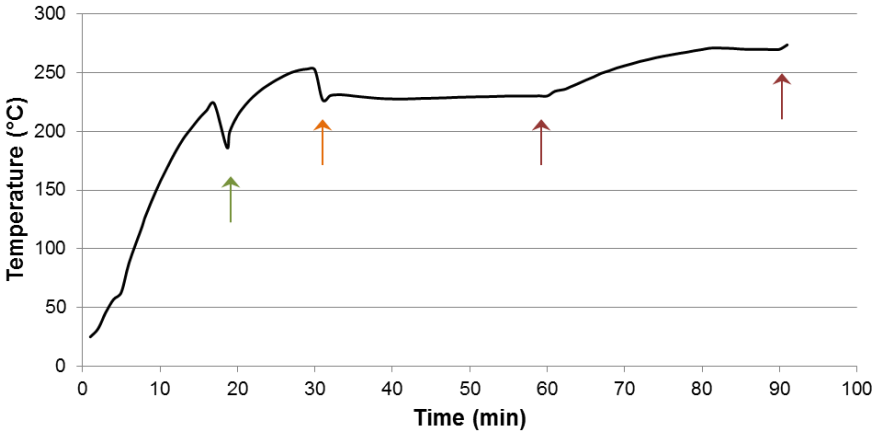


**Figure 24. Example temperature profile of QD synthesis in the presence of SWNHs. Green arrow points out a dip in the curve when the flask was removed from the heating mantle to rinse of the side walls, orange arrow represents Se/TOP/SWNH injection, and red arrows represent probe times.**

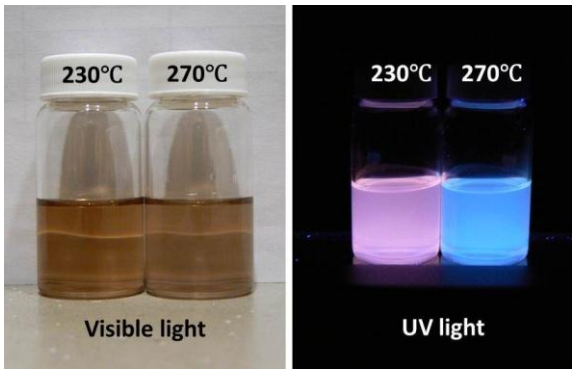


**Figure 25. Dilute solutions of SWNH+QD in toluene were imaged under visible (left image) and UV light (right image). Sample 1 (230°C/30 min) fluoresced pink, while sample 2 (270°C/10 min) fluoresced blue.**

TEM imaging of SWNH+QD samples provided interesting results. Larger spherical SWNHs were visible either bound to the surface or localized to internal pore spaces after reacting at 230°C for 30 min (Figure 26A). The resolution of the TEM used was not sufficient to image at higher magnifications to determine if smaller (1-3 nm) QDs were present inside of SWNH pores. Future investigation is necessary with high resolution TEM. An unexpected and fascinating finding, however, was the synthesis of

various QD shapes using this technique (squares/rectangles, triangles, and hexagons). Raising the reaction temperature to 270°C produced less spherical QDs and more shapes (Figure 26C). The SWNHs were separated from QDs via centrifugation; however, the square QDs precipitated with SWNHs due to their sizes.

Additional work should be performed to explore both avenues of this project: (1) if QDs were successfully synthesized inside of SWNHs and if they fluoresce, and (2) why SWNHs caused various QD morphologies that are typically not observed without altering ligand types and ratios (TOP, TOPO, etc.). These unique QDs may have potential implications in electronics because the square-shaped QDs self-assemble and align.

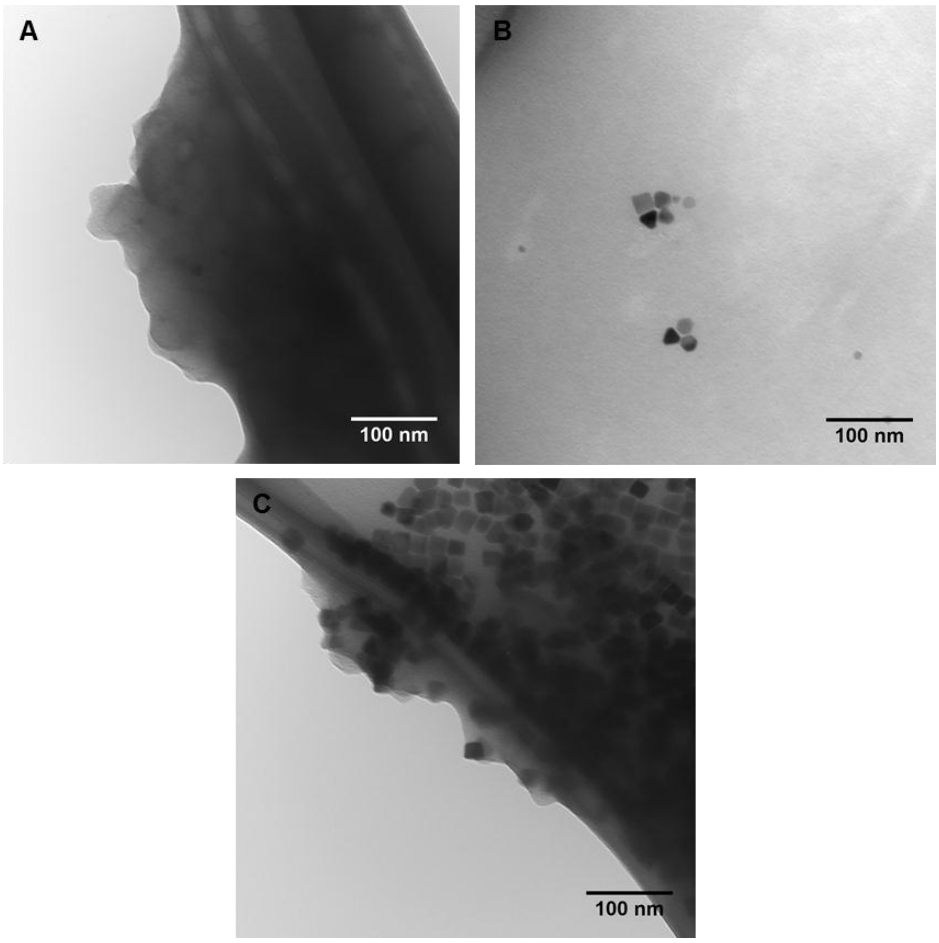


**Figure 26. TEM micrographs of SWNH+QD samples. (A,B) SWNH+QD sample 1 (230°C/30 min). (C) SWNH+QD sample 2 (270°C/10 min).**

## 5. REFERENCES


1. Kochanek K, Xu J, Murphy S, Minino A, Kumng H. Deaths: Preliminary Data for 2009. In: CDC/NCHS, editor. National Vital Statistics Reports2011.
2. Murphy S, Xu J, Kochanek K. Deaths: Preliminary Data for 2010. In: CDC/NCHS, editor. National Vital Statistics Reports2012.
3. Cancer Facts and Figures 2012. Atlanta: American Cancer Society 2012.
4. Shapiro S, Venet W, Strax P, Venet L, Roeser R. 10-Year to 14-Year Effect of Screening on Breast-Cancer Mortality. J Natl Cancer I. 1982;69:349-355.
5. Kerlikowske K, Grady D, Rubin SM, Sandrock C, Ernster VL. Efficacy of Screening Mammography - a Metaanalysis. Jama-J Am Med Assoc. 1995;273:149-154.
6. Siegel R, Naishadham D, Jemal A. Cancer Statistics, 2012. Ca-Cancer J Clin. 2012;62:10-29.
7. Nakasu S, Hirano A, Llena JF, Shimura T, Handa J. Interface between the Meningioma and the Brain. Surg Neurol. 1989;32:206-212.
8. Sidransky D, Frost P, Voneschenbach A, Oyasu R, Preisinger AC, Vogelstein B. Clonal Origin of Bladder-Cancer. New Engl J Med. 1992;326:737-740.
9. NCI Funded Research Portfolio [database on the Internet]. National Institute of Health 2011 [cited 2012 April 02]. Available from: http://fundedresearch.cancer.gov/.
10. Peer D, Karp JM, Hong S, FaroKHzad OC, Margalit R, Langer R. Nanocarriers as an emerging platform for cancer therapy. Nat Nanotechnol. 2007;2:751-760.
11. Castro MG, Cowen R, Williamson IK, David A, Jimenez-Dalmaroni MJ, Yuan X, Bigliari A, Williams JC, Hu J, Lowenstein PR. Current and future strategies for the treatment of malignant brain tumors. Pharmacol Therapeut. 2003;98:71-108.
12. Sakamoto JH, van de Ven AL, Godin B, Blanco E, Serda RE, Grattoni A, Ziemys A, Bouamrani A, Hu T, Ranganathan SI, De Rosa E, Martinez JO, Smid CA, Buchanan RM, Lee SY, Srinivasan S, Landry M, Meyn A, Tasciotti E, Liu XW, Decuzzi P, Ferrari M. Enabling individualized therapy through nanotechnology. Pharmacol Res. 2010;62:57-89.
13. Ferrari M. Cancer nanotechnology: Opportunities and challenges. Nat Rev Cancer. 2005;5:161-171.
14. Davis ME, Chen Z, Shin DM. Nanoparticle therapeutics: an emerging treatment modality for cancer. Nat Rev Drug Discov. 2008;7:771-782.
15. Burke A, Ding X, Singh R, Kraft RA, Levi-Polyachenko N, Rylander MN, Szot C, Buchanan C, Whitney J, Fisher J, Hatcher HC, D'Agostino R, Jr., Kock ND, Ajayan PM, Carroll DL, Akman S, Torti FM, Torti SV. Long-term survival following a single treatment of kidney tumors with multiwalled carbon nanotubes and near-infrared radiation. Proc Natl Acad Sci U S A. 2009;106:12897-12902.
16. Fisher JW, Sarkar S, Buchanan CF, Szot CS, Whitney J, Hatcher HC, Torti SV, Rylander CG, Rylander MN. Photothermal response of human and murine cancer cells to multiwalled carbon nanotubes after laser irradiation. Cancer Res. 2010;70:9855-9864.

17. Gobin AM, Lee MH, Halas NJ, James WD, Drezek RA, West JL. Near-infrared resonant nanoshells for combined optical imaging and photothermal cancer therapy. Nano Lett. 2007;7:1929-1934.
18. Johannsen M, Thiesen B, Wust P, Jordan A. Magnetic nanoparticle hyperthermia for prostate cancer. Int J Hyperther. 2010;26:790-795.
19. Wust P, Gneveckow U, Johannsen M, Bohmer D, Henkel T, Kahmann F, Sehouli J, Felix R, Ricke J, Jordan A. Magnetic nanoparticles for interstitial thermotherapy - feasibility, tolerance and achieved temperatures. Int J Hyperther. 2006;22:673-685.
20. Cho SH, Jones BL, Krishnan S. The dosimetric feasibility of gold nanoparticle-aided radiation therapy (GNRT) via brachytherapy using low-energy gamma-/x-ray sources. Phys Med Biol. 2009;54:4889-4905.
21. Roa W, Zhang XJ, Guo LH, Shaw A, Hu XY, Xiong YP, Gulavita S, Patel S, Sun XJ, Chen J, Moore R, Xing JZ. Gold nanoparticle sensitize radiotherapy of prostate cancer cells by regulation of the cell cycle. Nanotechnology. 2009;20.
22. Zhang M, Murakami T, Ajima K, Tsuchida K, Sandanayaka ASD, Ito O, Iijima S, Yudasaka M. Fabrication of ZnPc/protein nanohorns for double photodynamic and hyperthermic cancer phototherapy. P Natl Acad Sci USA. 2008;105:14773-14778.
23. Wieder ME, Hone DC, Cook MJ, Handsley MM, Gavrilovic J, Russell DA. Intracellular photodynamic therapy with photosensitizer-nanoparticle conjugates: cancer therapy using a 'Trojan horse'. Photoch Photobio Sci. 2006;5:727-734.
24. Cheng Y, Samia AC, Meyers JD, Panagopoulos I, Fei BW, Burda C. Highly efficient drug delivery with gold nanoparticle vectors for in vivo photodynamic therapy of cancer. J Am Chem Soc. 2008;130:10643-10647.
25. Samia ACS, Chen XB, Burda C. Semiconductor quantum dots for photodynamic therapy. J Am Chem Soc. 2003;125:15736-15737.
26. Dhar S, Liu Z, Thomale J, Dai HJ, Lippard SJ. Targeted single-wall carbon nanotube-mediated Pt(IV) prodrug delivery using folate as a homing device. J Am Chem Soc. 2008;130:11467-11476.
27. Guo Y, Shi DL, Cho HS, Dong ZY, Kulkarni A, Pauletti GM, Wang W, Lian J, Liu W, Ren L, Zhang QQ, Liu GK, Huth C, Wang LM, Ewing RC. In vivo imaging and drug storage by quantum-dot-conjugated carbon nanotubes. Adv Funct Mater. 2008;18:2489-2497.
28. Kopelman R, Koo YEL, Philbert M, Moffat BA, Reddy GR, McConville P, Hall DE, Chenevert TL, Bhojani MS, Buck SM, Rehemtulla A, Ross BD. Multifunctional nanoparticle platforms for in vivo MRI enhancement and photodynamic therapy of a rat brain cancer. J Magn Magn Mater. 2005;293:404-410.
29. Chithrani BD, Ghazani AA, Chan WCW. Determining the size and shape dependence of gold nanoparticle uptake into mammalian cells. Nano Lett. 2006;6:662-668.
30. Decuzzi P, Godin B, Tanaka T, Lee SY, Chiappini C, Liu X, Ferrari M. Size and shape effects in the biodistribution of intravascularly injected particles. J Control Release. 2010;141:320-327.
31. Jain RK, Stylianopoulos T. Delivering nanomedicine to solid tumors. Nat Rev Clin Oncol. 2010;7:653-664.

32. Brannon-Peppas L, Blanchette JO. Nanoparticle and targeted systems for cancer therapy. Adv Drug Deliver Rev. 2004;56:1649-1659.
33. Acharya S, Sahoo SK. PLGA nanoparticles containing various anticancer agents and tumour delivery by EPR effect. Adv Drug Deliver Rev. 2011;63:170-183.
34. Sahoo SK, Parveen S, Panda JJ. The present and future of nanotechnology in human health care. Nanomed-Nanotechnol. 2007;3:20-31.
35. Pasquier AD, Unalan HE, Kanwal A, Miller S, Chhowalla M. Conducting and transparent single-wall carbon nanotube electrodes for polymer-fullerene solar cells. Appl Phys Lett. 2005;87.
36. Brigger I, Dubernet C, Couvreur P. Nanoparticles in cancer therapy and diagnosis. Adv Drug Deliver Rev. 2002;54:631-651.
37. Hobbs SK, Monsky WL, Yuan F, Roberts WG, Griffith L, Torchilin VP, Jain RK. Regulation of transport pathways in tumor vessels: role of tumor type and microenvironment. Proc Natl Acad Sci U S A. 1998;95:4607-4612.
38. Koukourakis MI, Giatromanolaki A, Sivridis E, Fezoulidis I. Cancer vascularization: Implications in radiotherapy? Int J Radiat Oncol. 2000;48:545-553.
39. Li Y, Wang J, Wientjes MG, Au JL. Delivery of nanomedicines to extracellular and intracellular compartments of a solid tumor. Adv Drug Deliv Rev. 2012;64:29-39.
40. Boucher Y, Jain RK. Microvascular Pressure Is the Principal Driving Force for Interstitial Hypertension in Solid Tumors - Implications for Vascular Collapse. Cancer Res. 1992;52:5110-5114.
41. Bianchi E, Cohen RL, Thor AT, Todd RF, Mizukami IF, Lawrence DA, Ljung BM, Shuman MA, Smith HS. The Urokinase Receptor Is Expressed in Invasive Breast-Cancer but Not in Normal Breast-Tissue. Cancer Res. 1994;54:861-866.
42. Kaushal V, Kohli M, Dennis RA, Siegel ER, Chiles WW, Mukunyadzi P. Thrombin receptor expression is upregulated in prostate cancer. Prostate. 2006;66:273-282.
43. Balkwill F. The significance of cancer cell expression of the chemokine receptor CXCR4. Semin Cancer Biol. 2004;14:171-179.
44. Sudimack J, Lee RJ. Targeted drug delivery via the folate receptor. Adv Drug Deliver Rev. 2000;41:147-162.
45. Ross JF, Chaudhuri PK, Ratnam M. Differential Regulation of Folate Receptor Isoforms in Normal and Malignant-Tissues in-Vivo and in Established Cell-Lines - Physiological and Clinical Implications. Cancer. 1994;73:2432-2443.
46. Elnakat H, Ratnam M. Distribution, functionality and gene regulation of folate receptor isoforms: implications in targeted therapy. Adv Drug Deliv Rev. 2004;56:1067-1084.
47. Alexis F, Pridgen E, Molnar LK, Farokhzad OC. Factors affecting the clearance and biodistribution of polymeric nanoparticles. Mol Pharmaceut. 2008;5:505-515.
48. Blanco E, Hsiao A, Mann AP, Landry MG, Meric-Bernstam F, Ferrari M. Nanomedicine in cancer therapy: innovative trends and prospects. Cancer science. 2011;102:1247-1252.
49. Li SD, Huang L. Nanoparticles evading the reticuloendothelial system: role of the supported bilayer. Biochimica et biophysica acta. 2009;1788:2259-2266.
50. Klibanov AL, Maruyama K, Beckerleg AM, Torchilin VP, Huang L. Activity of amphipathic poly(ethylene glycol) 5000 to prolong the circulation time of

liposomes depends on the liposome size and is unfavorable for immunoliposome binding to target. Biochimica et biophysica acta. 1991;1062:142-148.
51. Nomura T, Koreeda N, Yamashita F, Takakura Y, Hashida M. Effect of particle size and charge on the disposition of lipid carriers after intratumoral injection into tissue-isolated tumors. Pharmaceut Res. 1998;15:128-132.
52. Hood RL, Rodgers AK, Carswell WF, Kosoglu MA, Rylander MN, Grant D, Robertson JL, Rylander CG. Microneedle Delivery of Single-Walled Carbon Nanohorns to Enhance Photothermal Heating in Bladder Tissue Lasers in Medicial Science. 2012;Submitted for Review.
53. Kosoglu MA, Hood RL, Chen Y, Xu Y, Rylander MN, Rylander CG. Fiber Optic Microneedles for Transdermal Light Delivery: Ex Vivo Porcine Skin Penetration Experiments. J Biomech Eng-T Asme. 2010;132.
54. Chithrani BD, Chan WCW. Elucidating the mechanism of cellular uptake and removal of protein-coated gold nanoparticles of different sizes and shapes. Nano Lett. 2007;7:1542-1550.
55. Arnida, Malugin A, Ghandehari H. Cellular uptake and toxicity of gold nanoparticles in prostate cancer cells: a comparative study of rods and spheres. J Appl Toxicol. 2010;30:212-217.
56. Huang XL, Teng X, Chen D, Tang FQ, He JQ. The effect of the shape of mesoporous silica nanoparticles on cellular uptake and cell function. Biomaterials. 2010;31:438-448.
57. Gratton SEA, Ropp PA, Pohlhaus PD, Luft JC, Madden VJ, Napier ME, DeSimone JM. The effect of particle design on cellular internalization pathways. P Natl Acad Sci USA. 2008;105:11613-11618.
58. He CB, Hu YP, Yin LC, Tang C, Yin CH. Effects of particle size and surface charge on cellular uptake and biodistribution of polymeric nanoparticles. Biomaterials. 2010;31:3657-3666.
59. Zhao F, Zhao Y, Liu Y, Chang X, Chen C. Cellular uptake, intracellular trafficking, and cytotoxicity of nanomaterials. Small. 2011;7:1322-1337.
60. Jiang W, Kim BYS, Rutka JT, Chan WCW. Nanoparticle-mediated cellular response is size-dependent. Nat Nanotechnol. 2008;3:145-150.
61. Ganley IG, Carroll K, Bittova L, Pfeffer S. Rab9 GTPase regulates late endosome size and requires effector interaction for its stability. Molecular biology of the cell. 2004;15:5420-5430.
62. Robert D, Nguyen TH, Gallet F, Wilhelm C. In Vivo Determination of Fluctuating Forces during Endosome Trafficking Using a Combination of Active and Passive Microrheology. Plos One. 2010;5.
63. Decuzzi P, Pasqualini R, Arap W, Ferrari M. Intravascular delivery of particulate systems: does geometry really matter? Pharm Res. 2009;26:235-243.
64. Lee SY, Ferrari M, Decuzzi P. Shaping nano-/micro-particles for enhanced vascular interaction in laminar flows. Nanotechnology. 2009;20.
65. Li SD, Huang L. Pharmacokinetics and biodistribution of nanoparticles. Mol Pharm. 2008;5:496-504.
66. Arnida, Janat-Amsbury MM, Ray A, Peterson CM, Ghandehari H. Geometry and surface characteristics of gold nanoparticles influence their biodistribution and uptake by macrophages. Eur J Pharm Biopharm. 2011;77:417-423.

67. Sun YN, Wang CD, Zhang XM, Ren L, Tian XH. Shape Dependence of Gold Nanoparticles on In Vivo Acute Toxicological Effects and Biodistribution. J Nanosci Nanotechno. 2011;11:1210-1216.
68. Labhasetwar V. Nanotechnology for drug and gene therapy: the importance of understanding molecular mechanisms of delivery. Current opinion in biotechnology. 2005;16:674-680.
69. Pan L, He Q, Liu J, Chen Y, Ma M, Zhang L, Shi J. Nuclear-Targeted Drug Delivery of TAT Peptide-Conjugated Monodisperse Mesoporous Silica Nanoparticles. J Am Chem Soc. 2012;134:5722-5725.
70. dos Santos T, Varela J, Lynch I, Salvati A, Dawson KA. Quantitative Assessment of the Comparative Nanoparticle-Uptake Efficiency of a Range of Cell Lines. Small. 2011;7:3341-3349.
71. Iijima S. Direct Observation of the Tetrahedral Bonding in Graphitized Carbon-Black by High-Resolution Electron-Microscopy. J Cryst Growth. 1980;50:675-683.
72. Kroto HW, Heath JR, Obrien SC, Curl RF, Smalley RE. C-60 - Buckminsterfullerene. Nature. 1985;318:162-163.
73. Iijima S. Helical Microtubules of Graphitic Carbon. Nature. 1991;354:56-58.
74. Iijima S, Yudasaka M, Yamada R, Bandow S, Suenaga K, Kokai F, Takahashi K. Nano-aggregates of single-walled graphitic carbon nano-horns. Chem Phys Lett. 1999;309:165-170.
75. Bianco A, Kostarelos K, Prato M. Opportunities and challenges of carbon-based nanomaterials for cancer therapy. Expert Opin Drug Del. 2008;5:331-342.
76. Yudasaka M, Iijima S, Crespi VH. Single-wall carbon nanohorns and nanocones. Top Appl Phys. 2008;111:605-629.
77. Suehiro J, Zhou GB, Hara M. Fabrication of a carbon nanotube-based gas sensor using dielectrophoresis and its application for ammonia detection by impedance spectroscopy. J Phys D Appl Phys. 2003;36:L109-L114.
78. Dorozhkin PS, Tovstonog SV, Golberg D, Zhan JH, Ishikawa Y, Shiozawa M, Nakanishi H, Nakata K, Bando Y. A liquid-Ga-filled carbon nanotube: A miniaturized temperature sensor and electrical switch. Small. 2005;1:1088-1093.
79. Dillon AC, Jones KM, Bekkedahl TA, Kiang CH, Bethune DS, Heben MJ. Storage of hydrogen in single-walled carbon nanotubes. Nature. 1997;386:377-379.
80. Xu WC, Takahashi K, Matsuo Y, Hattori Y, Kumagai M, Ishiyama S, Kaneko K, Iijima S. Investigation of hydrogen storage capacity of various carbon materials. Int J Hydrogen Energ. 2007;32:2504-2512.
81. Murata K, Kaneko K, Kanoh H, Kasuya D, Takahashi K, Kokai F, Yudasaka M, Iijima S. Adsorption mechanism of supercritical hydrogen in internal and interstitial nanospaces of single-wall carbon nanohorn assembly. J Phys Chem B. 2002;106:11132-11138.
82. Wei JQ, Jia Y, Shu QK, Gu ZY, Wang KL, Zhuang DM, Zhang G, Wang ZC, Luo JB, Cao AY, Wu DH. Double-walled carbon nanotube solar cells. Nano Lett. 2007;7:2317-2321.
83. Liu X, Shi L, Niu W, Li H, Xu G. Amperometric glucose biosensor based on single-walled carbon nanohorns. Biosens Bioelectron. 2008;23:1887-1890.

84. Wang J, Liu GD, Jan MR. Ultrasensitive electrical biosensing of proteins and DNA: Carbon-nanotube derived amplification of the recognition and transduction events. J Am Chem Soc. 2004;126:3010-3011.
85. Bhirde AA, Patel V, Gavard J, Zhang GF, Sousa AA, Masedunskas A, Leapman RD, Weigert R, Gutkind JS, Rusling JF. Targeted Killing of Cancer Cells in Vivo and in Vitro with EGF-Directed Carbon Nanotube-Based Drug Delivery. Acs Nano. 2009;3:307-316.
86. Muralkami T, Ajima K, Miyawaki J, Yudasaka M, Iijima S, Shiba K. Drug-loaded carbon nanohorns: Adsorption and release of dexamethasone in vitro. Mol Pharmaceut. 2004;1:399-405.
87. Ajima K, Yudasaka M, Murakami T, Maigne A, Shiba K, Ijima S. Carbon nanohorns as anticancer drug carriers. Mol Pharmaceut. 2005;2:475-480.
88. Whitney JR, Sarkar S, Zhang JF, Thao D, Young T, Manson MK, Campbell TA, Puretzky AA, Rouleau CM, More KL, Geohegan DB, Rylander CG, Dorn HC, Rylander MN. Single Walled Carbon Nanohorns as Photothermal Cancer Agents. Laser Surg Med. 2011;43:43-51.
89. Zhou FF, Xing D, Ou ZM, Wu BY, Resasco DE, Chen WR. Cancer photothermal therapy in the near-infrared region by using single-walled carbon nanotubes. J Biomed Opt. 2009;14.
90. Moon HK, Lee SH, Choi HC. In Vivo Near-Infrared Mediated Tumor Destruction by Photothermal Effect of Carbon Nanotubes. Acs Nano. 2009;3:3707-3713.
91. Sharma SK, Chiang LY, Hamblin MR. Photodynamic therapy with fullerenes in vivo: reality or a dream? Nanomedicine. 2011;6:1813-1825.
92. van der Zee J. Heating the patient: a promising approach? Ann Oncol. 2002;13:1173-1184.
93. Issels RD. Hyperthermia adds to chemotherapy. Eur J Cancer. 2008;44:2546-2554.
94. Kong G, Braun RD, Dewhirst MW. Hyperthermia enables tumor-specific nanoparticle delivery: Effect of particle size. Cancer Res. 2000;60:4440-4445.
95. Kong G, Braun RD, Dewhirst MW. Characterization of the effect of hyperthermia on nanoparticle extravasation from tumor vasculature. Cancer Res. 2001;61:3027-3032.
96. Ponce AM, Vujaskovic Z, Yuan F, Needham D, Dewhirst MW. Hyperthermia mediated liposomal drug delivery. Int J Hyperther. 2006;22:205-213.
97. Hildebrandt B, Wust P, Ahlers O, Dieing A, Sreenivasa G, Kerner T, Felix R, Riess H. The cellular and molecular basis of hyperthermia. Crit Rev Oncol Hemat. 2002;43:33-56.
98. Kawai H, Minamiya Y, Kitamura M, Matsuzaki I, Hashimoto M, Suzuki H, Abo S. Direct measurement of doxorubicin concentration in the intact, living single cancer cell during hyperthermia. Cancer. 1997;79:214-219.
99. Gabano E, Colangelo D, Ghezzi AR, Osella D. The influence of temperature on antiproliferative effects, cellular uptake and DNA platination of the clinically employed Pt(II)-drugs. Journal of inorganic biochemistry. 2008;102:629-635.
100. van der Heijden AG, Verhaegh G, Jansen CFJ, Schalken JA, Witjes JA. Effect of hyperthermia on the cytotoxicity of 4 chemotherapeutic agents currently used for the treatment of transitional cell carcinoma of the bladder: An in vitro study. J Urology. 2005;173:1375-1380.

101. Gerke P, Filejski W, Robins HI, Wiedemann GJ, Steinhoff J. Nephrotoxicity of ifosfamide, carboplatin and etoposide (ICE) alone or combined with extracorporeal or radiant-heat-induced whole-body hyperthermia. J Cancer Res Clin. 2000;126:173-177.
102. Huang X, El-Sayed IH, Qian W, El-Sayed MA. Cancer cell imaging and photothermal therapy in the near-infrared region by using gold nanorods. J Am Chem Soc. 2006;128:2115-2120.
103. Hauck TS, Jennings TL, Yatsenko T, Kumaradas JC, Chan WCW. Enhancing the Toxicity of Cancer Chemotherapeutics with Gold Nanorod Hyperthermia. Adv Mater. 2008;20:3832-+.
104. Zhang W, Guo ZY, Huang DQ, Liu ZM, Guo X, Zhong HQ. Synergistic effect of chemo-photothermal therapy using PEGylated graphene oxide. Biomaterials. 2011;32:8555-8561.
105. Lee SM, Lee YH. Hydrogen storage in single-walled carbon nanotubes. Appl Phys Lett. 2000;76:2877-2879.
106. Schlapbach L, Zuttel A. Hydrogen-storage materials for mobile applications. Nature. 2001;414:353-358.
107. Endo M, Strano MS, Ajayan PM. Potential applications of carbon nanotubes. In: Jorio A, Dresselhaus G, Dresselhaus M, editors. Topics in Applied Physics: Carbon Nanotubes Springer-Verlag Berlin Heidelberg; 2008. p. 13-62.
108. Cremillieux Y, Al Faraj A, Cieslar K, Lacroix G, Gaillard S, Canot-Soulas E. In Vivo Imaging of Carbon Nanotube Biodistribution Using Magnetic Resonance Imaging. Nano Lett. 2009;9:1023-1027.
109. Xu JX, Yudasaka M, Kouraba S, Sekido M, Yamamoto Y, Iijima S. Single wall carbon nanohorn as a drug carrier for controlled release. Chem Phys Lett. 2008;461:189-192.
110. Dorn HC, Zhang JF, Ge JC, Shultz MD, Chung EN, Singh G, Shu CY, Fatouros PP, Henderson SC, Corwin FD, Geohegan DB, Puretzky AA, Rouleau CM, More K, Rylander C, Rylander MN, Gibson HW. In Vitro and in Vivo Studies of Single-Walled Carbon Nanohorns with Encapsulated Metallofullerenes and Exohedrally Functionalized Quantum Dots. Nano Lett. 2010;10:2843-2848.
111. Miyawaki J, Yudasaka M, Imai H, Yorimitsu H, Isobe H, Nakamura E, Iijima S. In vivo magnetic resonance imaging of single-walled carbon nanohorns by labeling with magnetite nanoparticles. Adv Mater. 2006;18:1010-+.
112. Al Faraj A, Cieslar K, Lacroix G, Gaillard S, Canot-Soulas E, Cremillieux Y. In Vivo Imaging of Carbon Nanotube Biodistribution Using Magnetic Resonance Imaging. Nano Lett. 2009;9:1023-1027.
113. Richard C, Doan BT, Beloeil JC, Bessodes M, Toth E, Scherman D. Noncovalent functionalization of carbon nanotubes with amphiphilic Gd3+ chelates: Toward powerful T-1 and T-2 MRI contrast agents. Nano Lett. 2008;8:232-236.
114. Yudasaka M, Iijima S, Yamada R, Bandow S, Suenaga K, Kokai F, Takahashi K. Nano-aggregates of single-walled graphitic carbon nano-horns. Chem Phys Lett. 1999;309:165-170.
115. Utsumi S, Miyawaki J, Tanaka H, Hattori Y, Itoi T, Ichikuni N, Kanoh H, Yudasaka M, Iijima S, Kaneko K. Opening mechanism of internal nanoporosity of single-wall carbon nanohorn. J Phys Chem B. 2005;109:14319-14324.

116. Teeguarden JG, Hinderliter PM, Orr G, Thrall BD, Pounds JG. Particokinetics in vitro: Dosimetry considerations for in vitro nanoparticle toxicity assessments. Toxicol Sci. 2007;95:300-312.
117. Miyawaki J, Matsumura S, Yuge R, Murakami T, Sato S, Tonnida A, Tsuruo T, Ichihashi T, Fujinami T, Irie H, Tsuchida K, Iijima S, Shiba K, Yudasaka M. Biodistribution and Ultrastructural Localization of Single-Walled Carbon Nanohorns Determined In Vivo with Embedded Gd(2)O(3) Labels. Acs Nano. 2009;3:1399-1406.
118. Porter AE, Gass M, Muller K, Skepper JN, Midgley PA, Welland M. Direct imaging of single-walled carbon nanotubes in cells. Nat Nanotechnol. 2007;2:713-717.
119. Susumu K, Medintz IL, Mattoussi H. Colloidal Quantum Dots: Synthesis, Photophysical Properties, and Biofunctionalization Strategies In: Mattoussi H, Cheon J, editors. Inorganic Nanoprobes for Biological Sensing and Imaging. Norwood: Artech House, Inc.; 2009. p. 1-26.
120. Resch-Genger U, Grabolle M, Cavaliere-Jaricot S, Nitschke R, Nann T. Quantum dots versus organic dyes as fluorescent labels. Nat Methods. 2008;5:763-775.
121. Derfus AM, Chan WCW, Bhatia SN. Probing the cytotoxicity of semiconductor quantum dots. Nano Lett. 2004;4:11-18.
122. Hoshino A, Fujioka K, Oku T, Suga M, Sasaki YF, Ohta T, Yasuhara M, Suzuki K, Yamamoto K. Physicochemical properties and cellular toxicity of nanocrystal quantum dots depend on their surface modification. Nano Lett. 2004;4:2163-2169.
123. Geys J, Nemmar A, Verbeken E, Smolders E, Ratoi M, Hoylaerts MF, Nemery B, Hoet PHM. Acute Toxicity and Prothrombotic Effects of Quantum Dots: Impact of Surface Charge. Environ Health Persp. 2008;116:1607-1613.
124. Gao XH, Cui YY, Levenson RM, Chung LWK, Nie SM. In vivo cancer targeting and imaging with semiconductor quantum dots. Nat Biotechnol. 2004;22:969-976.
125. Li L, Daou TJ, Texier I, Tran TKC, Nguyen QL, Reiss P. Highly Luminescent CuInS(2)/ZnS Core/Shell Nanocrystals: Cadmium-Free Quantum Dots for In Vivo Imaging. Chem Mater. 2009;21:2422-2429.
126. Yong KT, Ding H, Roy I, Law WC, Bergey EJ, Maitra A, Prasad PN. Imaging Pancreatic Cancer Using Bioconjugated InP Quantum Dots. Acs Nano. 2009;3:502-510.
127. Zimmer JP, Kim SW, Ohnishi S, Tanaka E, Frangioni JV, Bawendi MG. Size series of small indium arsenide-zinc selenide core-shell nanocrystals and their application to in vivo imaging. J Am Chem Soc. 2006;128:2526-2527.
128. Raffaelle RP, Landi BJ, Evans CM, Worman JJ, Castro SL, Bailey SG. Noncovalent attachment of CdSe quantum dots to single wall carbon nanotubes. Mater Lett. 2006;60:3502-3506.
129. Haremza JM, Hahn MA, Krauss TD. Attachment of single CdSe nanocrystals to individual single-walled carbon nanotubes. Nano Lett. 2002;2:1253-1258.
130. Ozkan CS, Ravindran S, Chaudhary S, Colburn B, Ozkan M. Covalent coupling of quantum dots to multiwalled carbon nanotubes for electronic device applications. Nano Lett. 2003;3:447-453.
131. Wong SS, Banerjee S. Synthesis and characterization of carbon nanotube-nanocrystal heterostructures. Nano Lett. 2002;2:195-200.

132. Feng GD, Fei Q, Xiao DH, Zhang ZQ, Huan YF. A novel silica-coated multiwall carbon nanotube with CdTe quantum dots nanocomposite. Spectrochim Acta A. 2009;74:597-601.
133. Wang L, Niu MG, Wu ZW. In situ growth of CdSe/CdS quantum dots inside and outside of MWCNTs. Curr Appl Phys. 2009;9:1112-1116.
134. Bottini M, Cerignoli F, Dawson MI, Magrini A, Rosato N, Mustelin T. Full-length single-walled carbon nanotubes decorated with streptavidin-conjugated quantum dots as multivalent intracellular fluorescent nanoprobes. Biomacromolecules. 2006;7:2259-2263.
135. Medintz IL, Uyeda HT, Goldman ER, Mattoussi H. Quantum dot bioconjugates for imaging, labelling and sensing. Nat Mater. 2005;4:435-446.
136. Li XL, Qin YJ, Picraux ST, Guo ZX. Noncovalent assembly of carbon nanotube-inorganic hybrids. J Mater Chem. 2011;21:7527-7547.
137. Puretzky AA, Styers-Barnett DJ, Rouleau CM, Hu H, Zhao B, Ivanov IN, Geohegan DB. Cumulative and continuous laser vaporization synthesis of single wall carbon nanotubes and nanohorns. Appl Phys a-Mater. 2008;93:849-855.
138. Chen J, Rao AM, Lyuksyutov S, Itkis ME, Hamon MA, Hu H, Cohn RW, Eklund PC, Colbert DT, Smalley RE, Haddon RC. Dissolution of full-length single-walled carbon nanotubes. J Phys Chem B. 2001;105:2525-2528.
139. Tchoul MN, Ford WT, Lolli G, Resasco DE, Arepalli S. Effect of mild nitric acid oxidation on dispersability, size, and structure of single-walled carbon nanotubes. Chem Mater. 2007;19:5765-5772.
140. Zhu S, Han S, Zhang L, Parveen S, Xu G. A novel fluorescent aptasensor based on single-walled carbon nanohorns. Nanoscale. 2011;3:4589-4592.
141. Raja PMV, Connolley J, Ganesan GP, Ci LJ, Ajayan PM, Nalamasu O, Thompson DM. Impact of carbon nanotube exposure, dosage and aggregation on smooth muscle cells. Toxicol Lett. 2007;169:51-63.
142. Shi DL, Guo Y, Dong ZY, Lian J, Wang W, Liu G, Wang LM, Ewing RC. Quantum-dot-activated luminescent carbon nanotubes via a nano scale surface functionalization for in vivo imaging (vol 19, pg 4033, 2007). Adv Mater. 2008;20:1405-1405.
143. Parak WJ, Gerion D, Pellegrino T, Zanchet D, Micheel C, Williams SC, Boudreau R, Le Gros MA, Larabell CA, Alivisatos AP. Biological applications of colloidal nanocrystals. Nanotechnology. 2003;14:R15-R27.
144. Wuister SF, Swart I, van Driel F, Hickey SG, Donega CD. Highly luminescent water-soluble CdTe quantum dots. Nano Lett. 2003;3:503-507.
145. Woelfle C, Claus RO. Transparent and flexible quantum dot-polymer composites using an ionic liquid as compatible polymerization medium. Nanotechnology. 2007;18.
146. Maruyama K. Intracellular targeting delivery of liposomal drugs to solid tumors based on EPR effects. Adv Drug Deliv Rev. 2011;63:161-169.
147. Yuan F, Dellian M, Fukumura D, Leunig M, Berk DA, Torchilin VP, Jain RK. Vascular-Permeability in a Human Tumor Xenograft - Molecular-Size Dependence and Cutoff Size. Cancer Res. 1995;55:3752-3756.

148. White B, Banerjee S, O'Brien S, Turro NJ, Herman IP. Zeta-potential measurements of surfactant-wrapped individual single-walled carbon nanotubes. J Phys Chem C. 2007;111:13684-13690.
149. Grabinski C, Hussain S, Lafdi K, Braydich-Stolle L, Schlager J. Effect of particle dimension on biocompatibility of carbon nanomaterials. Carbon. 2007;45:2828-2835.
150. Monteiro-Riviere NA, Inman AO, Zhang LW. Limitations and relative utility of screening assays to assess engineered nanoparticle toxicity in a human cell line. Toxicol Appl Pharm. 2009;234:222-235.
151. Kam NWS, Liu ZA, Dai HJ. Carbon nanotubes as intracellular transporters for proteins and DNA: An investigation of the uptake mechanism and pathway. Angew Chem Int Edit. 2006;45:577-581.
152. Kostarelos K, Lacerda L, Pastorin G, Wu W, Wieckowski S, Luangsivilay J, Godefroy S, Pantarotto D, Briand JP, Muller S, Prato M, Bianco A. Cellular uptake of functionalized carbon nanotubes is independent of functional group and cell type. Nat Nanotechnol. 2007;2:108-113.
153. Porter AE, Gass M, Bendall JS, Muller K, Goode A, Skepper JN, Midgley PA, Welland M. Uptake of Noncytotoxic Acid-Treated Single-Walled Carbon Nanotubes into the Cytoplasm of Human Macrophage Cells. Acs Nano. 2009;3:1485-1492.
154. Hardman R. A toxicologic review of quantum dots: Toxicity depends on physicochemical and environmental factors. Environ Health Persp. 2006;114:165-172.
155. Urano M, Kuroda M, Nishimura Y. For the clinical application of thermochemotherapy given at mild temperatures. Int J Hyperther. 1999;15:79-107.
156. Murray TG, Cicciarelli N, McCabe CM, Ksander B, Feuer W, Schiffman J, Mieler WF, OBrien JM. In vitro efficacy of carboplatin and hyperthermia in a murine retinoblastoma cell line. Invest Ophth Vis Sci. 1997;38:2516-2522.
157. Di Filippo F, Carlini S, Garinei R, Perri P, Anza M, Ferranti F, Saracca E, Schiratti M, Cavaliere F, Cavaliere R. Local hyperthermia and systemic chemotherapy for treatment of recurrent melanoma. World journal of surgery. 1995;19:359-362.
158. al-Shabanah OA, Osman AM, al-Harbi MM, al-Gharably NM, al-Bekairi AM. Enhancement of doxorubicin-induced cytotoxicity by hyperthermia in Ehrlich ascites cells. Chemotherapy. 1994;40:188-194.
159. Landis SH, Murray T, Bolden S, Wingo PA. Cancer statistics, 1999. Ca-Cancer J Clin. 1999;49:8-31.
160. Raghavan D, Shipley WU, Garnick MB, Russell PJ, Richie JP. Biology and Management of Bladder-Cancer. New Engl J Med. 1990;322:1129-1138.
161. Amling CL. Diagnosis and management of superficial bladder cancer. Curr Prob Cancer. 2001;25:219-278.
162. Stein JP, Lieskovsky G, Cote R, Groshen S, Feng AC, Boyd S, Skinner E, Bochner B, Thangathurai D, Mikhail M, Raghavan D, Skinner DG. Radical cystectomy in the treatment of invasive bladder cancer: Long-term results in 1,054 patients. J Clin Oncol. 2001;19:666-675.

163. Rodel C, Grabenbauer GG, Kuhn R, Papadopoulos T, Dunst J, Meyer M, Schrott KM, Sauer R. Combined-modality treatment and selective organ preservation in invasive bladder cancer: Long-term results. J Clin Oncol. 2002;20:3061-3071.
164. Rietbroek RC, Schilthuis MS, Bakker PJM, vanDijk JDP, Postma AJ, Gonzalez DG, Bakker AJ, vanderVelden J, Helmerhorst TJM, Veenhof CHN. Phase II trial of weekly locoregional hyperthermia and cisplatin in patients with a previously irradiated recurrent carcinoma of the uterine cervix. Cancer. 1997;79:935-943.
165. Falk MH, Issels RD. Hyperthermia in oncology. Int J Hyperther. 2001;17:1-18.
166. Bader MJ, Sroka R, Gratzke C, Seitz M, Weidlich P, Staehler M, Becker A, Stief CG, Reich O. Laser Therapy for Upper Urinary Tract Transitional Cell Carcinoma: Indications and Management. Eur Urol. 2009;56:65-71.
167. Lokich J, Anderson N. Carboplatin versus cisplatin in solid tumors: An analysis of the literature. Ann Oncol. 1998;9:13-21.
168. Knox RJ, Friedlos F, Lydall DA, Roberts JJ. Mechanism of Cytotoxicity of Anticancer Platinum Drugs - Evidence That Cis-Diamminedichloroplatinum(Ii) and Cis-Diammine-(1,1-Cyclobutanedicarboxylato)Platinum(Ii) Differ Only in the Kinetics of Their Interaction with DNA. Cancer Res. 1986;46:1972-1979.
169. Buzdar AU, Marcus C, Smith TL, Blumenschein GR. Early and Delayed Clinical Cardiotoxicity of Doxorubicin. Cancer. 1985;55:2761-2765.
170. Childs AC, Phaneuf SL, Dirks AJ, Phillips T, Leeuwenburgh C. Doxorubicin treatment in vivo causes cytochrome c release and cardiomyocyte apoptosis, as well as increased mitochondrial efficiency, superoxide dismutase activity, and Bcl-2 : Bax ratio. Cancer Res. 2002;62:4592-4598.
171. Aubelsadron G, Londosgagliardi D. Daunorubicin and Doxorubicin, Anthracycline Antibiotics, a Physicochemical and Biological Review. Biochimie. 1984;66:333-352.
172. Adams M, Kerby IJ, Rocker I, Evans A, Johansen K, Franks CR. A Comparison of the Toxicity and Efficacy of Cisplatin and Carboplatin in Advanced Ovarian-Cancer. Acta Oncol. 1989;28:57-60.
173. Doz F, Berens ME, Dougherty DV, Rosenblum ML. Comparison of the Cytotoxic Activities of Cisplatin and Carboplatin against Glioma Cell-Lines at Pharmacologically Relevant Drug Exposures. J Neuro-Oncol. 1991;11:27-35.
174. Petrioli R, Frediani B, Manganelli A, Barbanti G, DeCapua B, DeLauretis A, Salvestrini F, Mondillo S, Francini G. Comparison between a cisplatin-containing regimen and a carboplatin-containing regimen for recurrent or metastatic bladder cancer patients - A randomized phase II study. Cancer. 1996;77:344-351.
175. Raaphorst GP, Doja S, Davis L, Stewart D, Ng CE. A comparison of hyperthermia cisplatin sensitization in human ovarian carcinoma and glioma cell lines sensitive and resistant to cisplatin treatment. Cancer Chemoth Pharm. 1996;37:574-580.
176. Meyn RE, Corry PM, Fletcher SE, Demetriades M. Thermal Enhancement of DNA Damage in Mammalian-Cells Treated with Cis-Diamminedichloroplatinum(Ii). Cancer Res. 1980;40:1136-1139.
177. Liu Y, Cho CW, Yan XD, Henthorn TK, Lillehei KO, Cobb WN, Ng KY. Ultrasound-induced hyperthermia increases cellular uptake and cytotoxicity of P-glycoprotein substrates in multi-drug resistant cells. Pharmaceut Res. 2001;18:1255-1261.

178. Medintz IL, Pons T, Delehanty JB, Susumu K, Brunel FM, Dawson PE, Mattoussi H. Intracellular delivery of quantum dot-protein cargos mediated by cell penetrating peptides. Bioconjugate Chem. 2008;19:1785-1795.
179. Clapp AR, Goldman ER, Mattoussi H. Capping of CdSe-ZnS quantum dots with DHLA and subsequent conjugation with proteins. Nature Protocols. 2006;1:1258-1266.
180. Susumu K, Uyeda HT, Medintz IL, Pons T, Delehanty JB, Mattoussi H. Enhancing the stability and biological functionalities of quantum dots via compact multifunctional ligands. J Am Chem Soc. 2007;129:13987-13996.
181. Liu YF, Xie B, Yin ZG, Fang SM, Zhao JB. Synthesis of Highly Stable CdTe/CdS Quantum Dots with Biocompatibility. Eur J Inorg Chem. 2010:1501-1506.
182. Liu WH, Greytak AB, Lee J, Wong CR, Park J, Marshall LF, Jiang W, Curtin PN, Ting AY, Nocera DG, Fukumura D, Jain RK, Bawendi MG. Compact Biocompatible Quantum Dots via RAFT-Mediated Synthesis of Imidazole-Based Random Copolymer Ligand. J Am Chem Soc. 2010;132:472-483.
183. Yadav RS, Mishra P, Mishra R, Kumar M, Pandey AC. Histidine functionalised biocompatible CdS quantum dots synthesised by sonochemical method. J Exp Nanosci. 2010;5:348-356.
184. Ajima K, Murakami T, Mizoguchi Y, Tsuchida K, Ichihashi T, Iijima S, Yudasaka M. Enhancement of In Vivo Anticancer Effects of Cisplatin by Incorporation Inside Single-Wall Carbon Nanohorns. Acs Nano. 2008;2:2057-2064.
185. Yuge R, Yudasaka M, Miyawaki J, Kubo Y, Isobe H, Yorimitsu H, Nakamura E, Iijima S. Plugging and unplugging holes of single-wall carbon nanohorns. J Phys Chem C. 2007;111:7348-7351.
186. Fan J, Yuge R, Miyawaki J, Kawai T, Iijimia S, Yudasaka M. Close-open-close evolution of holes at the tips of conical graphenes of single-wall carbon nanohorns. J Phys Chem C. 2008;112:8600-8603.
187. Peng ZA, Peng XG. Formation of high-quality CdTe, CdSe, and CdS nanocrystals using CdO as precursor. J Am Chem Soc. 2001;123:183-184.

# APPENDIX A: COPYRIGHT PERMISSIONS

## NATURE PUBLISHING GROUP LICENSE TERMS AND CONDITIONS

May 10, 2012

---

This is a License Agreement between Kristen Zimmermann ("You") and Nature Publishing Group ("Nature Publishing Group") provided by Copyright Clearance Center ("CCC"). The license consists of your order details, the terms and conditions provided by Nature Publishing Group, and the payment terms and conditions.

**All payments must be made in full to CCC. For payment instructions, please see information listed at the bottom of this form.**

| | |
|---|---|
| License Number | 2901541439129 |
| License date | May 03, 2012 |
| Licensed content publisher | Nature Publishing Group |
| Licensed content publication | Nature Reviews Drug Discovery |
| Licensed content title | Nanoparticle therapeutics: an emerging treatment modality for cancer |
| Licensed content author | Mark E. Davis, Zhuo (Georgia) Chen, Dong M. Shin |
| Licensed content date | Sep 1, 2008 |
| Type of Use | reuse in a thesis/dissertation |
| Requestor type | academic/educational |
| Format | print and electronic |
| Portion | figures/tables/illustrations |
| Number of figures/tables/illustrations | 1 |
| High-res required | no |
| Figures | Table 1. Nanoscaled Systems for systemic cancer therapy |
| Author of this NPG article | no |
| Your reference number | |
| Title of your thesis / dissertation | Intracellular Transport in Cancer Treatments: Carbon Nanohorns Conjugated to Quantum Dots and Chemotherapeutic Agents |
| Expected completion date | May 2012 |
| Estimated size (number of pages) | 100 |
| Total | 0.00 USD |
| Terms and Conditions | |

## ELSEVIER LICENSE

## TERMS AND CONDITIONS

May 10, 2012

This is a License Agreement between Kristen Zimmermann ("You") and Elsevier ("Elsevier") provided by Copyright Clearance Center ("CCC"). The license consists of your order details, the terms and conditions provided by Elsevier, and the payment terms and conditions.

**All payments must be made in full to CCC. For payment instructions, please see information listed at the bottom of this form.**

| | |
|---|---|
| Supplier | Elsevier Limited<br>The Boulevard,Langford Lane<br>Kidlington,Oxford,OX5 1GB,UK |
| Registered Company Number | 1982084 |
| Customer name | Kristen Zimmermann |
| Customer address | 340 ICTAS Bldg. (MC 0298)<br>Blacksburg, VA 24060 |
| License number | 2901550662591 |
| License date | May 03, 2012 |
| Licensed content publisher | Elsevier |
| Licensed content publication | Advanced Drug Delivery Reviews |
| Licensed content title | Delivery of nanomedicines to extracellular and intracellular compartments of a solid tumor |
| Licensed content author | Yinghuan Li,Jie Wang,M. Guillaume Wientjes,Jessie L.-S. Au |
| Licensed content date | January 2012 |
| Licensed content volume number | 64 |
| Licensed content issue number | 1 |
| Number of pages | 11 |
| Start Page | 29 |
| End Page | 39 |
| Type of Use | reuse in a thesis/dissertation |
| Intended publisher of new work | other |
| Portion | figures/tables/illustrations |
| Number of figures/tables/illustrations | 1 |

| | |
|---|---|
| Format | both print and electronic |
| Are you the author of this Elsevier article? | No |
| Will you be translating? | No |
| Order reference number | |
| Title of your thesis/dissertation | Intracellular Transport in Cancer Treatments: Carbon Nanohorns Conjugated to Quantum Dots and Chemotherapeutic Agents |
| Expected completion date | May 2012 |
| Estimated size (number of pages) | 100 |
| Elsevier VAT number | GB 494 6272 12 |
| Permissions price | 0.00 USD |
| VAT/Local Sales Tax | 0.0 USD / 0.0 GBP |
| Total | 0.00 USD |
| Terms and Conditions | |